UNIVERSITY OF CALIFORNIA SAN DIEGO

Photodetection in Disordered Materials

A dissertation submitted in partial satisfaction of the
requirements for the degree
Doctor of Philosophy

in

NanoEngineering

by

Zihan Xu

Committee in charge:

Professor Yu-Hwa Lo, Chair
Professor Kenji Nomura, Co-Chair
Professor Shyue Ping Ong, Co-Chair
Professor Renkun Chen
Professor Ping Liu
Professor Kesong Yang

2020

The Dissertation of Zihan Xu is approved, and it is acceptable in quality and form for publication on microfilm and electronically:

_____

_____

_____

_____

Co-Chair

_____

Co-Chair

_____

Chair

University of California San Diego

2020

DEDICATION

To Yongren Yu, Juan Yu and Qinghe Xu

TABLE OF CONTENTS

LIST OF FIGURES

ACKNOWLEGEMENTS

I would like to express my great gratitude to my advisor, Professor Yu-Hwa Lo, for teaching, inspiring and encouraging me so much. It has been my fortunate and honor to work under his guidance. I learnt from him not only the scientific mindset and the engineering spirits, but also how to be a caring and responsible individual. I thank my first co-advisor Professor Shyue Ping Ong for helping me get used to UCSD initially, guiding me with code development, and showing the importance of being professional in every way. I thank my other co-advisor Professor Kenji Nomura. He taught me to pay attentions to details while having a whole picture of my research. It was always helpful and cheerful from our weekly meetings. I thank other members on my Dissertation Committee, Professor Kesong Yang, Professor Ping Liu and Professor Renkun Chen for their supports and valuable suggestions in the completion of this dissertation.

I thank all members from Professor Lo's Group for the enriching and supportive three plus years together. I thank Yugang Yu, Jiayun Zhou, Alex Ce Zhang, M.A. Raihain Miah, Shaurya Arya, Zijian Zeng, Samir Damle, Shelly Chiu and Li-Yuan Chiang from the Photonics subgroup and Ram Subramanian, Yi-Huan Tsai, Rui Tang, Edward Wang, Xinyu Chen, Zhilin Guo, Chi-Yang Tseng, Lauren Waller, Zunming Zhang from the Biomedial subgroup. I also thank former members from Professor Lo's Group, Dr. Yu-Hsin Liu, Dr. Lujiang Yan, Dr. David Hall, Dr. Iftikhar A. Niaz, Dr. Roger Chiu, Dr. Wen Qiao, Dr. Brian Lewis, Dr. Tiantian Zhang, Dr. Wei Cai, Dr. Tony Yen, Dr. Yi Gu, Dr. Pingwei Chen, Dr. Yuanyuan Han, Dr. Jiajie Chen and Dr. Zhe Mei. I especially thank Yu-

Hsin, Lujiang and David for mentoring me when I was new to Lo's lab. I want to thank Yugang a lot for working closely with me for our two co-first author publications. I thank Dr. Balachandran Radhakrishnan and Dr. Iek-Heng Chu for mentoring me in MAVRL.

I thank all my collaborators of publications outside Lo's lab, Professor Zhaowei Liu, Dr. Shilong Li, Professor Sheng Xu, Yusheng Lei, Yusheng Lei, Richard Tran, Dr. Donald Winston, Dr. Wenhao Sun, Dr. Kristin A Persson, Dr. Naixie Zhou, Professor Jian Luo, Dr. Han Nguyen, Dr. Sunny Hy, Dr. Yuh-Chieh Lin, Dr. Zhenbin Wang, Dr. Zhi Deng and Professor Ying Shirley Meng. I thank the staff of the UCSD Nano3/SDNI facility, Dr. Bernd Fruhberger, Ryan Anderson, Dr. Xuekun Lu, Larry Grissom, Dr. Namseok Park, Sean Parks and Shu Xiang, for their technical support. I thank Dr. Nicolas Vargas Ayalai for helping with MBE CuPc film deposition. I also thank Dr. Zhenghui Wu, Dr. Weichuan Yao, Kaiping Wang and Yichen Zhai from Professor Ting Ng's Group for their assistance in glove box usage.

I thank my personal trainer Bobby Martinez for encouraging me to complete my first NYC marathon before my senate exam. From the training for marathons, I learnt to take my pace and complete with myself, while pushing myself hard and enjoying the weekly improvement. Regular exercises are important to prepare myself with a strong heart through the long journey of the PhD study. I thank Zihua Liu, an old friend of mine, for encouraging me to seize all kinds of opportunities to improve myself.

I thank those professors at UCSD because I learnt a lot and really enjoyed their classes and discussing with them, Professor Jorge E. Hirsch, Professor Daniel Arovas, Professor Vlado Lubarda, Professor Gert Lanckriet, Professor Yoav Freund, Professor

Dimitris N. Politis, Professor Shadi Dayeh, Professor Douglas Pinto, Professor Judith Sharp, Professor David Barner, Professor Nicholas Christenfeld, Professor Delbert Foit and Professor Vish Krishnan. I thank the staffs of NanoEngineering, especially for my graduate coordinator, Dana Jimenez, for being helpful and easy to work with.

I thank my undergrad research advisor, Professor Wen-Yan Yin from Zhejiang University, for leading me to scientific research. I thank my undergrad professor, Dr. Jianqi Shen, for guiding me though publishing my first paper. I thank my high school physics teacher, Suping Wang, for inspiring me of the importance of hand-on experiments. I thank my high school math teacher, Ming Liu, for emphasizing the beauty of math. I thank my high school chemistry teacher, Wei Zhou, for encouraging me on finding and asking questions to gain deeper comprehension. I thank my Uncle, Yongren Yu, for believing in my dream of pursuing the Ph.D. degree since I was still in primary school.

I thank many coincidences in life, especially for Google Mail service for misclassifying the offer letter from another university as junk emails to help me decide to pursue my PhD study at UCSD. I thank my friends at UCSD for making my graduate study colorful. I thank my friends from our 1106G group in my undergrad for fighting against GRE together, especially for Motao Cao, Yichen Shen, Yue Zhang and Ting Yang. I thank my close friends Wanxi Liu, Xun Liu, Bo Zhang, Lihao Xu, Yue Wu and Qian Huang, for being with me and sharing important moments as well as trivial warmth and worries, even when we were not in the same city.

Finally, I thank my mom, Juan Yu, my dad, Qinghe Xu and my husband, Ilya Valmianski, for the enormous amount of support, encouragement and love.

Portions of Chapter 3 have been published in the following publication: Yugang Yu†, **Zihan Xu**†, Shilong Li, Alex Ce Zhang, Lujiang Yan, Zhaowei Liu, and Yu-Hwa Lo. "Plasmonically Enhanced Amorphous Silicon Photodetector with Internal Gain." *IEEE Photonics Technology Letters* 31, no. 12 (2019): 959-962. († These authors contributed equally.) The dissertation author was the co-first author/primary investigator and author of these papers.

Portions of Chapter 4 have been published in the following publication: **Zihan Xu**†, Yugang Yu†, Shaurya Arya, Iftikhar Ahmad Niaz, Yimu Chen, Yusheng Lei, Mohammad Abu Raihan Miah, Jiayun Zhou, Alex Ce Zhang, Lujiang Yan, Sheng Xu, Kenji Nomura and Yu-Hwa Lo, "Frequency and Power Dependent Photoresponse of Perovskite Photodetector Down to Single Photon Level" *Nano Letters* (2020). († These authors contributed equally.) The dissertation author was the co-first author/primary investigator and author of these papers.

Portions of Chapter 5 have been published in the following publication: **Zihan Xu**†, Yugang Yu†, Shaurya Arya, Iftikhar Ahmad Niaz, Yimu Chen, Yusheng Lei, Mohammad Abu Raihan Miah, Jiayun Zhou, Alex Ce Zhang, Lujiang Yan, Sheng Xu, Kenji Nomura and Yu-Hwa Lo, "Frequency and Power Dependent Photoresponse of Perovskite Photodetector Down to Single Photon Level" *Nano Letters* (2020). († These authors contributed equally.) The dissertation author was the co-first author/primary investigator and author of these papers.

VITA

2013	Bachelor of Engineering, Zhejiang University Information Engineering of Optical Engineering Department
2015	Master of Science, University of California San Diego NanoEngineering
2020	Doctor of Philosophy, University of California San Diego NanoEngineering

PUBLICATIONS

Peer-Reviewed Journals

1. **Zihan Xu**†, Yugang Yu†, Shaurya Arya, Iftikhar Ahmad Niaz, Yimu Chen, Yusheng Lei, Mohammad Abu Raihan Miah, Jiayun Zhou, Alex Ce Zhang, Lujiang Yan, Sheng Xu, Kenji Nomura and Yu-Hwa Lo, "Frequency and Power Dependent Photoresponse of Perovskite Photodetector Down to Single Photon Level" *Nano Letters* (2020). († These authors contributed equally.)

2. Yugang Yu†, **Zihan Xu**†, Shilong Li, Alex Ce Zhang, Lujiang Yan, Zhaowei Liu, and Yu-Hwa Lo. "Plasmonically Enhanced Amorphous Silicon Photodetector with Internal Gain." *IEEE Photonics Technology Letters* 31, no. 12 (2019): 959-962. († These authors contributed equally.)

3. Lujiang Yan, Yugang Yu, **Zihan Xu**, Iftikhar Niaz, Mohammad Abu Raihan Miah, Alex Ce Zhang, Jiayun Zhou, and Yuhwa Lo. "Low Noise, High Gain-Bandwidth Photodetectors Using Cycling Exciting Process (CEP) as Amplification Mechanism." In *2018 IEEE International Conference on Electron Devices and Solid State Circuits (EDSSC)*, pp. 1-2. IEEE, 2018.

4. Richard Tran, **Zihan Xu**, Naixie Zhou, Balachandran Radhakrishnan, Jian Luo, and Shyue Ping Ong. "Computational study of metallic dopant segregation and embrittlement at molybdenum grain boundaries." *Acta Materialia* 117 (2016): 91-99.

5. Richard Tran, **Zihan Xu**, Balachandran Radhakrishnan, Donald Winston, Wenhao Sun, Kristin A. Persson, and Shyue Ping Ong. "Surface energies of elemental crystals." *Scientific data* 3 (2016): 160080.

6. Iek-Heng Chu, Han Nguyen, Sunny Hy, Yuh-Chieh Lin, Zhenbin Wang, **Zihan Xu**, Zhi Deng, Ying Shirley Meng, and Shyue Ping Ong. "Insights into the performance limits of the Li7P3S11 superionic conductor: a combined first-principles and experimental study." *ACS applied materials & interfaces* 8, no. 12 (2016): 7843-7853.

Patents

1. Yu-Hwa Lo, David Hall, Yu-Hsin Liu, **Zihan Xu**, and Lujiang Yan. "Systems, devices and methods for amplification of signals based on a cycling excitation process in disordered materials." U.S. Patent Application 16/486,482, filed November 28, 2019.

ABSTRRACT OF THE DISSERTATION

Photodetection in Disordered Materials

by

Zihan Xu

Doctor of Philosophy in NanoEngineering

University of California San Diego, 2020

Professor Yu-Hwa Lo, Chair

Professor Kenji Nomura, Co-Chair

Professor Shyue Ping Ong, Co-Chair

This dissertation offers two different mechanisms for photodetection in disordered materials. Photodetectors made of amorphous materials enable low cost optical imaging and communications over non-semiconductor platforms. The key challenges are to

improve efficiency, sensitivity, and frequency response. Using the localized surface plasmon resonance (LSPR) effect and an efficient carrier multiplication process, cycling excitation process (CEP), the plasmonically enhanced amorphous silicon photodetector (PEASP) with a thin (60 nm) absorption layer achieves a high external quantum efficiency with a record fast impulse response of 170 ps (FWHM). This approach offers the possibility of making detectors out of amorphous material for high frame rate imaging and optical communications in spite of the material's low carrier mobility.

Spin-coating thin film is another approach in obtaining disordered materials. Organometallic halide perovskites attract strong interests for their high photoresponsivity and solar cell efficiency. However, there was no systematic study of their power and frequency dependent photoresponsivity. Two different power-dependent photoresponse types in methylammonium lead iodide perovskite ($MAPbI_3$) photodetectors were identified. In the first type, photoresponse remains constant from 5 Hz to 800 MHz. In the second type, absorption of a single photon can generate a persistent photoconductivity of 30 pA under an applied electric field of 2.5×10^4 V/cm. Additional absorbed photons, up to 8, linearly increase the persistent photoconductivity, which saturates with absorption of more than 10 photons. This is different than single photon avalanche detectors (SPADs) because the single photon response is persistent as long as the device is under bias, providing unique opportunities for novel electronic and photonic devices such as analog memories for neuromorphic computing. An avalanche-like process for iodine ions was proposed, with the estimation that absorption of a single 0.38 aJ photon triggers motion of $10^{8\text{-}9}$ ions, resulting in accumulations of ions and charged vacancies at the

$MAPbI_3$/electrode interfaces to cause band bending and change of material electric properties. This is the first observation that single-digit photon absorption can alter the macroscopic electric and optoelectronic properties of a perovskite thin film. DFT toy model calculations were also conducted to further support the proposed ionic impact ionization.

Chapter 1 Introduction

1.1 Introduction for Photodetection

Light is a natural medium for information, from the burning logs to the starry sky. In ancient China, when the enemies came, warriors from the watchtower could send warning signals by starting some smoky fires and the signal can be transferred along the Great Wall [1] to major cities. That was the fastest signaling method thanks to the speed of light. Nowadays, we can transport more complicated information thanks to the optical telecommunication development, also using light as the medium. In particular, photodetction is a critical part in the entire process of optical telecommunication [2], which requires high sensitivity, low noise and high speed.

Photodetection has wide applications through the spectrum of light, including detecting air pollution with UV light, camera color imaging with visible light, bioimaging with NIR light, optical telecommunication with SWIR light, chemical analysis from MWIR, thermal imaging from LWIR and medical imaging from FIR and THz light [3]. Taking the visible photodetection as an example, the current state of art cameras still cannot capture the images as accurately as human eyes in many cases [4]. There is still a long way to improve the photodetector performance with advantageous features such as low operation voltage, internal amplification mechanism to handle low light intensity situation, low noise to achieve better signal to noise ratio.

1.2 Operating Principles for Photodetectors with Weak Light

Signal amplification and noise management are critical to achieve weak light detection, especially when pushing the limit down to single photon level. In terms of signal amplification for photodetector, the dominant intrinsic mechanism is impact ionization for over 40 years. Conventionally, the two major approaches for photodetectors of weak light application are avalanche photodiode (APD) [5] and the single photon avalanche detector (SPAD) [6].

APD photodetectors have reasonable dynamic range for around 30 dB as well as can achieve modest gain with intermediate voltage, which are their advantages. But APD photodetectors have limited sensitivity due to the excess noise, as a remarkable drawback. In terms of SPAD photodetectors, it can have down to single photon sensitivity with a very high price. SPAD photodetectors have to operate at high bias voltage above breakdown and it cannot be used for input photon number counting for lack of input photon number resolution.

In 2014, cycling excitation process (CEP) mechanism was discovered in heavily co-doped Si photodetector [7]. With the assistance of localized states and phonon interaction, this internal amplification process can operate under a much lower bias with high gain, low noise.

1.3 Motivation

Localized states are common in disordered materials [8], showing the possibility of applying CEP mechanism to improve photodetection under weak light or high speed. We've been looking for new materials with CEP mechanism for photodetector

applications as well as trying to enhance the CEP mechanism in disorder materials. It's also important to manage the disorder level in materials for CEP mechanism and explore different substrates for broader application in the future.

We're also interested in investigating the other internal amplification process in disorder materials. Organometallic perovskites have drawn a lot of attentions for its high detectivity and the unconventional high photoresponse suggest some novel device physics for perovskite devices. [9]

1.4 Synopsis of Dissertation

CEP mechanism in disordered materials is a recent new discovery for operating principles of signal amplification in the device. With very different disorder level between amorphous Si and spin-coated perovskite photodetector, the high photoresponses have different origin and physics. In order to further improve photodetector performance and reduce fabrication cost, we incorporated the CEP mechanism in amorphous Si with other signal amplification methods as well as looked into spin-coated organic film including perovskite to investigate alternative signal amplification process other than the conventional impact ionization. This dissertation is organized as below.

In Chapter 2, a recently found internal amplification process in disordered material, CEP mechanism, is discussed. An organic CEP photodetector with CuPc film is demonstrated.

In Chapter 3, an amorphous Si photodetector with gold nanoparticle is discussed. With the help of localized surface plasmon resonance (LSPR) effect, both the

responsivity and the device speed are improved. 3D electromagnetic simulation is conducted to verify the enhancement from gold nanoparticle.

In Chapter 4, a spin-coated organometallic perovskite photodetector is demonstrated. Two different types of photodetection are discussed. One type of photodetection is the convectional photoresponse, with high speed for perovskite photodetectors. The other type of photoresponse is quasi-persistent photoresponse, which can reach single photon sensitivity and is reversible, suggesting a novel internal amplification mechanism in perovskite.

In Chapter 5, in order to explain the quasi-persistent photoresponse with single photon sensitivity in Chapter 4, the ionic impact ionization mechanism is proposed. A toy model using density functional theory (DFT) is calculated to further support the proposed mechanism.

In Chapter 6, a conclusion of photodetection in disordered materials is shown. Future work and applications of ionic impact ionization in perovskite and cycling excitation process are also presented.

References:

[1] Waldron, Arthur (1990). The Great Wall of China : from history to myth. Cambridge England New York: Cambridge University Press. ISBN 978-0-521-42707-4.

[2] Miller, Stewart E. "Lightwaves and Telecommunication", American Scientist, Sigma Xi, The Scientific Research Society, January–February 1984, Vol. 72, No. 1, pp. 66-71

[3] Zhuge, Fuwei, Zhi Zheng, Peng Luo, Liang Lv, Yu Huang, Huiqiao Li, and Tianyou Zhai. "Nanostructured materials and architectures for advanced infrared photodetection." Advanced Materials Technologies 2, no. 8 (2017): 1700005.

[4] Skorka, O. and Joseph, D., 2011. Toward a digital camera to rival the human eye. Journal of Electronic Imaging, 20(3), p.033009.

[5] Campbell, Joe C., Stephane Demiguel, Feng Ma, Ariane Beck, Xiangyi Guo, Shuling Wang, Xiaoguang Zheng, Li, X., Beck, J.D., Kinch, M.A. and Huntington, A. "Recent advances in avalanche photodiodes." IEEE Journal of selected topics in quantum electronics 10, no. 4 (2004): 777-787.

[6] Itzler, Mark A., R. Ben-Michael, C-F. Hsu, Krystyna Slomkowski, Alberto Tosi, Sergio Cova, Franco Zappa, and Radu Ispasoiu. "Single photon avalanche diodes (SPADs) for 1.5 μ m photon counting applications." Journal of Modern Optics 54, no. 2-3 (2007): 283-304.

[7] Liu, Yu-Hsin, Lujiang Yan, Alex Ce Zhang, David Hall, Iftikhar Ahmad Niaz, Yuchun Zhou, L. J. Sham, and Yu-Hwa Lo. "Cycling excitation process: An ultra efficient and quiet signal amplification mechanism in semiconductor." Applied Physics Letters 107, no. 5 (2015): 053505.

[8] Bullot, J., and M. P. Schmidt. "Physics of amorphous silicon–carbon alloys." physica status solidi (b) 143, no. 2 (1987): 345-418.

[9] Zhao, Yixin, and Kai Zhu. "Organic–inorganic hybrid lead halide perovskites for optoelectronic and electronic applications." Chemical Society Reviews 45, no. 3 (2016): 655-689.

Chapter 2 Disordered Materials and Gain Mechanism

2.1 CEP Mechanism

Carrier excitation process in disordered materials is the alternative carrier multiplication mechanism compared with the conventional impact ionization. In disordered materials, both extended and localized states are involved in the carrier multiplication process. In discovery of CEP mechanism [1], this internal amplification process was demonstrated in compensated doped silicon. A brief illustration of CEP mechanism is shown in Figure 2.1.

The primary photocurrent is generated from the absorption of a photon (Figure 2.1.a) and the electron/hole pair is separated by the applied electric field. The operation voltage for CEP process is relatively low, thanks to relaxing k-selection rule [2]. Silicon as an indirect bandgap photodetector, in order to satisfy the momentum conservation, it requires a specific k-vector, which is difficult in the extended states. However, it's much easier to achieve in the localized states in the disordered materials. Figure 2.1.b shows relaxing k-selection rule and the Auger excitation [3] by energetic electrons, moving a localized-state electron (charge carrier) to the mobile band, leaving an unoccupied impurity state. The other import process in CEP is phonon absorption, through a phonon interaction with a localized electron, as shown in Figure 2.1.c. By absorbing a phonon [4], the previously neutralized impurity is re-ionized, creating a mobile hole in Figure 2.1.c. Then the mobile hole gains enough energy from the electric field and trigger another auger excitation and relax of k-selection rule, as shown in Figure 2.1.d. With

another phonon absorption in Figure 2.1.e, a new mobile electron is created, and the second cycle can start as illustrated in Figure 2.1.f.

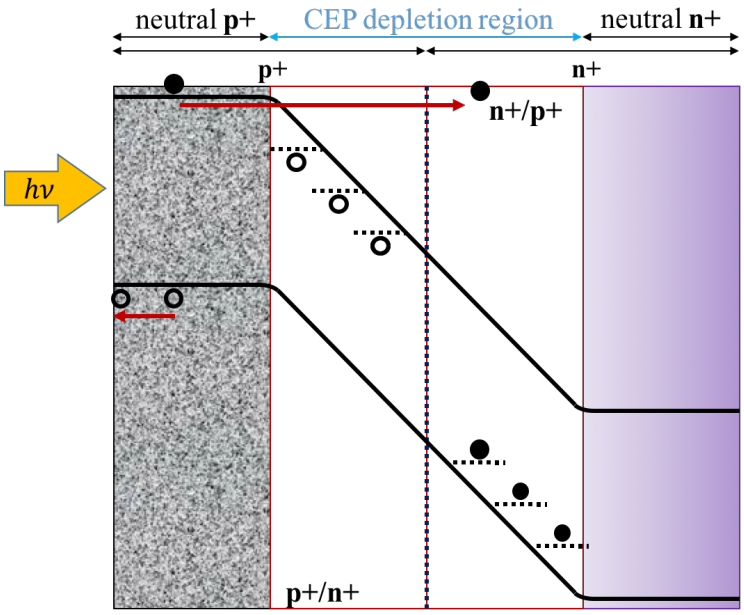

a. The first cycle of CEP starts with photon generated electron hole pair.

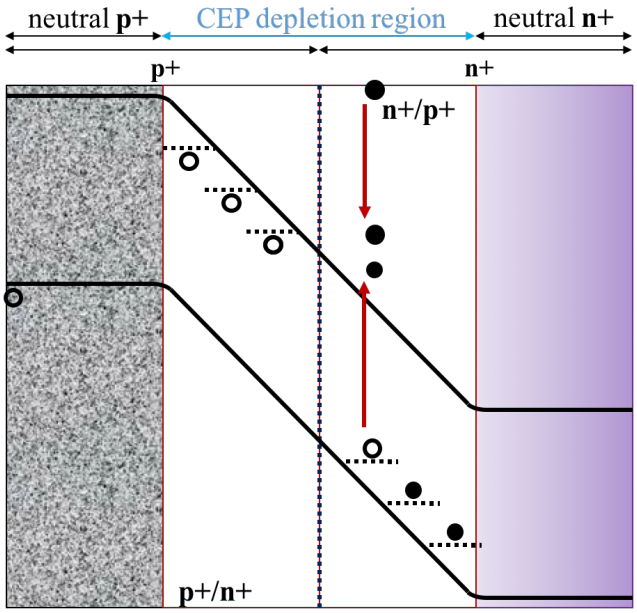

b. Auger excitation by energetic electrons and relaxing K-selection rule.

Figure 2.1. Illustration of CEP Mechanism.

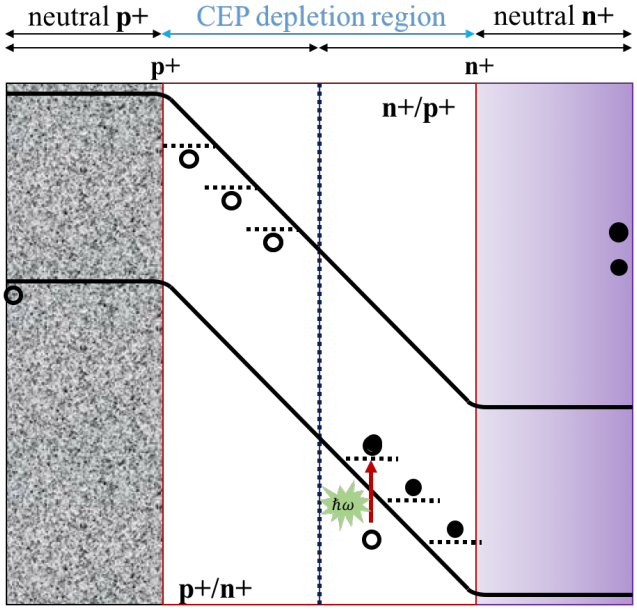

c. Phonon absorption generates a hot hole.

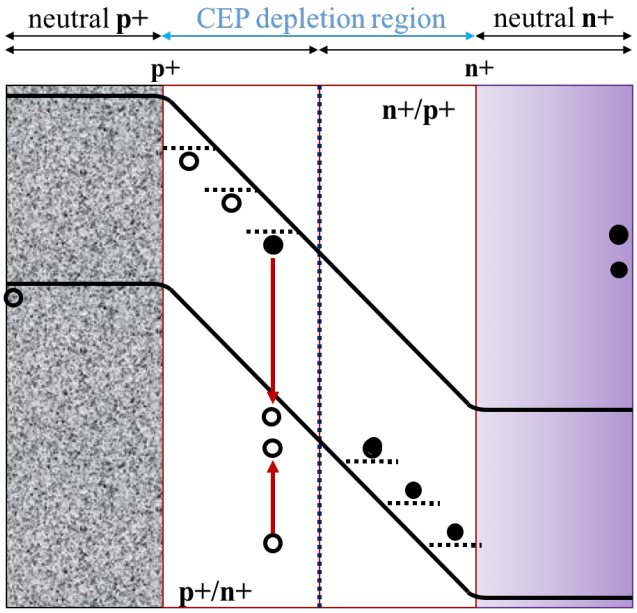

d. Auger excitation by energetic hole and relaxing K-selection rule.

Figure 2.1. Illustration of CEP mechanism, continued.

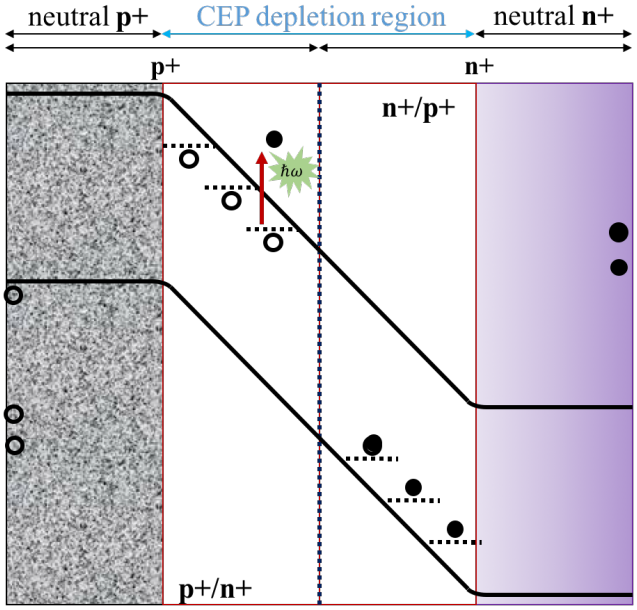

e. Phonon absorption generates a hot electron.

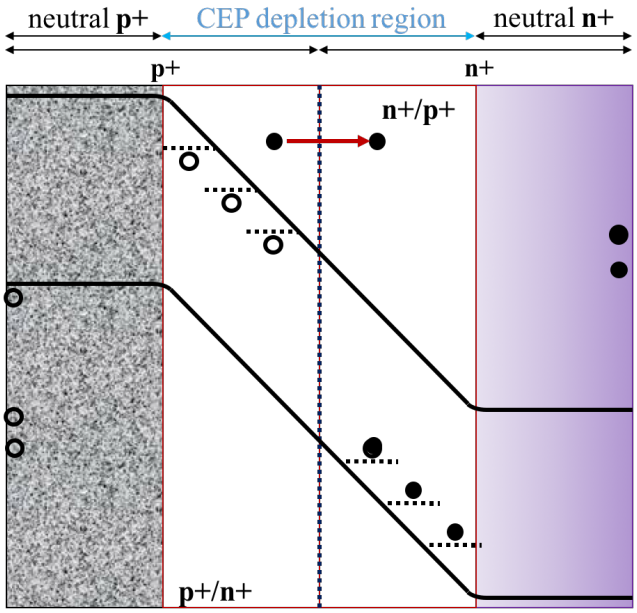

f. The start of the second cycle.

Figure 2.1. Illustration of CEP Mechanism, continued.

2.2 Photodection in two types of disordered CuPc films

In the search of disordered materials for CEP mechanism, we are not only interested in amorphous semiconductor materials such as amorphous Si, but also interested in organic thin film. Copper (II) phthalocyanine (CuPc) attracted my attention because of its band alignment with GaAs as substrate and ITO as the top electrode, as shown in Figure 2.2. We'll discuss the fabrication and characterization of CuPc device as an example for CEP photodetector based on disordered organic materials.

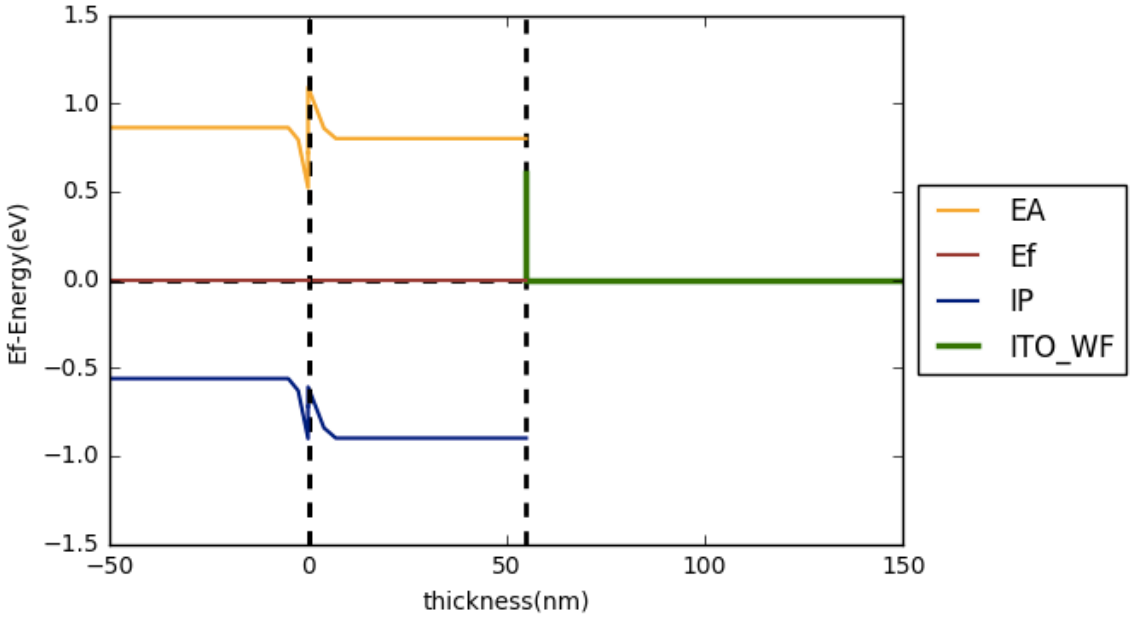

Figure 2.2. Band diagram at 0V of CuPc on GaAs devices

2.2.1 Fabrication of spin-coated CuPc photodetector

The fabrication process is illustrated in Figure 2.3. We started with substrate wafer clean and passivation (Figure 2.3.a). The diced p-GaAs substrate was solvent

cleaned with sonication, in the order of acetone (2 minutes), methanol (2 minutes), IPA (2 minutes), and then rinsed with deionized (DI) water. In order to remove native oxide, the substrate was soak in HCl for 1 minute and then rinsed with DI water.

The CuPc power was dissolved in chlorobenzene (CB): trifluoroacetic acid (TFA) = 4:1 in volume, with concentration of 0.8 mg/mL. The solution was stirred with a magnetic stirring bar and heat on a hot plate of 65 ºC overnight. The CuPc film was deposited through spin-coating at 200 acc and 600 rpm for 90 seconds (Figure 2.3.b). Then CuPc device was baked in an oven at 80 ºC for 4 hours and cooled down from 80 ºC to 60 ºC, so as to remove solvents. The thickness of CuPc layer was around 45 nm.

Then a layer of 110 nm ITO was sputtered on the device (Figure 2.3.c). Then the positive photoresist AZ1518 was spin-coated and patterned as the mask (Figure 2.3.d) for the following etching. The ITO layer was wet etched in 50% HCl for 2 minutes (Figure 2.3.e). CuPc layer was patterned through dry etch with O2 plasma (Figure 2.3.f). Then the photoresist was removed by being exposed with flood mode and then immersed in the developer.

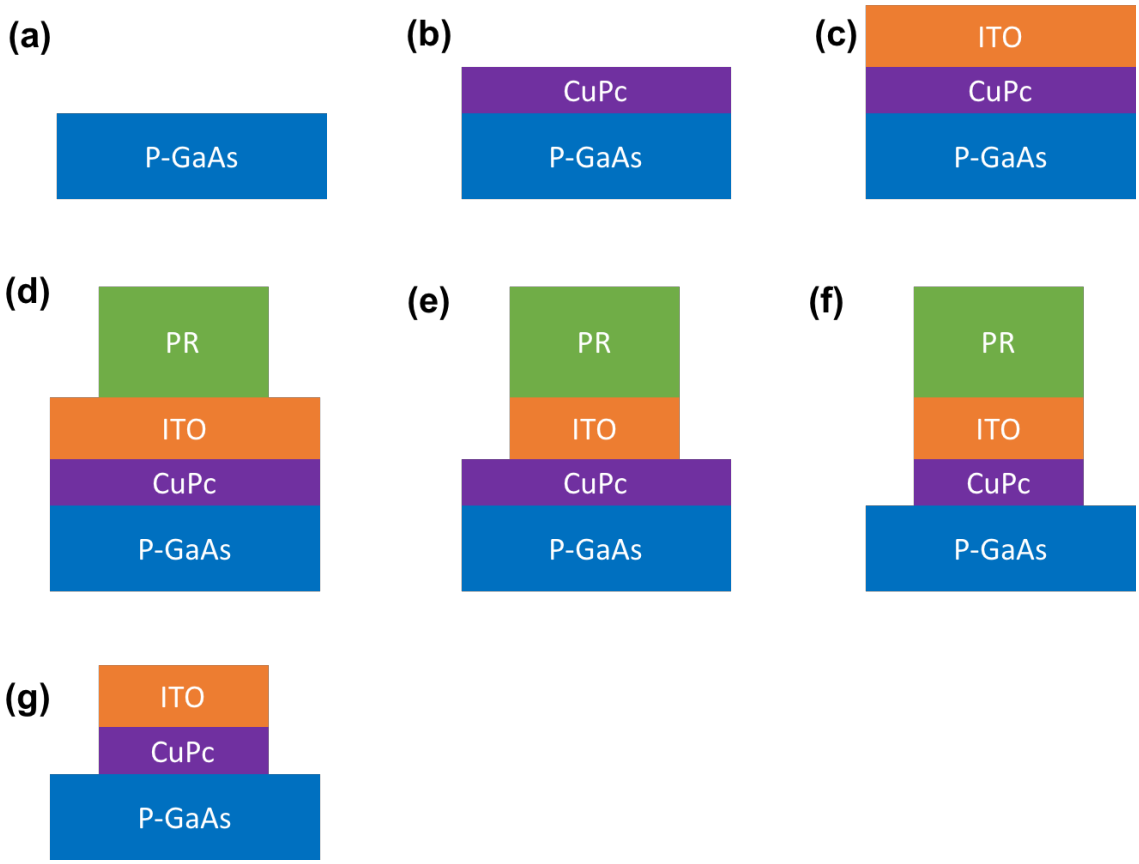

Figure 2.3. Process Flow for CuPc Device Fabrication. (a) Substrate preparation; (b) CuPc deposition and annealing; (c) ITO sputtering; (d) Photolithography with positive photoresist; (e) Wet etch of ITO layer with HCl solution; (f) Dry etch of CuPc layer with O2 plasma; (g) Removal of photoresist.

2.2.2 Device characterization of CuPc devices

Apart from the spin-coated CuPc photodetector, we also had MBE grown CuPc photodetector for comparison, and the only difference in their fabrication process is the CuPc deposition step in Figure 2.3.b. The X-ray measurement of MBE grown CuPc was done using rotating anode Cu K-alpha source filtered with a 4 bounce Ge 022 monochrometer (wavelength = 0.15418 nm). The X-ray characterization result is shown

in Figure 2.4. There is a peak at 6.8 degree but not at other 2-theta, which suggest that CuPc is entirely in the chevron orientation, standing on its edge relative to the substrate [5]. The broad background rise peaking at 16 degrees, which may be signature of an amorphous layer. From the quick rocking and chi scans, we can conclude the film is disordered. Because there is no size effect peaks or oscillations in XRR, the film should be rough enough.

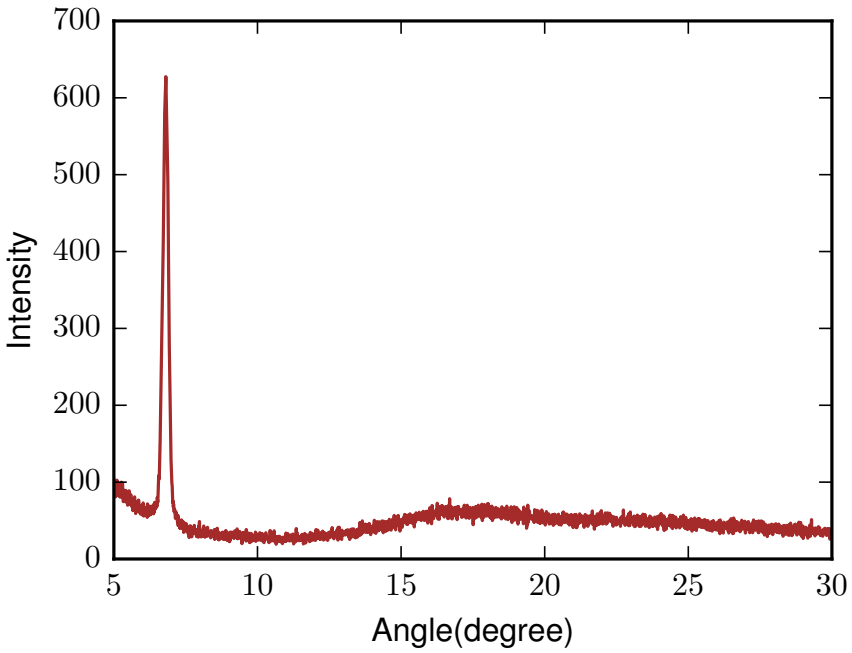

Figure 2.4 X-Ray Diffraction data for CuPc film (MBE)

We did bias dependent photoresponse characterization for both MBE grown CuPc photodetector and spin-coated CuPc photodetector and the results are shown in Figure 2.5. Though spin-coated CuPc and MBE grown CuPc should have different levels of disordered, but they have very similar photoresponse characterization and high gain compared with low bias, suggesting CEP mechanism in both case. Spin-coating organic

film can be a more convenient and cheaper way of depositing disordered materials for CEP photodetectors, which can be used for imaging and bio-sensing applications.

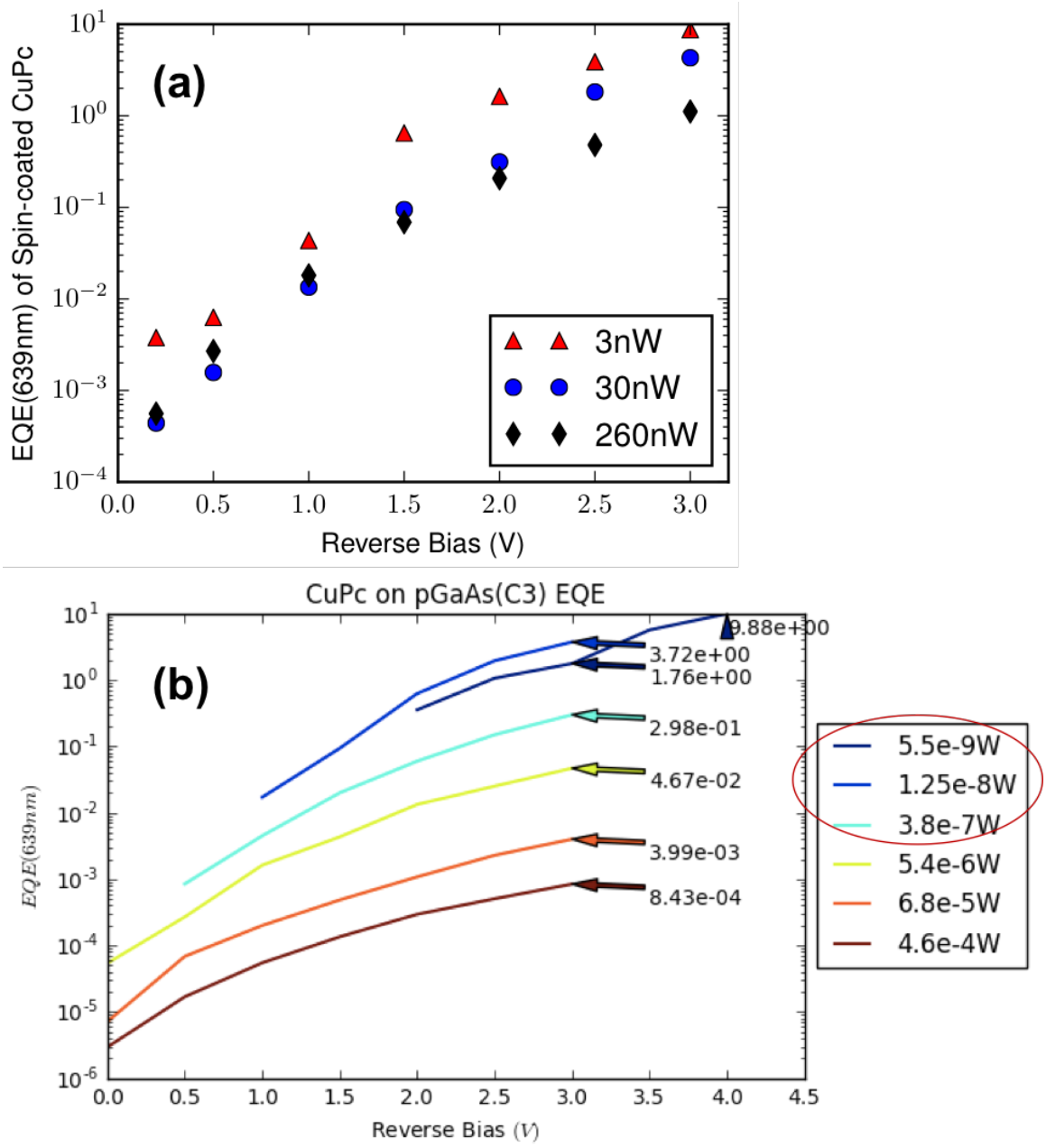

Figure 2.5 Bias dependent photoresponse for two types of CuPc. (a) Spin-coated CuPc photodetector. (b) MEB growth CuPc photodetector

References:

[1] Liu, Yu-Hsin, Lujiang Yan, Alex Ce Zhang, David Hall, Iftikhar Ahmad Niaz, Yuchun Zhou, L. J. Sham, and Yu-Hwa Lo. "Cycling excitation process: An ultra efficient and quiet signal amplification mechanism in semiconductor." *Applied Physics Letters* 107, no. 5 (2015): 053505.

[2] Sano, Nobuyuki, and Akira Yoshii. "Impact-ionization theory consistent with a realistic band structure of silicon." *Physical Review B* 45, no. 8 (1992): 4171.

[3] Dziewior, J., and W. Schmid. "Auger coefficients for highly doped and highly excited silicon." *Applied Physics Letters* 31, no. 5 (1977): 346-348.

[4] Wolff, P. A. "Theory of electron multiplication in silicon and germanium." *Physical Review* 95, no. 6 (1954): 1415.

[5] Ofuji, Masato, Katsuhiko Inaba, Kazuhiko Omote, Hajime Hoshi, Yoichi Takanishi, Ken Ishikawa, and Hideo Takezoe. "Grazing incidence in-plane X-ray diffraction study on oriented copper phthalocyanine thin films." *Japanese journal of applied physics* 41, no. 8R (2002): 5467.

Chapter 3 Plasmonically Enhanced Amorphous Si Photodetector

3.1 Previous Drawbacks for Semiconductor Photodetectors and Our Approaches

Photodetectors that convert optical signals into electrical currents are essential devices for imaging, sensing, and optical communications [1-2]. So far, inorganic crystalline semiconductors are the predominant material for photodetectors. Based on the operation wavelength, detectors are made of various types of crystalline semiconductors such as Si-, GaN-, and InGaAs-based materials. However, each material system requires a compatible crystalline semiconductor substrate that is nearly lattice-matched to the active layers of the detectors. The required high quality semiconductor substrates and epitaxial growth of active layers of detectors make photodetectors expensive to fabricate, costly to scale, and difficult to adapt to new platforms such as glass, ceramic or polymer substrates that become increasingly important for the emerging fields of internet of things (IOT), wearable electronics, flexible imaging and display, high frame rate cameras, underwater and free-space optical communications, etc. Therefore, there is a motivation to fabricate photodetectors on non-semiconductor substrate. Organic photodetectors, synthesized via low-cost solution-based methods on a non-semiconductor substrate, have been widely studied in this field [3-4].

In spite of promising results with organic semiconductor detectors, most organic semiconductor materials still suffer from poor stability, especially in environments with high temperature, moisture, light and oxygen [5-6]. To assure their reliability and performance in such common environments, complicated protection and encapsulation processes are required for organic detectors. In contrast, amorphous semiconductors such

as amorphous silicon (a-Si) are stable with field- proven reliability for optoelectronic applications [7-8]. However, detectors made of a-Si face several issues that compromise the detector performance. The key performance limiting factors include high defect density, which leads to low EQE due to Shockley-Read-Hall carrier recombination, and very low electron and hole mobility, which leads to very low speed [9].

To address the speed problem and operate the device under low voltage, we demonstrate a detector with a very thin (60 nm) layer of a-Si as the light absorption layer. To overcome the problem of low external quantum efficiency due to the thin a-Si light absorption layer, two innovative approaches were employed. First, we used localized surface plasmon resonance (LSPR) effect from Au nanoparticles (NPs) to enhance the light-matter interactions. Second, we used an internal carrier multiplication mechanism in a-Si to amplify the photocurrent. The latter is referred to the cycling excitation process (CEP) reported in our earlier publication [10]. CEP is an internal photocurrent amplification mechanism found in (quasi)disordered materials such as heavily compensated p-n junction and amorphous Si [10-14]. These materials display strong carrier multiplication effect under high electric field due to the large amount of localized states in the bandtails. These bandtailed states can be excited into the mobile bands without the limit of *k*-selection rule that lowers the efficiency for conventional impact ionization. Aided by the plasmonically enhanced light-matter interaction and the CEP effect, a-Si detector can be an attractive alternative to organic semiconductors for light detection on non-semiconducting or compliant substrates.

3.2 Device Design and Fabrication

The device consists of a thin layer of un-doped a-Si sandwiched by two ITO electrodes. Between the a-Si layer and the bottom ITO electrode, there is a layer of randomly distributed Au NPs (40-nm in diameter) to enhance the electromagnetic (EM) field, and thus facilitating the light absorption of the thin a-Si layer via the LSPR effect [15-16]. We chose the dimension of Au nanoparticles based on the localized surface plasmon resonance (LSPR) effect, fabrication process compatibility, and conditions in favor of CEP. The device cross session is shown in Figure 3.1. And Figure 3.2 presents the Scanning Electron Microscope (SEM) image of Au NPs on the bottom ITO electrode.

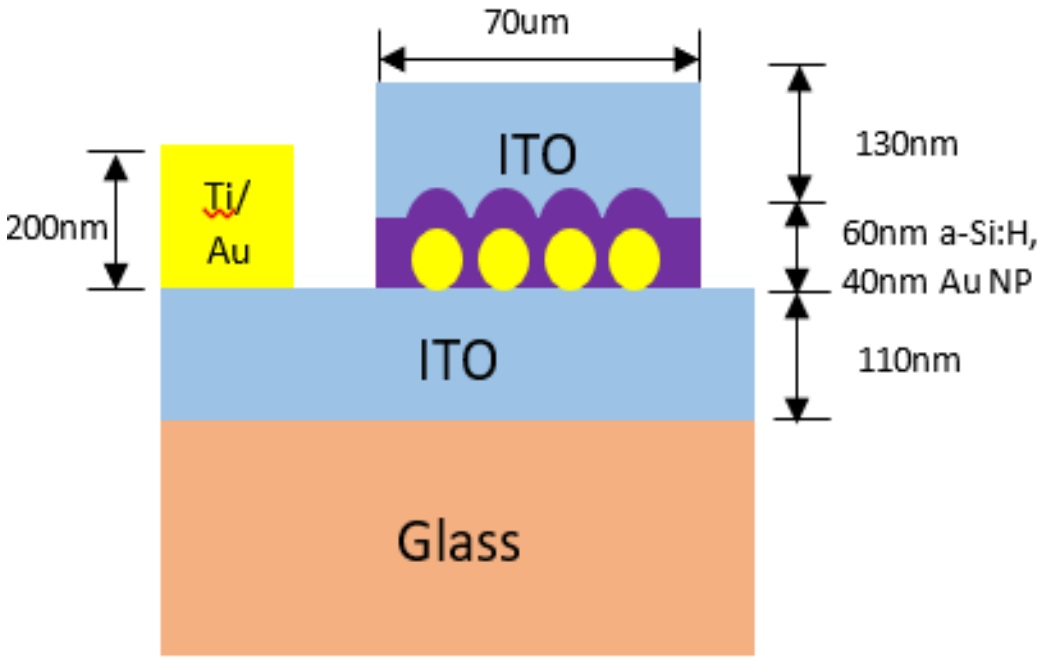

Figure 3.1. Schematic diagram of device structure with material, function and thickness of each layer. Top ITO: 130 nm; amorphous Si: 60 nm; Au NPs: 40 nm in diameter; bottom ITO: 110 nm; Ti / Au: 200 nm. Active area: 70 μm in diameter.

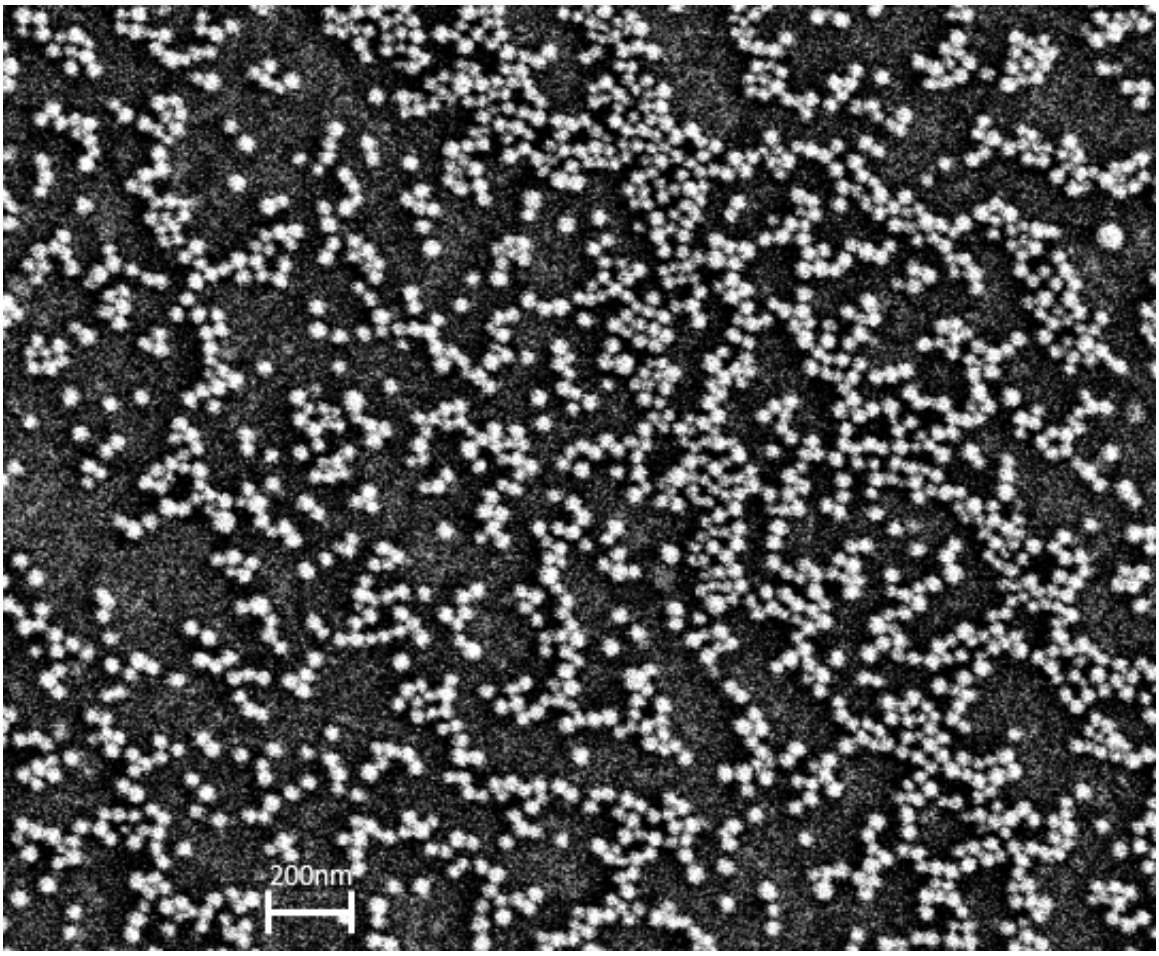

Figure 3.2. Scanning electron microscope (SEM) Image of Au Nanoparticles (NP)

The ITO on glass substrate was firstly solvent cleaned. To improve surface smoothness, ITO/glass substrate was soaked in KOH/isopropanol saturated solution for 2 hours at room temperature. Next, the substrate was rinsed with DI water and baked for 30 minutes. A layer of HMDS adhesion promoter was spin-coated onto the substrate. 1 mg/ml aqueous solution of Au NPs with a core diameter of 40 nm and PVP 40 kDa coating (NanoComposix) was diluted to 0.75 mg/mL with IPA and homogenized with 30 s of sonication. Then the 0.75 mg/mL Au NPs mixed solution was deposited on the substrate by drop coating at 55 °C, followed by 2-hour hard baking at 120 °C. The Au NPs coverage is around 25% measured by SEM. After Au NPs deposition, a 60 nm thick a-Si layer with 5% carbon doping was grown using PECVD. The growth temperature was 270 °C at the substrate and the flow rates were 450 sccm for silane (SiH4) and 24 sccm for methane (CH4). The a-Si film was hydrogen-loaded with H_2 plasma. The first photo-lithography was performed to create photoresist patterns. A 130-nm thick ITO layer was sputtered on the patterned surface and lifted-off to define the top electrode. This ITO layer was also used as etch mask for plasma etch of a-Si in a self-aligned process. The ground contact pad was formed with a 200-nm thick sputtered Ti/Au layer on the bottom ITO electrode.

3.3 DC and Low Frequency Performance

The typical dark current-voltage characteristic of a 70 μm diameter device with Au NPs is shown in Figure 3.3, measured by an Agilent B2912A precision source meter. To characterize device photoresponses, we used single mode fiber-pigtailed laser diodes

modulated at 100 Hz and an SR865A lock-in amplifier to amplify the photocurrent of the device under different DC voltage bias. The laser diodes were driven by a Thorlabs CLD1010 compact laser diode controller modulated by an Agilent 33600A series waveform generator. The measurement setup was controlled by LabView program.

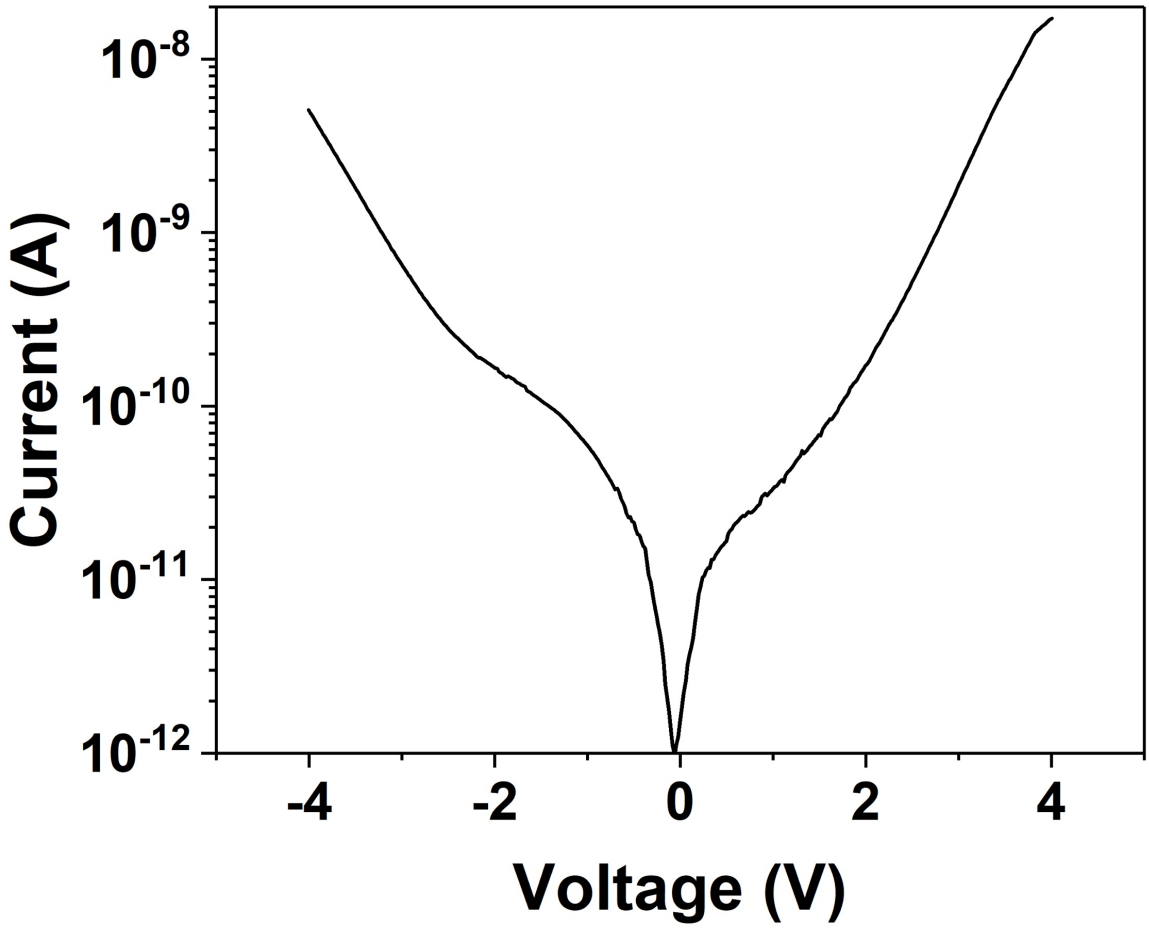

Figure 3.3. A-Si with Au NPs device IV characteristics.

Within the visible light range, we measured the device photoresponse at three wavelengths: red (639 nm), green (518 nm) and blue (488 nm) with incident light power of 350 pW, 80 pW and 70 pW, respectively. The EQE is determined by equation (3.1):

$$EQE = \frac{I_{ph}}{P_{in}} \times \frac{1240}{\lambda(nm)} \tag{3.1}$$

Where I_{ph} is the measured photocurrent, P_{in} is the input power and λ is the measured wavelength. The bias dependent EQE for these three wavelengths is shown in Figure 3.4.

At all three wavelengths, the EQE of devices with Au NPs is appreciably greater than that of the devices without Au NPs, manifesting enhanced light adsorption of a-Si layer due to the LSPR effect. Notably for both devices with and without Au NPs, the EQE increases with voltage bias above 1 V due to the CEP amplification mechanism, which also contributes to high frequency response, to be elucidated later.

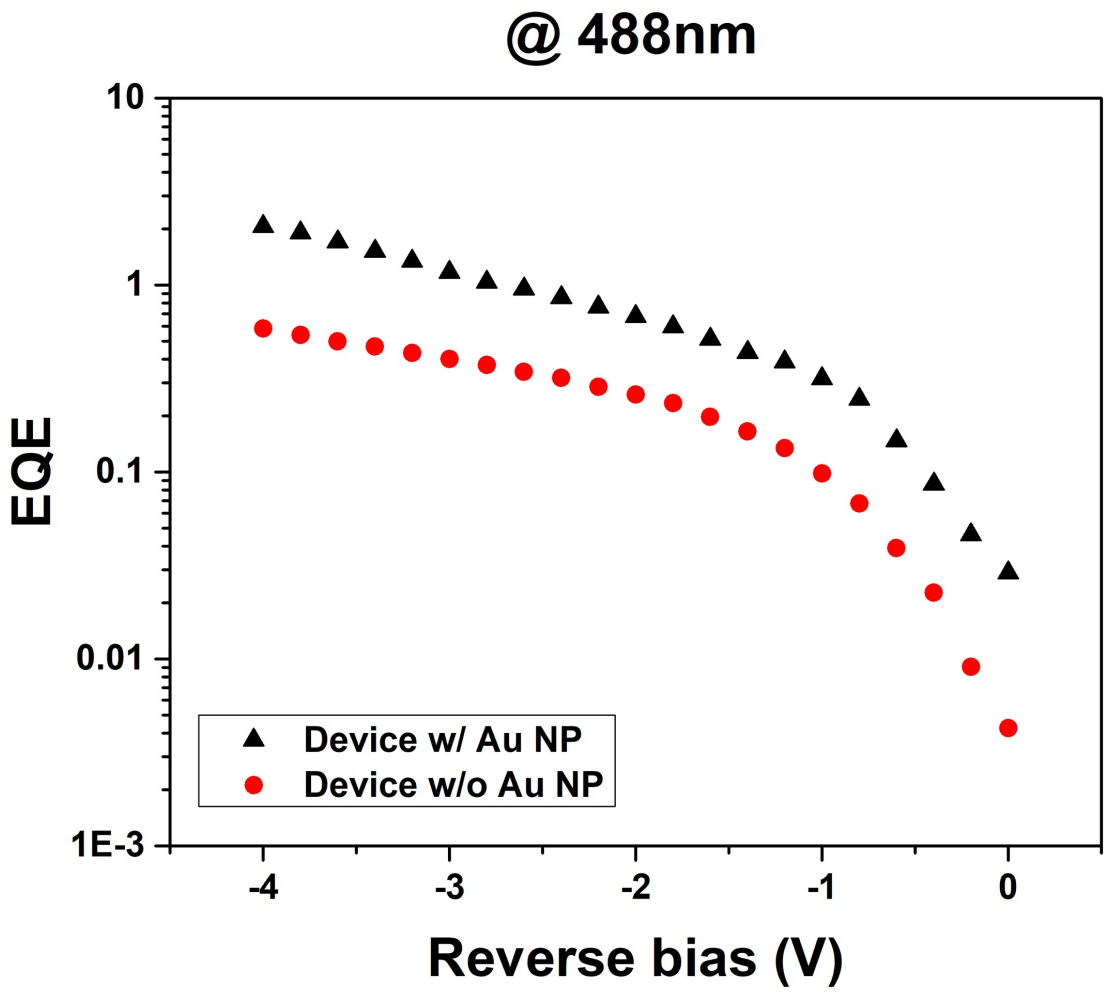

a. For 488 nm (blue) with 70 pW input.

Figure 3.4. Bias Dependent EQE.

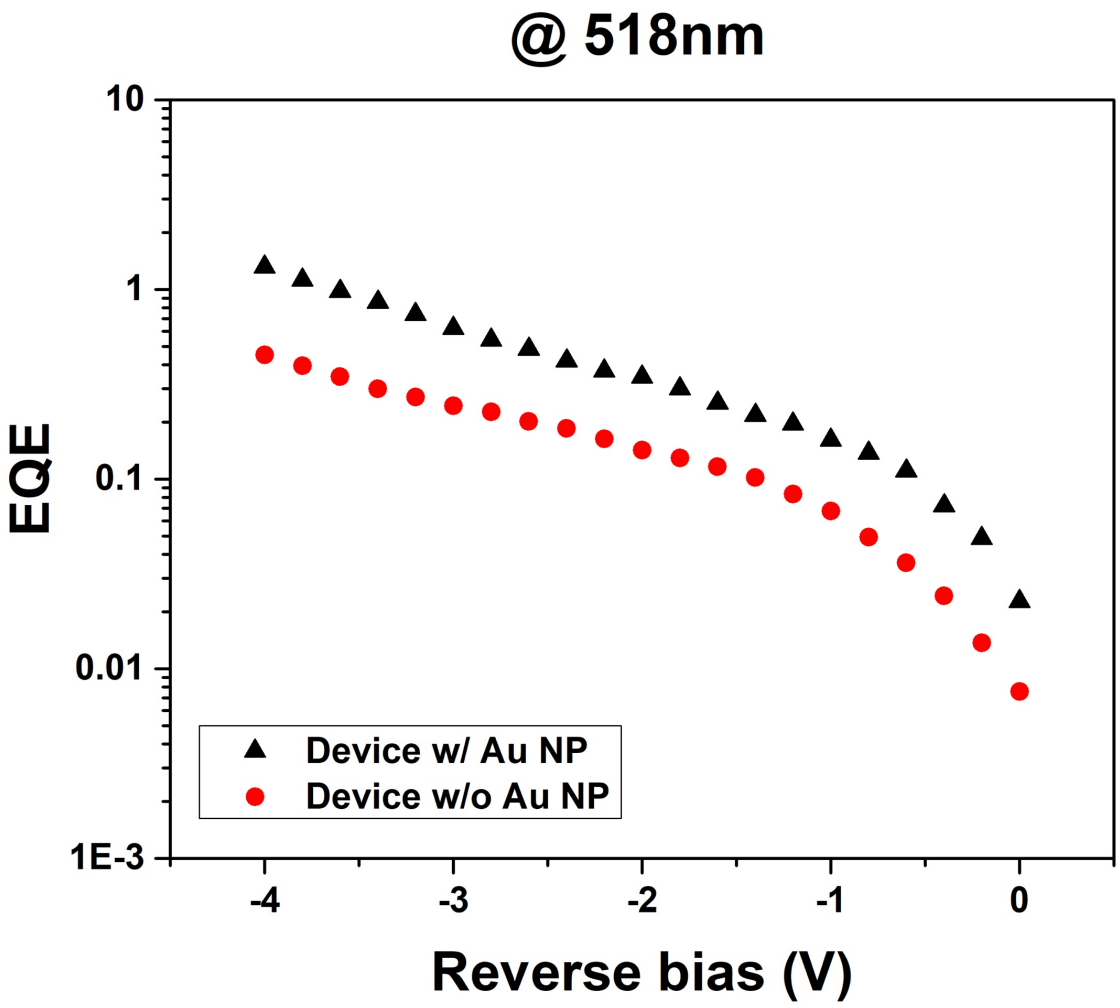

b. For 518 nm (green) with 80 pW input.

Figure 3.4. Bias Dependent EQE, continued.

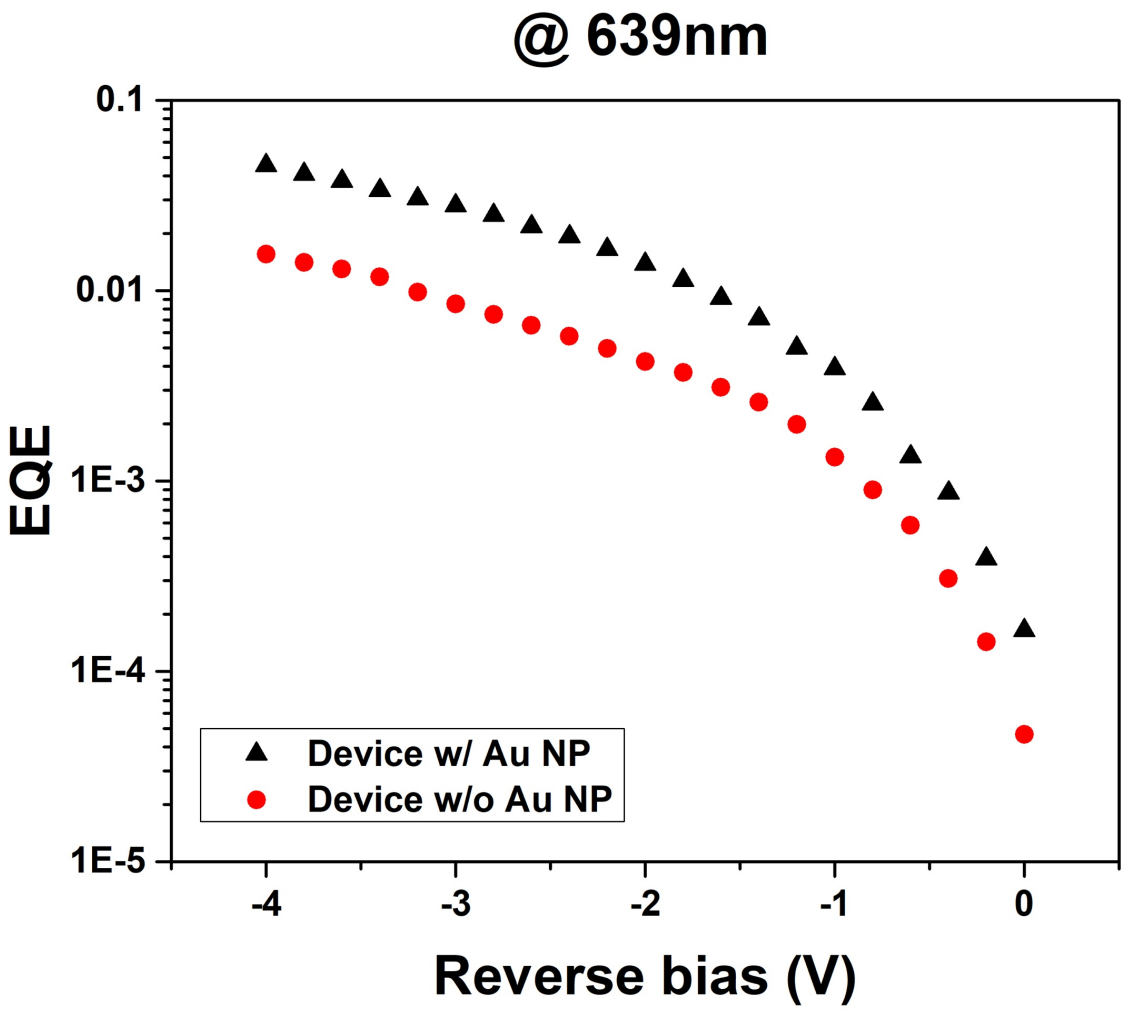

c. For 639 nm (red) with 350 pW input.

Figure 3.4. Bias Dependent EQE, continued.

3.4 High Frequency Characterization

One key performance limit for organic or amorphous semiconductor detectors is their frequency response due to the very low mobility. The slow response of the devices can limit their applications in high frame rate imaging, which is important for applications such as LIDAR for anonymous vehicle and optical communications.

To measure the high frequency characteristics of the devices, we used a high-speed ground-signal-ground (GSG) probe to make device contacts. For small-signal AC tests, the input laser light was modulated by an Agilent N5182A signal generator and the output current from the device was first amplified by an MITEQ AM-1300 low noise amplifier (27 dB voltage gain and 1.4 dB noise figure) and then measured by an HP 8594E spectrum analyzer. Limited by the response of the laser diodes and the bandwidth of Thorlabs CLD1010 laser driver, the small signal AC measurements were made over a range from 200KHz to 1GHz. To characterize the device properties at higher than 1 GHz frequency, we measured the impulse response using 375 nm and 639 nm wavelength picosecond pulsed lasers (PiLas) which produced 40 ps laser pulses at a 1 MHz repetition rate. The measurement setup is the same as small-signal AC test except that the output signal was measured by an Agilent DSO80604B Infiniium High Performance Oscilloscope. The block diagram for high-speed characterization is illustrated in Figure 3.5.

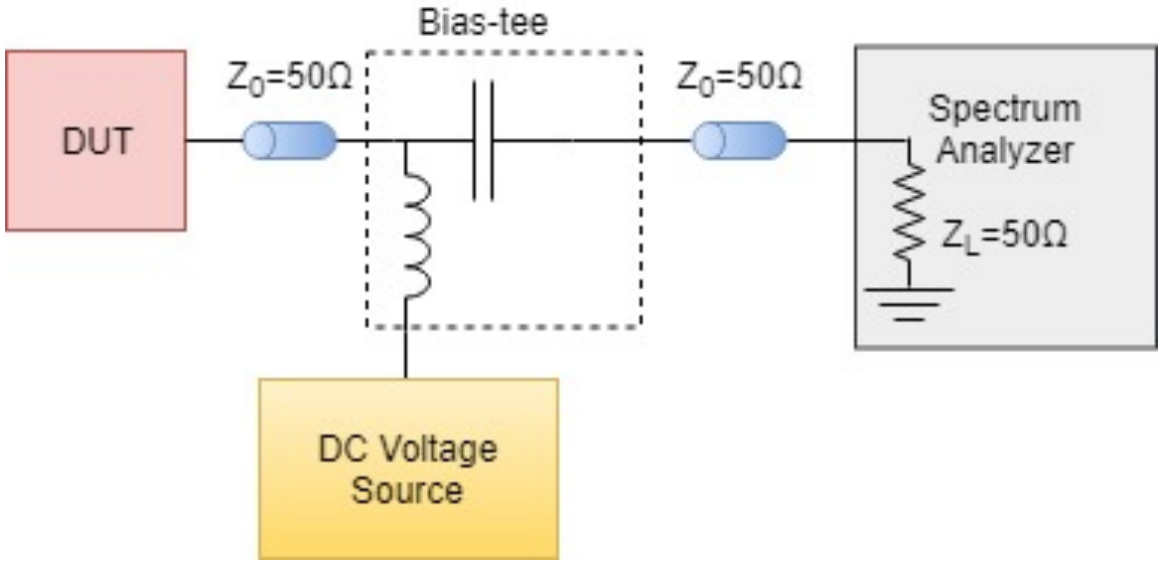

Figure 3.5. Schematic circuit diagram for the high-speed measurement

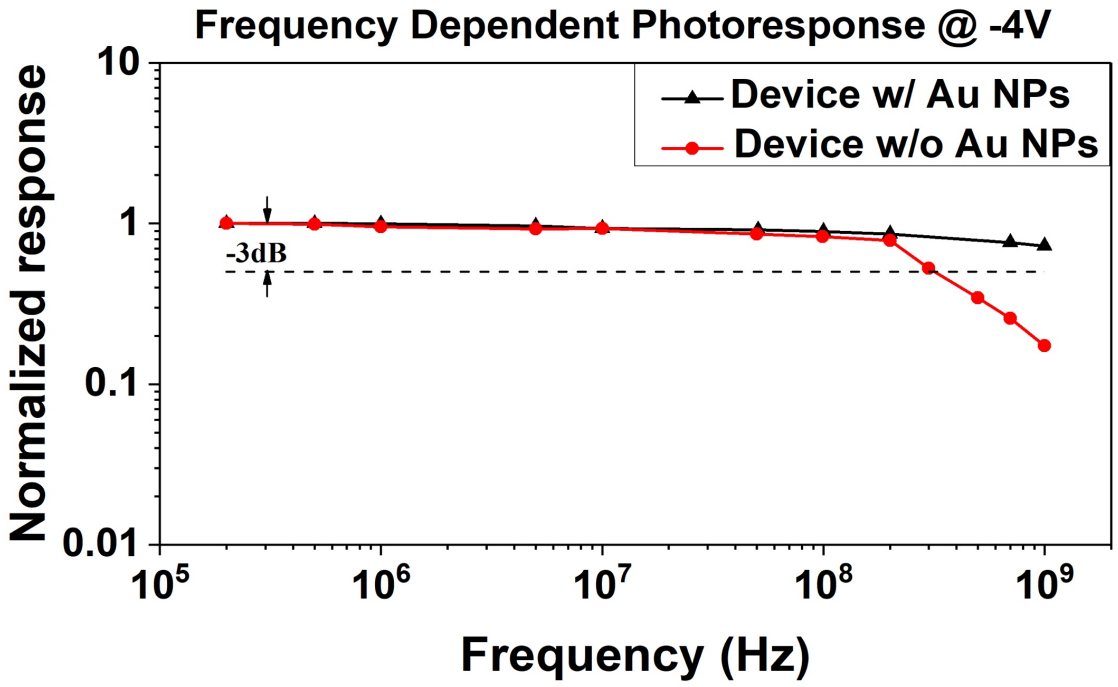

Figure 3.6. Frequency response of 518 nm for devices with and without Au NPs under -4 V, from 200 kHz to 1 GHz. All the responses are normalized with the 200 kHz one. The dash line showed the 3 dB decrease in normalized photoresponse

The small signal frequency response of the detectors at 518 nm wavelength, the desired wavelength for underwater communication [17], is shown in Figure 3.6. Compared with device without Au NPs, which has 3 dB cutoff frequency around 300 MHz, the detector with the help of LSPR achieves a bandwidth of over 1 GHz. This small signal modulation bandwidth is limited by the bandwidth of the 518 nm diode laser, and the actual device bandwidth can be significantly greater. Even with 1 GHz bandwidth, the speed is already more than 10 times faster than the best reported results of solution-processed organic semiconductor photodetectors [18].

To investigate the intrinsic device speed without the limitation of laser driver, the bandwidth of the device with Au NPs was also characterized by its impulse response

using pulsed lasers at 375 nm and 639 nm wavelength. The pulse width of the laser sources is around 40 ps, and the impulse responses of the device with and without Au NPs at 375 nm and 639 nm are shown in Figure 3.7 (a) and (b) respectively. Consistent with the results from small signal measurements, there is an obvious increase on the device speed induced by LSPR. The rise time for devices without Au NP is 240 ps at 375 nm, and its value is reduced to 85 ps for devices with Au NPs. At 639 nm wavelength, the device rise time was reduced from 330 ps to 75 ps due to the incorporation of Au NPs. In terms of the full pulse width at half maximum (FWHM), devices with Au NPs achieve a FWHM of around 170 ps (FWHM) at both wavelengths, while the a-Si devices without Au NPs have a FWHM of 540 ps at 375 nm wavelength and 600 ps at 639 nm wavelength. Apart from the speed increase, the greater peak signal of devices further proves the QE enhancement induced by LSPR. The underlining physics about EQE and speed enhancements of the a-Si detectors with Au NPs will be discussed in the next section.

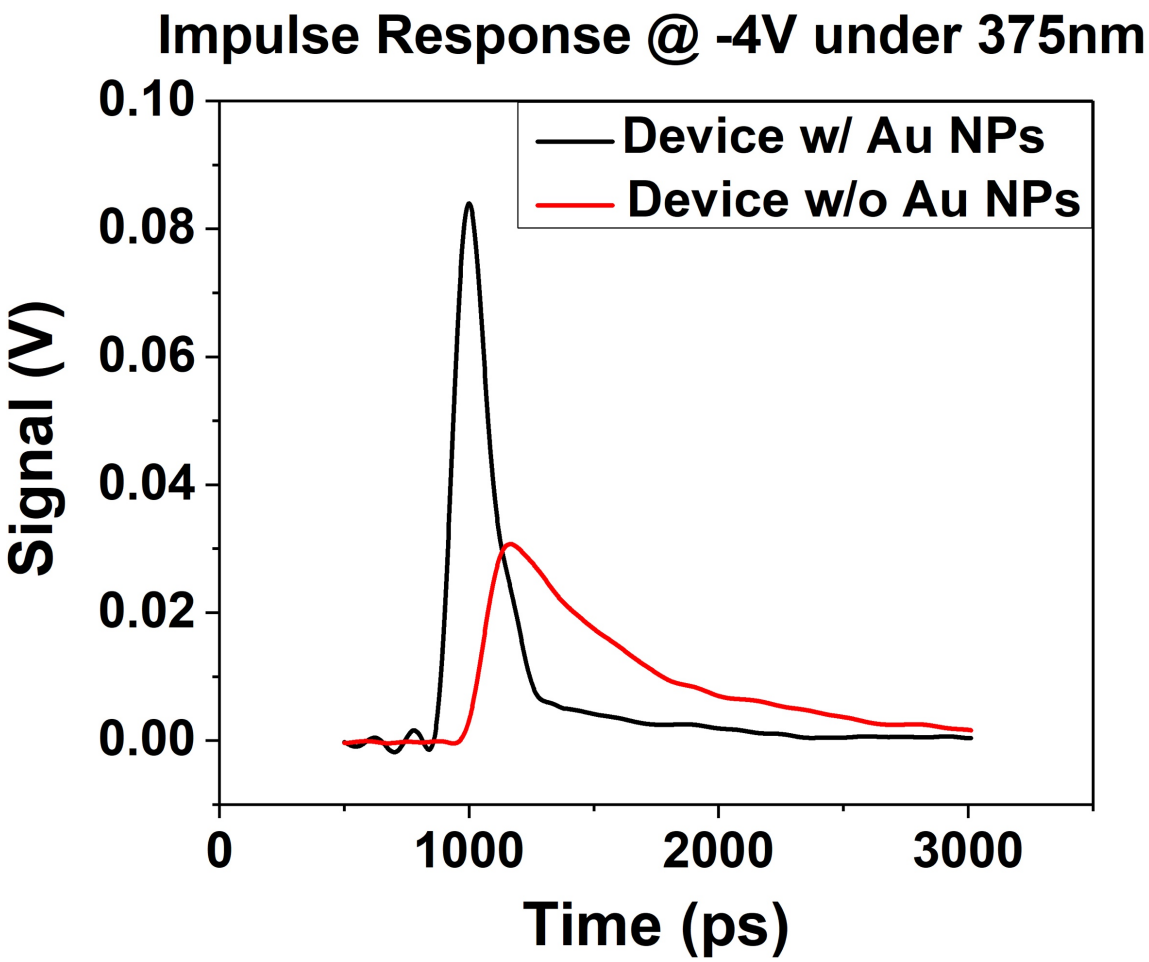

a. 40 ps laser pulses at 375 nm wavelength and1 MHz repetition rate.

Figure 3.7. Impulse response.

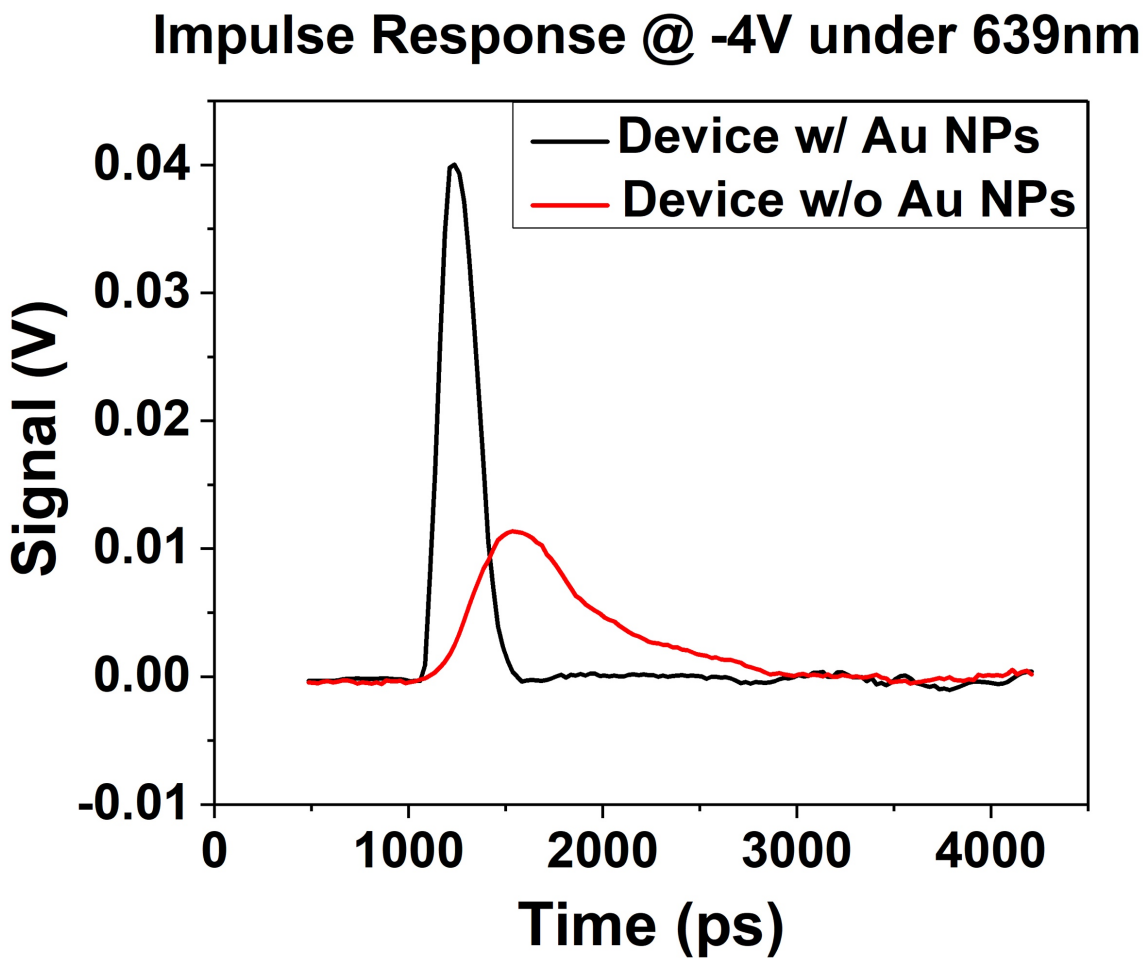

b. 40 ps laser pulses at 639 nm wavelength and 1 MHz repetition rate.

Figure 3.7. Impulse response, continued.

3.5 Electromagnetic Modeling

3.5.1 Simulation Setup

The wavelength dependence of the real and imaginary parts of the refractive index, $n(\lambda)$ and $k(\lambda)$, for 5% C-doped a-Si was measured by Filmetrics, and used in EM simulations with the commercial software COMSOL Multiphysics 4.3, in order to

calculate light absorption with or without addition of Au NPs at different wavelength from the simulated electromagnetic field distribution. The wavelength dependent n and k for 5% C doped a-Si is shown in Figure 3.8.

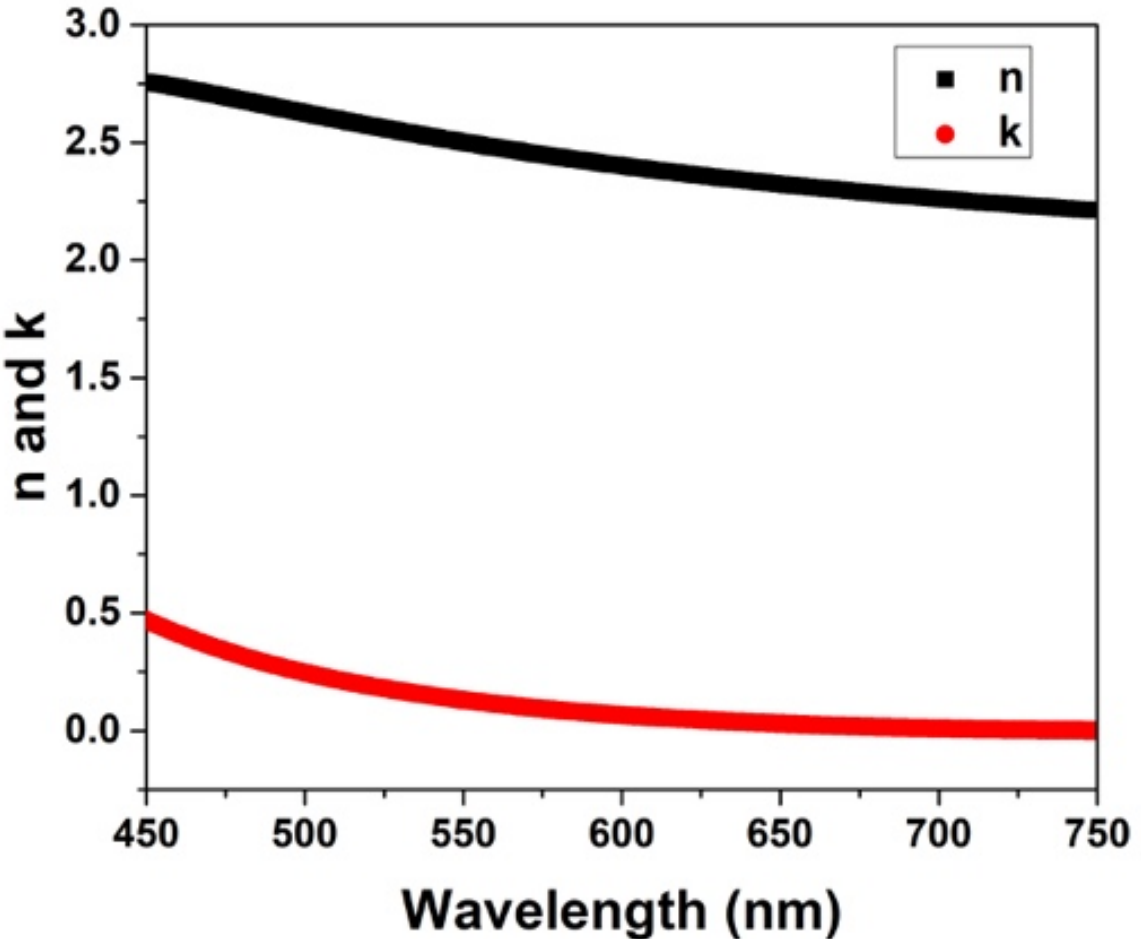

Figure 3.8. Wavelength dependent n & k of 5% C doped a-Si from 450 nm to 750 nm.

When the layer thickness is much smaller than the wavelength, the amount of light absorption is linearly proportional to the input intensity, and the absorption coefficient, $\boldsymbol{\alpha(\lambda)}$, can be calculated from the imaginary part of the wave vector, $\mathbf{k}(\boldsymbol{\lambda})$,

$$\boldsymbol{\alpha(\lambda)} = \frac{\boldsymbol{4\pi k(\lambda)}}{\boldsymbol{\lambda}} \tag{3.2}$$

Then, by performing the integration within the detector volume *V,* we have

$$\int_V \boldsymbol{dI(\vec{r})} = \int_V \boldsymbol{\alpha I(x,y,z) d^2 x dz} \tag{3.3}$$

where x and y directions are identical in our case, and they define he plane normal to the incident light.

The quantum efficiency, η, is defined by the adsorbed light power $\int_V \boldsymbol{dI(\vec{r})}$ divided by the input power $\boldsymbol{P_o}$ as below,

$$\boldsymbol{\eta(\lambda)} = \int_V \boldsymbol{dI(\vec{r})/P_o} = \frac{\boldsymbol{n(\lambda)\alpha(\lambda)}}{\boldsymbol{AE_o^2}} \int_V |\mathrm{E}(\boldsymbol{x,y,z})|^2 \boldsymbol{d^2 x dz} \tag{3.4}$$

where A is the area of the detector, λ is the wavelength in vacuum, E_0 and E are the incident and total electromagnetic field, respectively.

In these EM simulations, the periodicity of a single calculation cell is 70 nm along both the *x* and *y* directions, and the thickness of each layer is consistent with the actual device geometry shown in Figure 3.1. There is one Au NP with a diameter of 40 nm inside the calculation cell, so that the resultant fill factor (~25%) agrees with that of the measured result taken from SEM images, shown in Figure 3.2. Moreover, to take into account the actual device geometry, nanoscale air voids around the lower contact point of the Au NP were introduced into the simulations, which are supposed to be formed because the Au NP was not able to be conformably covered during the PECVD of the a-Si active layer. A 3-D schematic of the a-Si active layer used in the EM simulations is given in Figure 3.9. for clarity.

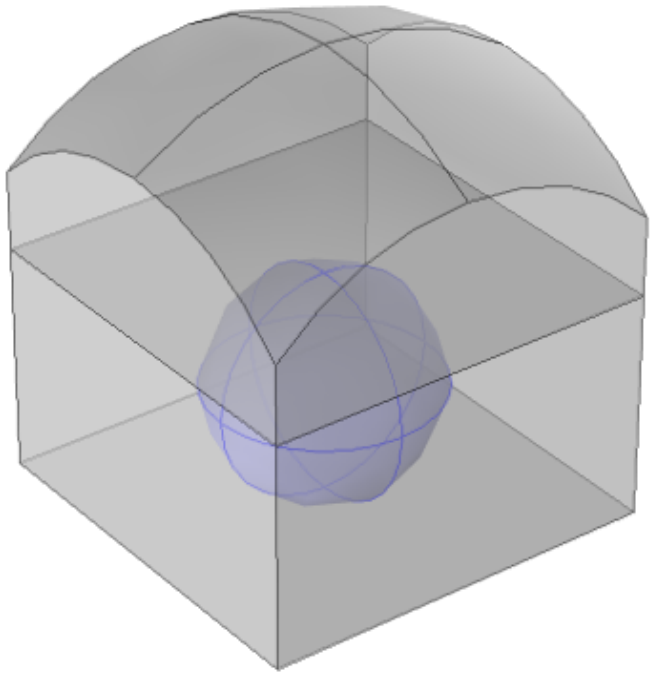

Figure 3.9. 3D structure of the a-Si layer with an Au NP. Diameter of Au NP is 40 nm. The simulation cell is 70 nm in both x and y directions. The thickness of a-Si layer is 60 nm.

3.5.2 Simulation Results

The calculated electric fields at wavelengths of 488 nm, 518 nm, and 639 nm are shown in Figure 3.10. (a, b, c). The electric field in the a-Si active layer is concentrated near the surface of the embedded Au NP due to the LSPR, contributing to the enhancement of the absorption efficiency. The electric field in the a-Si active layer is concentrated near the surface of the embedded Au NP due to the LSPR, contributing to the enhancement of the absorption efficiency.

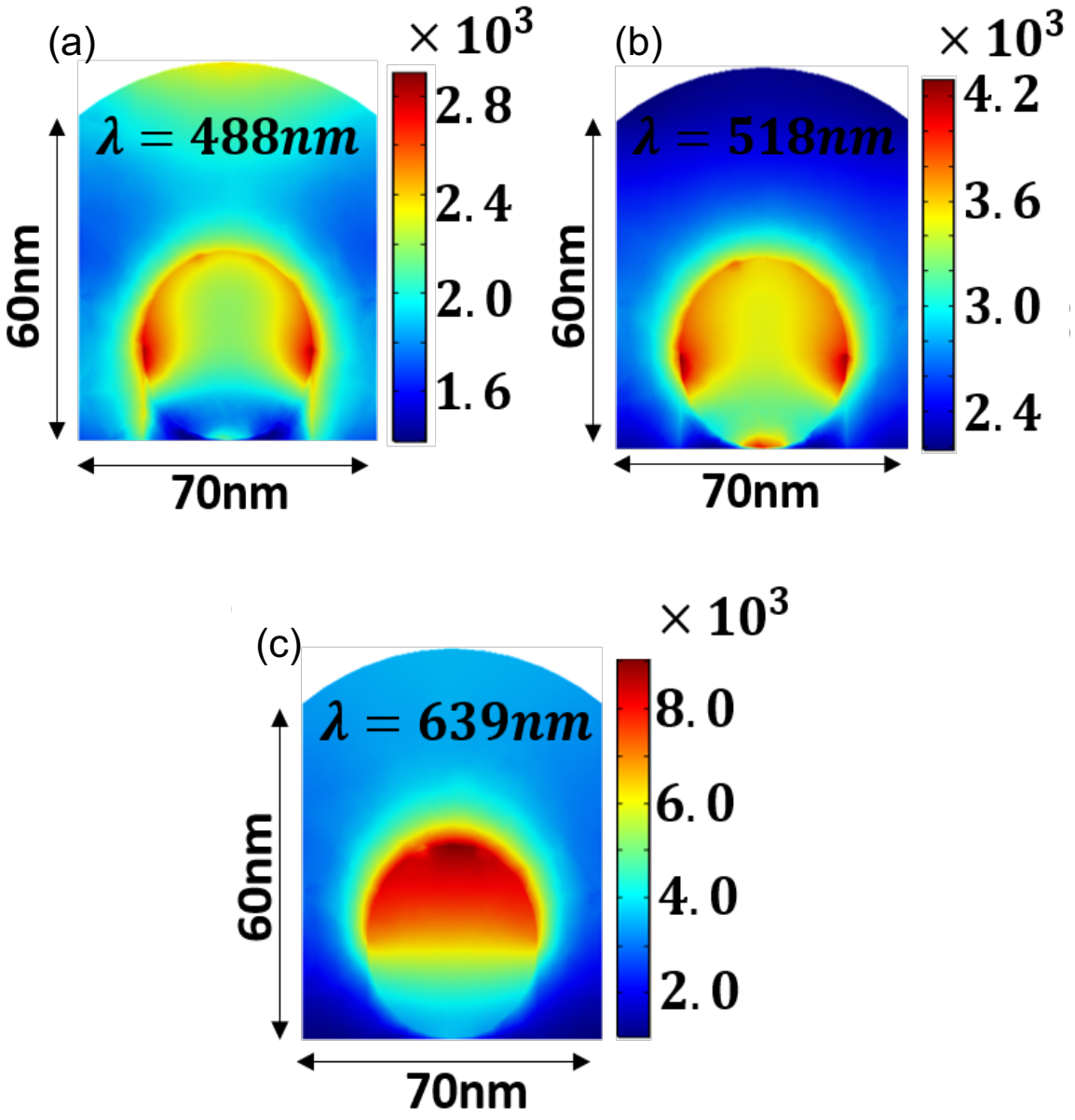

Figure 3.10. 3D EM simulation results of electric field in the a-Si active layer and quantum efficiency enhancement by LSPR effect: (a) 488 nm; (b) 518 nm; (c) 639 nm.

We use equation (3.4) to calculate light absorption at different wavelength from the simulated electromagnetic field distribution. To represent the enhancement due to Au

nanoparticles, we use the ratio of the integrated square of the magnitude of electromagnetic field with and without Au nanoparticles, shown in Figure 3.11.

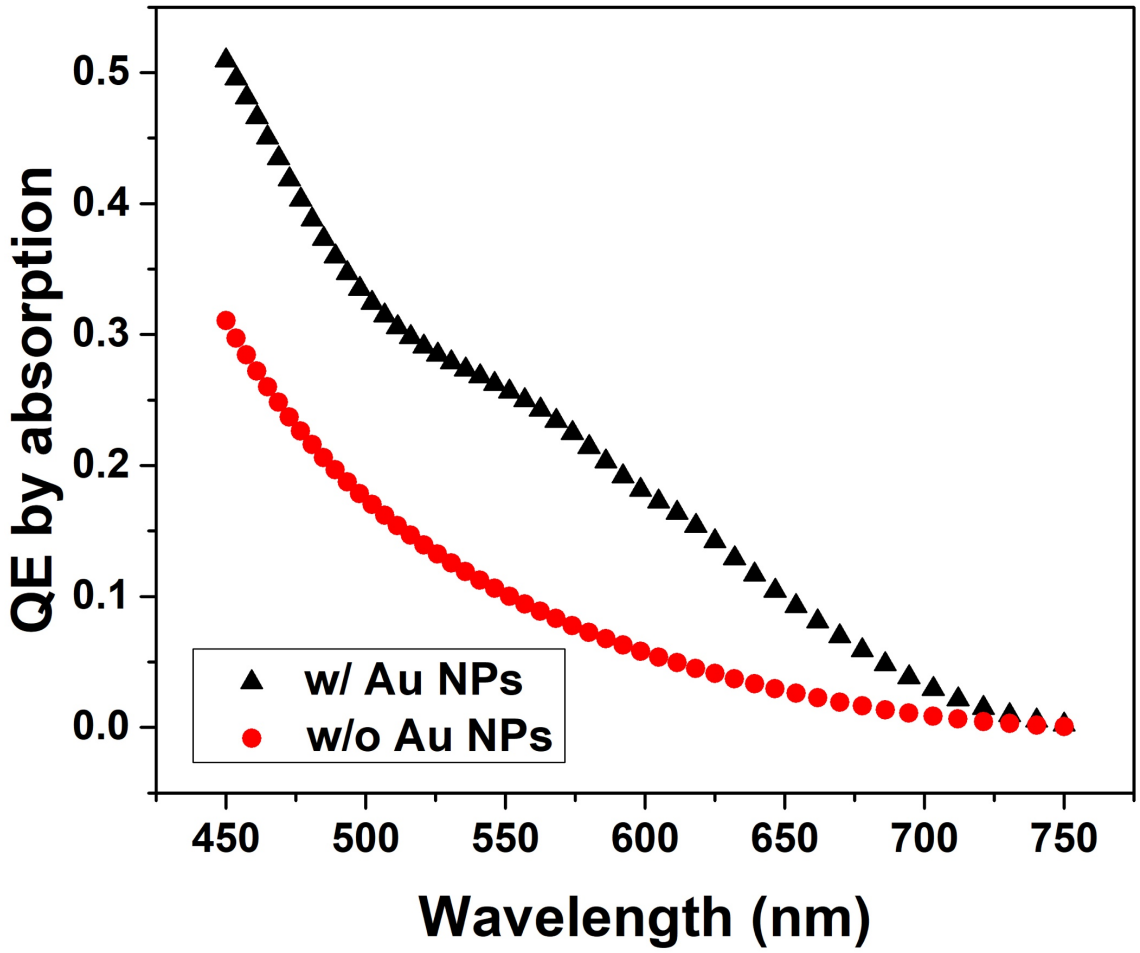

Figure 3.11. Wavelength dependent absorption with and without Au NPs from 3D EM simulation results.

By taking the ratio of the QE by absorption with and without Au NPs, we obtain the QE enhancement after embedding Au NPs into the device, as shown in Figure 3.12. An improved absorption efficiency by factors of 1.6 to 3.8 from 450 nm to 700 nm is

obtained owing to the LSPR near the Au NP. The result is in agreement with the experimental observation shown in Figure 3.4 where the device with Au NPs under -2 V bias exhibits an improved EQE by factors of 2.62 at 488 nm, 2.51 at 518 nm, and 4.72 at 639 nm, respectively**.**

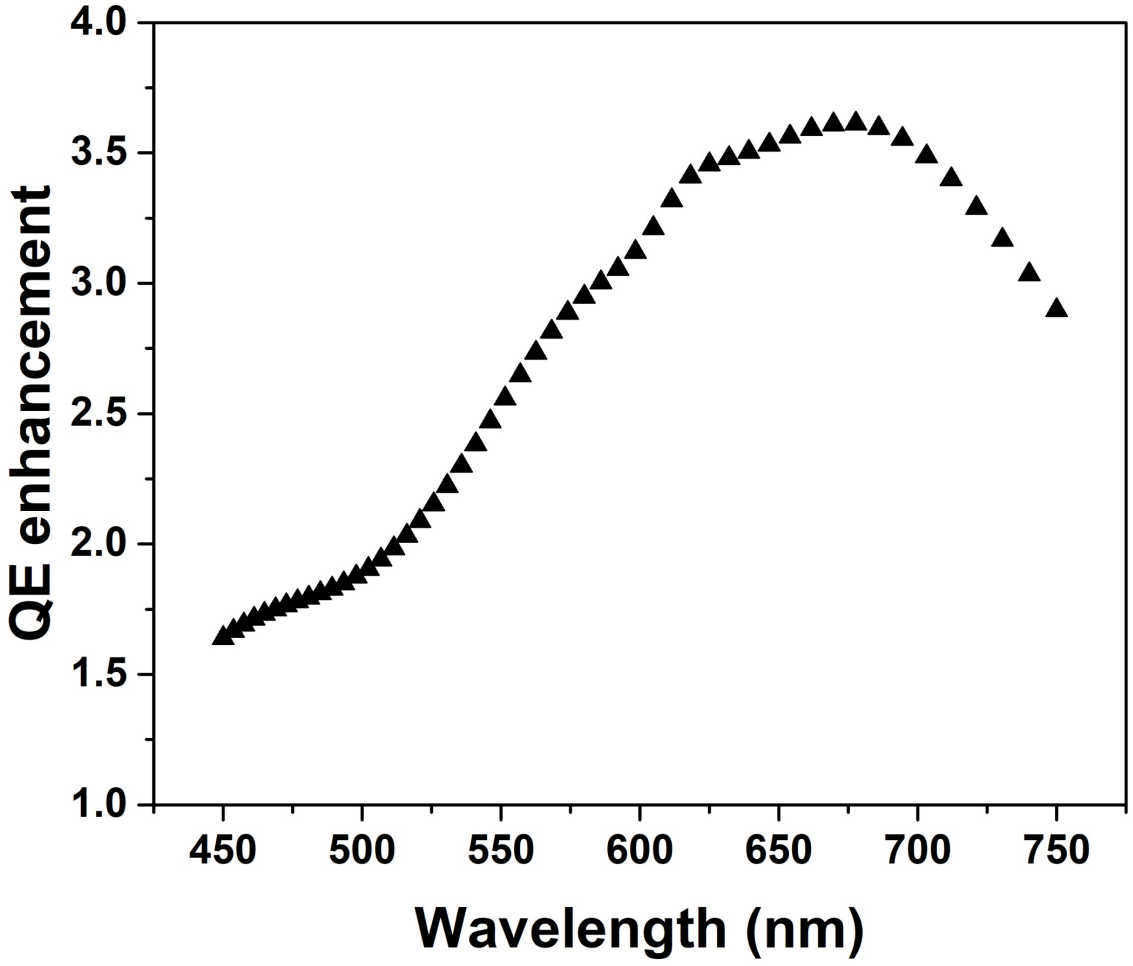

Figure 3.12. QE enhancement factor induced by Au NPs, from 3D EM simulation results.

With the enhancement of electromagnetic field in a-Si near the Au NPs, the amount of the photo-generated electron-hole pairs in the a-Si active layers would be

increased. In addition, the DC electric field under voltage bias is also expected to be enhanced in regions near the Au NPs, giving rise to a good match between the region of light absorption and the region of high E-field to rapidly drive the photogenerated electrons and holes towards their respective electrodes (cathode and anode). To illustrate this effect, the distribution of DC electric field was simulated, and the results are shown in Figure 3.13. Without the Au NP, the DC electric field in the a-Si active layer is uniformly distributed. In contrast, we found that the E-field near the upper half of the particle reaches a much higher level. Even in areas near the upper contact and farthest from the Au NP, the E-field exhibits a comparable value to the device without Au NPs. The EM field distributions in Figure 3.10 and the DC electric field distributions in Figure 3.13 support our hypothesis that the presence of Au NPs creates a good match between the distribution of the EM field and the DC electric field, which favors rapid transport of photogenerated carriers and results in higher frequency responses.

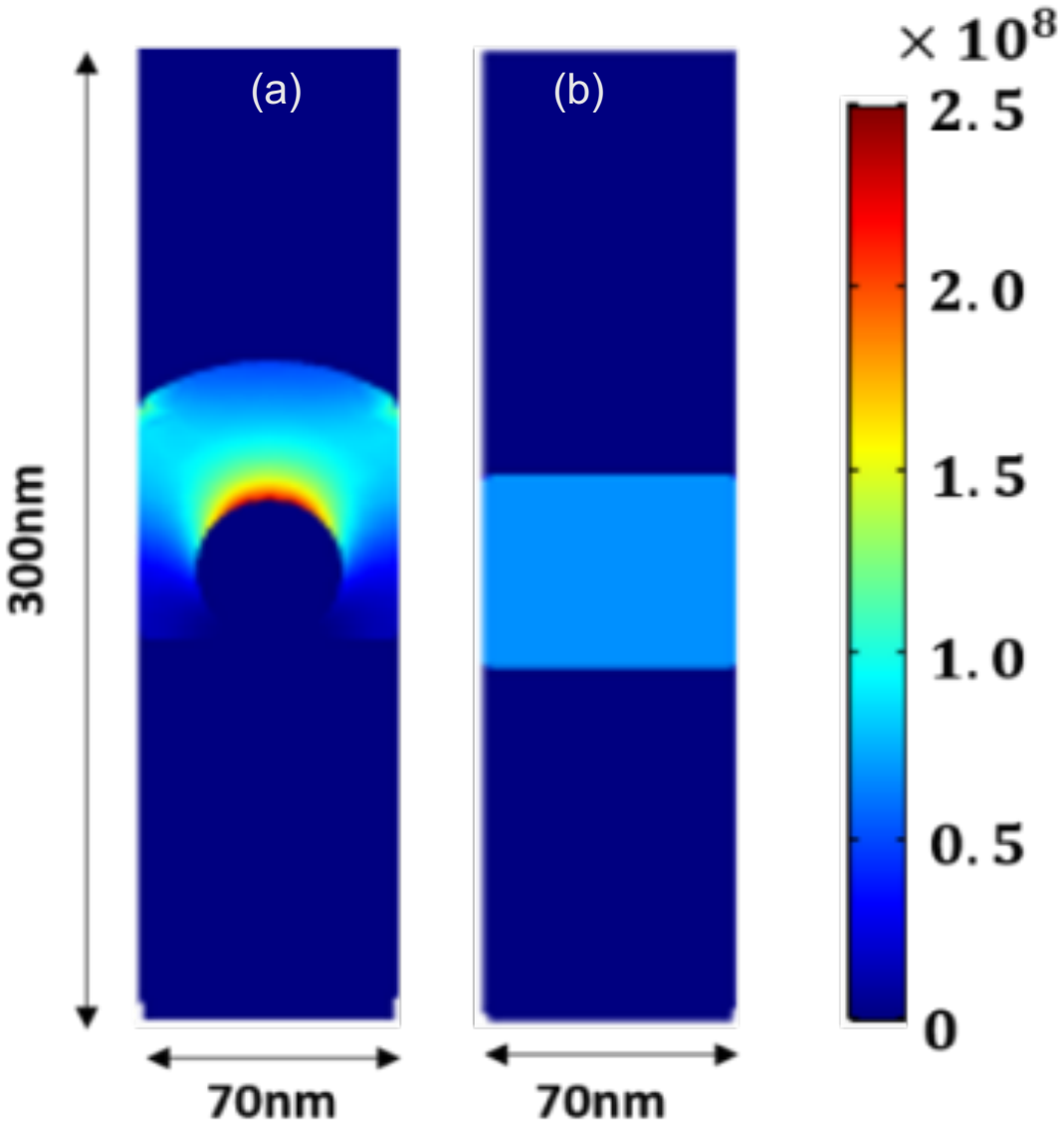

Figure 3.13. DC electric field simulation in the a-Si active layer for (a) device with Au NPs, (b) device without Au NPs.

3.6 Conclusion

We have demonstrated that by using gold nanoparticles embedded in a thin amorphous silicon layer and an effective intrinsic photocurrent amplification mechanism, significant enhancement of the external quantum efficiency and frequency response of photodetectors can be achieved. Adding Au NPs can enhance the external quantum efficiency within the visible light region by approximately a factor of 3. Moreover, CEP amplification mechanism allows achievement of high EQE even with a very thin absorption layer. Besides the improvement of responsivity, the detector has shown a high speed in spite of the material's low electron and hole mobility. We have demonstrated a modulation bandwidth well above 1 GHz and a FWHM of 170 ps. Even though the device has a narrower spectral range of operation than a conventional device because of its thin a-Si:H layer that is essential to achieving high CEP gain and high frequency response, the design has been optimized for blue-green wavelength for applications such as underwater communications, air pollution detection, free-space optical communications, LIDAR, etc. Unlike semiconductor detectors that require high quality, single crystal, rigid substrates and expensive epitaxial growth, amorphous Si thin film detectors can be deposited on various substrates and fabricated in a simple, low cost, and highly scalable process to support emerging applications such as IoT, wearable electronics, flexible displays, autonomous vehicles, and more.

Portions of Chapter 3 have been published in the following publication: Yugang Yu†, **Zihan Xu**†, Shilong Li, Alex Ce Zhang, Lujiang Yan, Zhaowei Liu, and Yu-Hwa Lo. "Plasmonically Enhanced Amorphous Silicon Photodetector with Internal Gain." *IEEE Photonics Technology Letters* 31, no. 12 (2019): 959-962. († These authors contributed equally.) The dissertation author was the co-first author/primary investigator and author of these papers.

References:

[1] Donati, Silvano. "Photodetectors: devices, circuits, and applications." (2001): 653.

[2] Konstantatos, Gerasimos, and Edward H. Sargent. "Nanostructured materials for photon detection." *Nature nanotechnology* 5, no. 6 (2010): 391.

[3] Gong, Xiong, Minghong Tong, Yangjun Xia, Wanzhu Cai, Ji Sun Moon, Yong Cao, Gang Yu, Chan-Long Shieh, Boo Nilsson, and Alan J. Heeger. "High-detectivity polymer photodetectors with spectral response from 300 nm to 1450 nm." *Science* 325, no. 5948 (2009): 1665-1667.

[4] Yao, Yan, Yongye Liang, Vishal Shrotriya, Shengqiang Xiao, Luping Yu, and Yang Yang. "Plastic near‐infrared photodetectors utilizing low band gap polymer." *Advanced Materials* 19, no. 22 (2007): 3979-3983.

[5] Asghar, M. I., J. Zhang, H. Wang, and P. D. Lund. "Device stability of perovskite solar cells–A review." *Renewable and Sustainable Energy Reviews* 77 (2017): 131-146.

[6] Thomas, Simil, Jack Ly, Lei Zhang, Alejandro L. Briseno, and Jean-Luc Bredas. "Improving the stability of organic semiconductors: Distortion energy versus aromaticity in substituted bistetracene." *Chemistry of Materials* 28, no. 23 (2016): 8504-8512.

[7] Carlson, David E., and Cristopher R. Wronski. "Amorphous silicon solar cell." *Applied Physics Letters* 28, no. 11 (1976): 671-673.

[8] Cocorullo, Giuseppe, Francesco G. Della Corte, R. De Rosa, Ivo Rendina, A. Rubino, and E. Terzini. "Amorphous silicon-based guided-wave passive and active devices for silicon integrated optoelectronics." *IEEE Journal of selected topics in quantum electronics* 4, no. 6 (1998): 997-1002.

[9] Sakata, I., and Y. Hayashi. "Theoretical analysis of trapping and recombination of photogenerated carriers in amorphous silicon solar cells." *Applied Physics A* 37, no. 3 (1985): 153-164.

[10] Yan, Lujiang, Yugang Yu, Alex Ce Zhang, David Hall, Iftikhar Ahmad Niaz, Mohammad Abu Raihan Miah, Yu-Hsin Liu, and Yu-Hwa Lo. "An amorphous silicon photodiode with 2 THz gain-bandwidth product based on cycling excitation process." *Applied Physics Letters* 111, no. 10 (2017): 101104.

[11] Liu, Yu-Hsin, Alex Zhang, Mohammad Abu Raihan Miah, David Hall, Ifikhar Ahmad Niaz, Lujiang Yan, Yugang Yu, Mahmut S. Kavrik, and Yu-Hwa Lo. "Cycling excitation process for light detection and signal amplification in semiconductors." In *Optical Sensing, Imaging, and Photon Counting: Nanostructured Devices and Applications 2016*, vol. 9933, p. 99330C. International Society for Optics and Photonics, 2016.

[12] Hall, David, Yu-Hsin Liu, Lujiang Yan, Yugang Yu, and Yu-Hwa Lo. "Approaching the quantum limit of photodetection in solid-state photodetectors." *IEEE Transactions on Electron Devices* 64, no. 12 (2017): 4812-4822.

[13] Link, Stephan, and Mostafa A. El-Sayed. "Optical properties and ultrafast dynamics of metallic nanocrystals." *Annual review of physical chemistry* 54, no. 1 (2003): 331-366.

[14] Mulvaney, Paul. "Surface plasmon spectroscopy of nanosized metal particles." *Langmuir* 12, no. 3 (1996): 788-800.

[15] Schill, Felix, Uwe R. Zimmer, and Jochen Trumpf. "Visible spectrum optical communication and distance sensing for underwater applications." In *Proceedings of ACRA*, vol. 2004, pp. 1-8. 2004.

[16] Shen, Liang, Yanjun Fang, Dong Wang, Yang Bai, Yehao Deng, Mengmeng Wang, Yongfeng Lu, and Jinsong Huang. "A Self-Powered, Sub-nanosecond-Response Solution-Processed Hybrid Perovskite Photodetector for Time-Resolved Photoluminescence-Lifetime Detection." *Advanced Materials* 28, no. 48 (2016): 10794-10800.

[17] Auston, D. H., P. Lavallard, N. Sol, and D. Kaplan. "An amorphous silicon photodetector for picosecond pulses." *Applied Physics Letters* 36, no. 1 (1980): 66-68.

[18] Salamin, Yannick, Ping Ma, Benedikt Baeuerle, Alexandros Emboras, Yuriy Fedoryshyn, Wolfgang Heni, Bojun Cheng, Arne Josten, and Juerg Leuthold. "100 GHz plasmonic photodetector." *ACS photonics* 5, no. 8 (2018): 3291-3297.

Chapter 4: Two Regimes Photodetection in Perovskite

4.1 Introduction

Organometallic halide perovskites have extraordinary optical-electrical conversion efficiency as photovoltaic devices and enormous responsivity as photodetectors [1-11]. One general observation among all perovskite detectors is that its photoresponsivity is sensitive to the input light intensity. As the light intensity increases, the responsivity decreases. However, to our best knowledge, there have been no systematic studies about power and frequency dependent responsivity for perovskite detectors. Several groups have reported high frequency response without specifying the power level and the corresponding responsivity at high frequency [12-14]. Other groups reported power dependent responsivity under DC measurements, without considering the frequency dependence of responsivity [15-16]. We believe a comprehensive study of photoresponsivity of perovskite devices under different frequencies and optical power levels is important not only from application point of view but also for understanding the physics of optical process in Organometallic halide perovskites. In this paper we probed solution processed polycrystalline methylammonium lead iodide ($MAPbI_3$) to investigate its power and frequency dependent photoresponse. By doing so, we observed several interesting characteristics that shed light on the intrinsic physical mechanisms of perovskite detectors and new opportunities for applications.

We found that over the frequency range from 5 Hz to 800 MHz, the device photoresponsivity decreases with the input optical power following the relation $R \propto P^{-\alpha}$ with $\alpha \sim 0.4$ and P being the input light power. This relation holds over a wide frequency

range of more than 8 orders of magnitude. Over this frequency range, the temporal response of the detector follows the waveform of the modulating light intensity. However, as we investigated the extremely low frequency response (near DC), we found that the perovskite detectors display the characteristics of persistent photoconductivity with very slow response. In this regime, the power dependent photoresponsivity mostly follows the relation $R \propto P^{-\beta}$ with $\beta \sim 0.9$. Most strikingly, we found that in the low frequency or persistent photoresponsivity regime, the device can respond to single photons. Our detailed study shows that in the extremely low light intensity regime where less than 10 photons are absorbed by the device, the photoresponse is actually proportional to the input photon number (i.e. $R \propto N$ with N being the number of photons absorbed by the perovskite material). However, as the photon number increases, the photoresponse enters the regime of $R \propto P^{-\beta}$ with $\beta \sim 0.9$. In this paper we report the detailed measurement results in different frequencies and power levels down to single digit photons. We also propose possible mechanisms causing such unique characteristics for perovskite devices.

4.2 Device Design and Fabrication

The testing platform has a vertical structure consisting of indium tin oxide (ITO; 180 nm-thickness)/perovskite (400 nm)/ ITO (110 nm) with an active area of 7 μm in diameter. A 3d model as well the top layout are shown in Figure 4.1.a. Device dark IV characteristic as well as the top view of a probed device with scale are shown in Figure 4.1.b. The detailed fabrication process is illustrated in Figure 4.2.

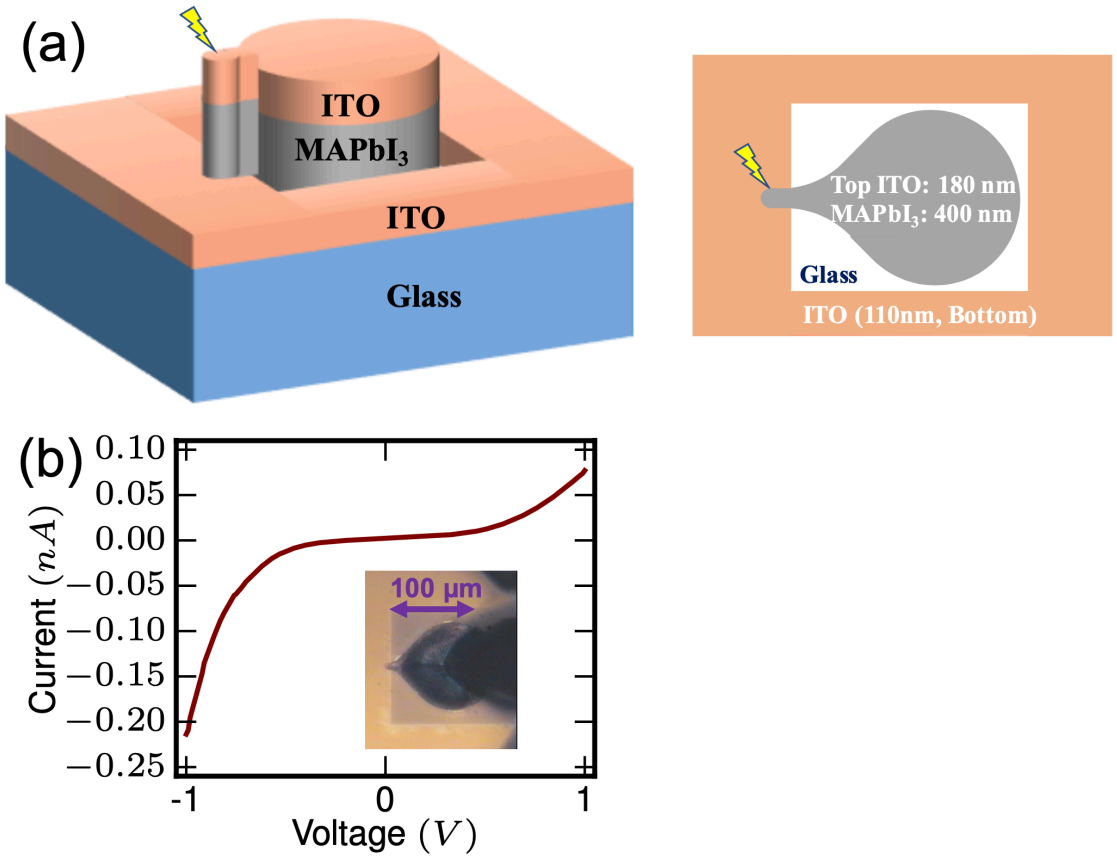

Figure 4.1. Device layout and dark IV (a) Schematic diagram of device structure with material and thickness of each layer (3D and top view), (b) Dark IV Characteristics and the micrograph of a probed device.

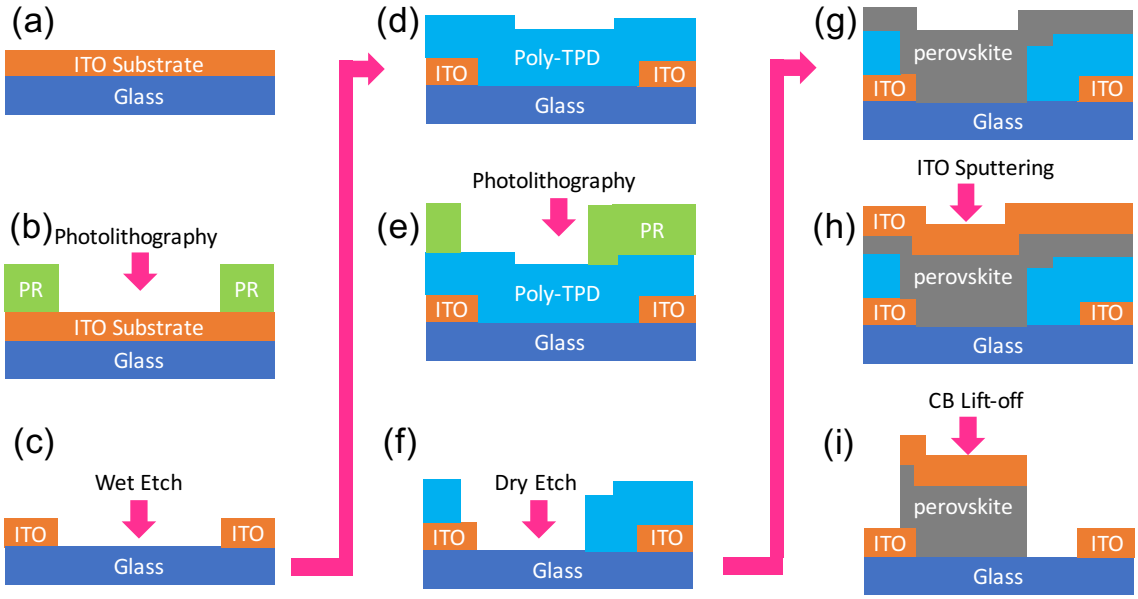

Figure 4.2. Fabrication process. (a) Cleaned ITO glass substrate with Cr/Au alignment markers. Cr/Au alignment markers are in the center and 4 corners of a substrate, not shown in the device region. (b) Photolithography for wet etch mask. (c) Wet-etching of ITO. (d) Spin-coating of poly-TPD. (e) Photolithography for dry etch mask. (f) Dry-etching of poly-TPD. (g) Spin-coating of perovskite and post bake. (h) ITO sputtering. (i) Lift-off in CB.

For the solution preparation, we dissolved poly-TPD (40 mg) in 2mL Chlorobenzene (CB) in N_2 glovebox to get the 20 mg/mL solution. $CH_3NH_3PbI_3$ was prepared by mixing CH_3NH_3I (795 mg) and PbI_2 (2.3 g, 1:1 molar ratio) into DMF (2648 µl) and DMSO (323 µL) mixed solvents. All the solutions were magnetically stirred at 60 ^oC and 1200 rpm for more than 12 hours.

An ITO-deposited glass substrate was sonically cleaned in acetone, methanol, IPA and deionized water (DI water) sequentially and then blown dry with N_2. After the solvent cleaning, the ITO substrate was dipped in saturated KOH containing IPA solution for one hour then rinsed with IPA and DI water and blown dry with N_2. Before spin-coating of photoresist, the ITO substrate was baked at 120 ºC for 30 minutes to remove adsorbed moisture at the film surface and then cooled to room temperature. For all the photolithography steps, we spin-coated negative photoresist (NR9-1500) with 3500 rpm for 45 seconds to obtain a photoresist layer thickness of around 1.5 µm. All the photolithography exposure steps were performed by a laser writer (Heidelberg MLA150). After the patterning we sputtered Cr (20 nm)/Au (100 nm) and lifted off in acetone. Cr/Au patterns were also formed as alignment markers for subsequent photolithography steps (Figure 4.2.a).

We carried out another photolithography step (Figure 4.2.b) to pattern the bottom ITO layer by wet-etching with 50%-HCl (Figure 4.2.c). Right before poly-TPD spin-coating, the patterned ITO substrate was baked at 120 ^oC for 30 minutes and then cooled down to room temperature. The 20 mg/mL poly-TPD solution was spin-coated with 600 rpm for 45 seconds, followed by 150 ^oC post bake for 30 minutes (Figure 4.2.d). Using

the patterned NR9-1500 as the mask (Figure 4.2.e), we performed O_2 plasma etch of the poly-TPD layer. The photoresist was removed with acetone. The wafer was rinsed with DI water and blown dry with N_2 (Figure 4.2.f). The perovskite solution was spin-coated onto the patterned substrate with 3500 rpm for 40 second. At the 10^{th} second during spin-coating, 1 mL Ether was sprayed on the substrate. Then the sample was baked at 70 ^{o}C for 15 minutes (Figure 4.2.g). The resultant perovskite layer is around 400 nm thick. A layer of 180 nm-ITO was then sputtered onto the samples (Figure 4.2.h). After overnight lift-off in Chlorobenzene (CB) (Figure 4.2.i), the sample was rinsed with CB and then blown dry with N_2. The last step Chlorobenzene (CB) lift-off is critical to the overall device yield and performance. Unlike conventional photoresist lift-off process in acetone, to facilitate the CB lift-off process, we have created a smooth contour for the top ITO electrode (Figure 4.1.a) and a larger contact pad (100 μm diameter). Regarding the asymmetric dark IV in Figure 4.1.b, it is likely that the bottom ITO layer from a commercial ITO-on-glass substrate has slightly different properties than the sputtered top ITO layer formed in our laboratory. Depending on the method of deposition and deposition condition, the work function of the ITO layer can vary, causing asymmetric I-V characteristics.

4.3 Photoresponse Characterization

4.3.1 Optical Setup

In the optical setup for photoresponse characterization, the two beam-splitter system couples both the input laser light and the illuminating light source onto the device

under test (DUT), allowing us to visualize the device position as well as the beam spot through a CCD camera. Before the first beam-splitter, there is a lens to focus the input laser beam spot. A neutral density filter is placed in front of the focusing lens to attenuate the light power.

To avoid stray light, the perovskite photodetector device was put in a dark box. The device was electrically contacted with a ground-signal-ground (GSG) probe, with the output terminal connected to a Keysight B2902A precision source meter for slow response measurement and IV characterization. The optical input was from single mode fiber-pigtailed laser diodes of different wavelengths, driven by a Thorlabs CLD1010 compact laser diode controller.

4.3.2 Frequency Dependent Characterization

For frequency dependent characterization, the device was biased at 1V and contacted with a GSG probe. Due to instrumental limits, we have measured the frequency response using two instruments: a lock-in amplifier from 5 Hz ~ 10 kHz and a vector analyzer and amplifier from 500 kHz to 800 MHz range. In the frequency range from 5 Hz to 10k Hz, the photocurrent was measured by a lock-in amplifier SR865A following a low-noise current pre-amplifier SR570. In the frequency range from 500 KHz to 800 MHz, the input light was modulated by Agilent N5182A, and the output photocurrent was measured by a HP 89410A vector signal analyzer with the pre-amplifier on.

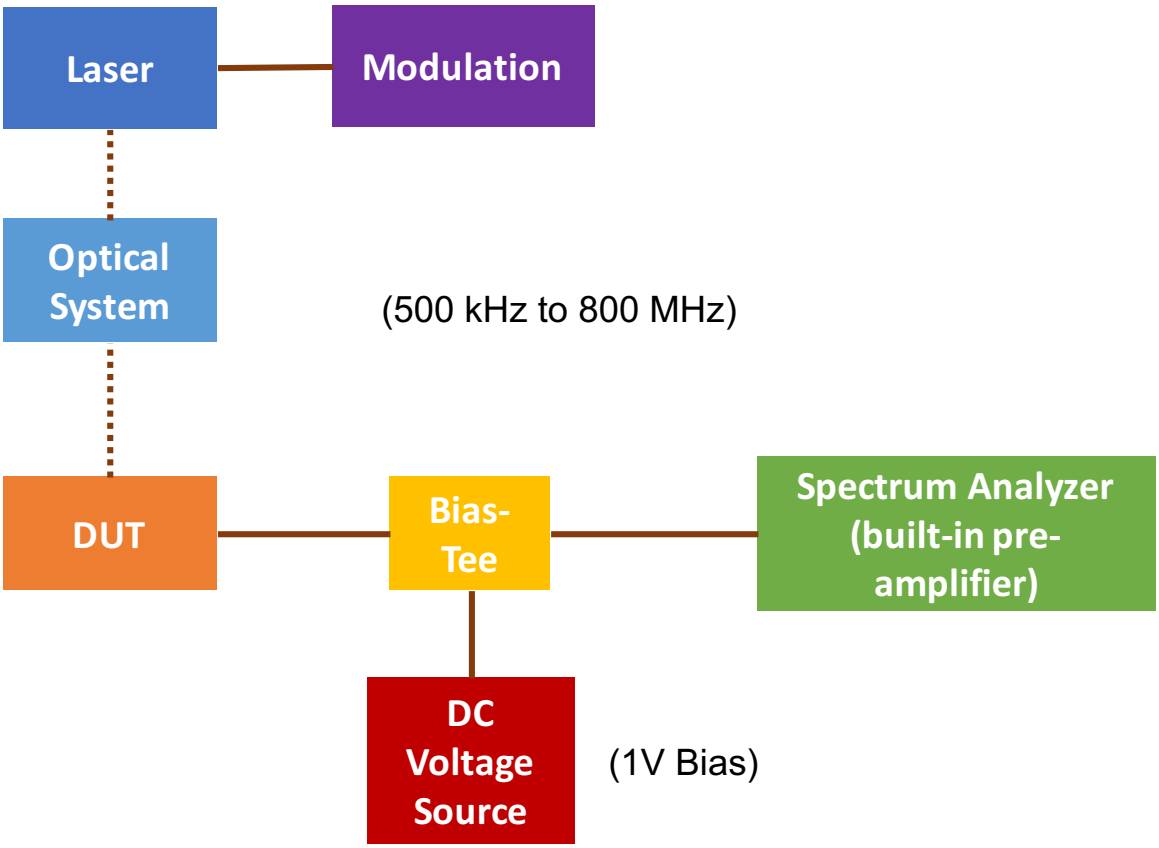

Figure 4.3. Setup for High-Frequency Characterization. Dash lines are for optical coupling and solid lines are for electrical connection.

4.3.3 Quasi-Persistent Photoresponse Characterization

In slow response characterization, the laser was modulated by an Agilent 33600A series waveform generator to generate a series of 200 ms rectangular pulses in a manner described below. To record the device response to a single 200ms optical pulse at a given power level, we programmed a LabVIEW file to control the device bias and optical pulses. At first the bias on the device was ramped from 0 V to 1 V at a rate of 0.2 V s^{-1}. After reaching 1 V bias, the waveform generator sent a single 200 ms laser pulse at the

10^{th} second (i.e. 5 seconds after the device is biased at 1V) and the program started to collect the data for time dependent photocurrent, which is the total current subtracted by the dark current. It was observed that the photocurrent response to a single optical pulse rose with a time constant of the order of 10 seconds (0.1Hz) till a constant current level was reached. Then the current output remains at the level in a manner of persistent photocurrent. Then the LabVIEW program reset the device by reducing its bias voltage to 0V, causing the current level to drop to zero in less than 140 seconds. After resting the device at zero bias for 3 minutes, the bias was ramped to 1V again following the same cycle as before. In this manner, a series of perovskite detector response to a single optical pulse at given optical power level was measured.

4.3.4 Absorbed Optical Power Calibration

We used 4 different structures, ITO/ glass (substrate), ITO/ ITO/ glass, perovskite/ ITO/ glass, and ITO/ perovskite/ ITO/ glass to carefully calibrate the amount of light absorbed by the perovskite layer. We used Filmetrics profilometer to measure reflectivity and the percentage of transmitted light at different wavelengths. The fraction of light absorption by the perovskite layer in the ITO/ perovskite/ ITO /glass structure was characterized to be 0.75 at 518 nm wavelength and 0.68 at 639 nm wavelength. This process allows us to obtain the percentage of light adsorption, γ, by the perovskite layer at each wavelength.

Then the optical power and the number of photons, $N_{ph,PV}$, absorbed by the perovskite layer within the optical pulse width can be calculated by

$$P_{ph,PV} = \gamma \frac{P_{in}}{E_\lambda} \quad (4.1\text{-a})$$

$$N_{ph,PV} = \gamma \frac{P_{in}T}{E_\lambda} \quad (4.1\text{-b})$$

where T is the laser pulse width (200 ms in our case), P_{in} is the input optical power, and E_λ is the energy of a single photon of wavelength λ.

4.3.5 Reflectivity Spectrum Characterization

To relate the photoresponse to any changes in material properties, which shed light on the origins of the photoresponse due to electronic transition or ionic migration, we also measured reflectivity spectrum of the device in areas subjective to voltage bias and light exposure using HP70950A Optical Spectrum Analyzer (OSA). We used the calibrated, single mode fiber coupled white light source from the instrument as the incident light and measured the reflected light by the device. The reflected light was coupled to the same optical fiber and entered the optical spectrum analyzer via a 90/10 fiber-optic coupler.

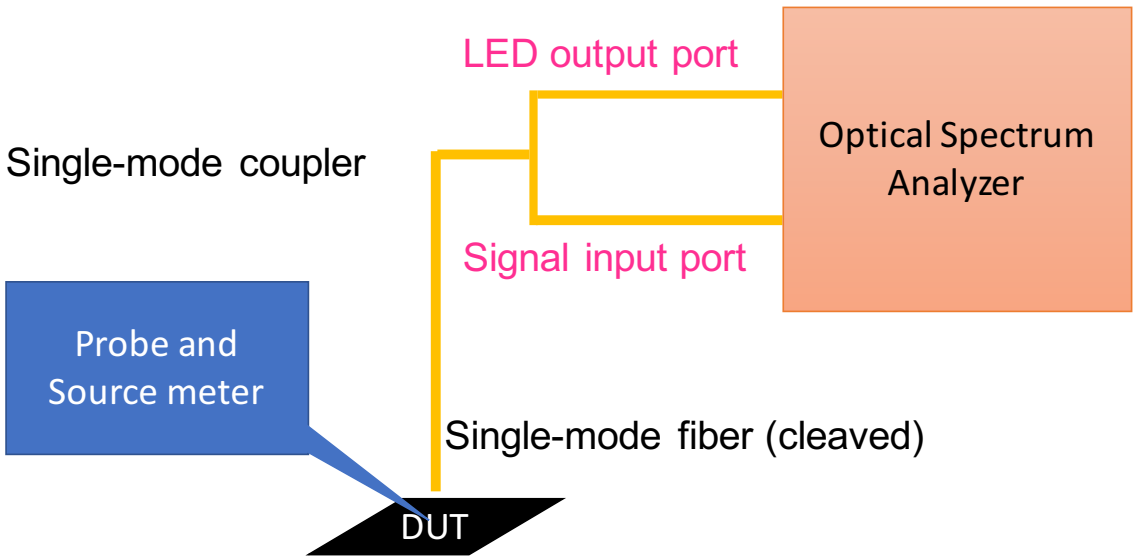

Figure 4.4. Block diagram for the setup of optical reflectivity measurement to confirm reversibility.

4.4. Two Regimes Photoresponses

4.4.1 High Frequency Response

Because of the small (7 μm diameter) active area of the device and the use of GSG high-speed probe, we can characterize the device over a broad frequency range. Figure 4.5 shows the device frequency response from 5Hz to 800 MHz at 4.5 μW sinusoidally modulated optical input absorbed (639 nm wavelength). Due to instrumental limits, we have measured the frequency response using two instruments: a lock-in amplifier from 5 Hz ~ 10 kHz and a vector analyzer and amplifier from 500 kHz to 800 MHz range. It was apparent that the photoresponsivity was nearly independent of frequency within the measurement errors and gave rise to the value of around 10^{-3} A/W under 4.5 μW.

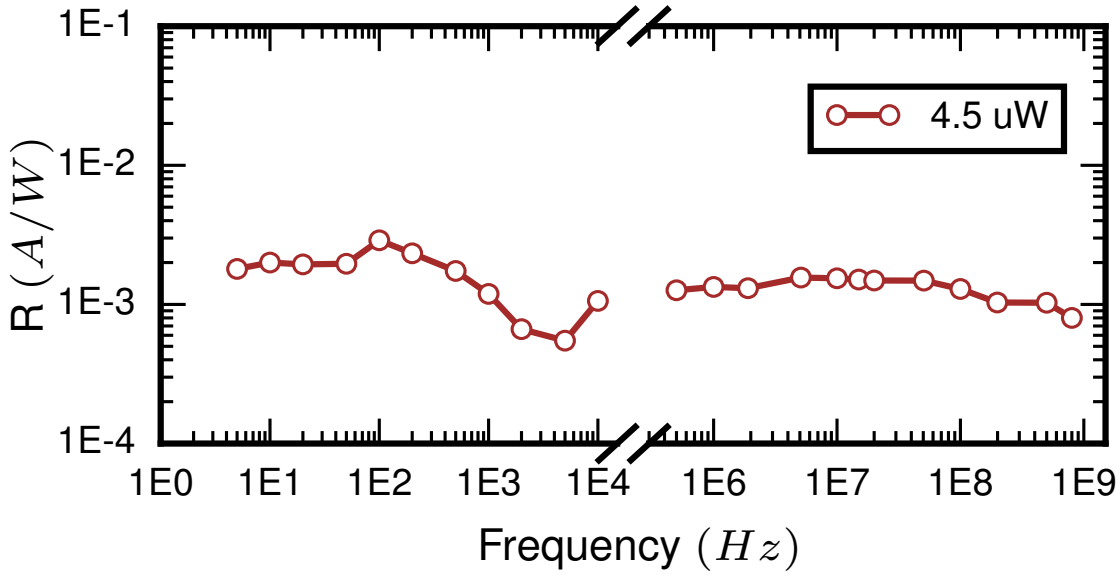

Figure 4.5. Frequency response from 5 Hz to 800 MHz with 4.5 μW 639 nm input

To characterize the optical power dependence of photoresponse, we also measured the power dependent responsivity from 18 pW to 5 μW under different frequencies (10 Hz, 0.5 MHz, 5 MHz, and 51 MHz). The log-log plot of responsivity is shown in Figure 4.6.a. The log-log slopes are all close to -0.38 for 0.5 MHz, 5 MHz, and 51 MHz in the power range from 50 nW to 5 μW. The log-log slope at 10 Hz also shows a similar slope of -0.41 for input power from 18 pW to 18 nW. Essentially these results show the power dependent responsivity of $R \propto P^{-\beta}$ with $\beta \sim 0.4$ from 10 Hz to 51 MHz. From literature we have found a similar relation was reported with $\beta \sim 0.5$. The value of β, which is typically between 0.4 and 0.5, is related to the defect states density in perovskite [17-18] and a detailed model between the defects and β will be presented separately.

Next we examined the responsivity under very low frequency (on the order of 0.1 Hz or quasi-persistent photoresponse). The slow response of photocurrent is obtained by taking the current difference before and after illumination by a single 200 ms optical pulse, as discussed in detail in the previous session on experimental setups and methods. The responsivity is obtained by dividing the photocurrent by the absorbed optical power by the perovskite layer. The log-log slope for slow-response responsivity under 639 nm is -0.89 between 14 aW and 6.9 fW (i.e. $R \propto P^{-\beta}$, $\beta \sim 0.9$), as shown in Figure 4.6.b. A similar correlation has also been reported in so-called DC measurements previously [15-16], showing that the internal responsivity as high as 10^7 A/W, and its value decreases rapidly with increased power. Note that the main difference between our measurement

and the conventional DC measurements is that the temporal response to a single optical pulse is directly measured, showing a very slow rise time of the device (in the order of 10 seconds).

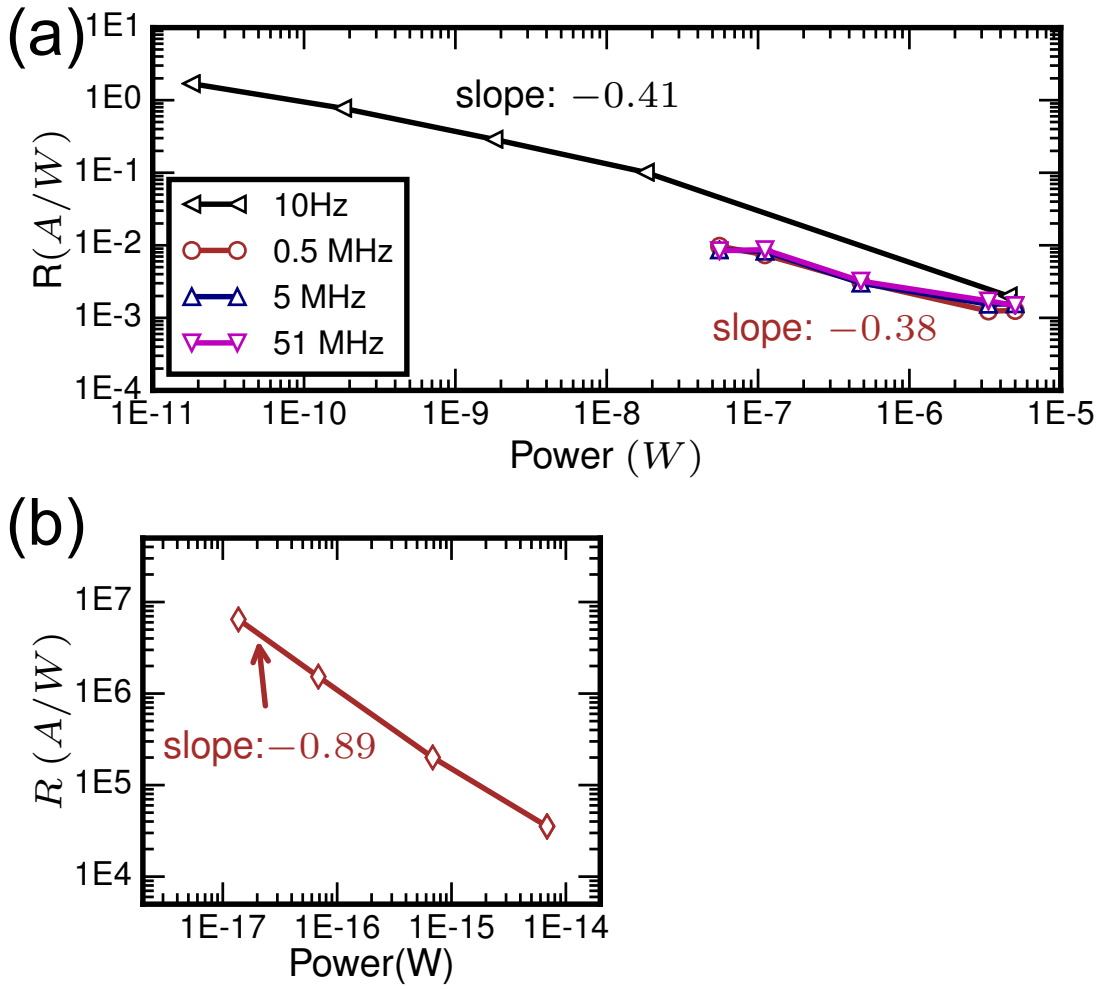

Figure 4.6. Power Dependent Response (639 nm) (a) Perovskite device power dependent photoresponse under 10Hz, 0.5MHz, 5MHz and 51 MHz. The slopes are all close to -0.4. (b) Power dependent slow (quasi-persistent) photoresponse.

We also observed the quasi-persistent photoresponsivity (i.e. the current does not return to the original dark current level without resetting the bias voltage (Figure 4.7). The good stability of the dark current allows us to precisely measure the persistent photocurrent as small as 30 pA, which is well above the sensitivity limit (10 fA) of the instrument. By comparing Figure 4.6.a and Figure 4.6.b, one interesting question arises: why the responsivity of a perovskite device shows two very different power dependence, one having a smaller slope of -0.4 and being frequency independent (at least from 5 Hz to 800 MHz) and another having a much steeper slope of -0.9 and having a very slow rise time (around 20 seconds) and being quasi-persistent. The most likely reason is that in perovskite, there are two distinct physical mechanisms that give rise to the photoresponse. One mechanism is similar to a standard photodiode where photon absorption generates electron-hole pairs travelling in the opposite directions under bias, and such response is largely frequency independent. On the other hand, the slow response is likely related to point defects and ion migration [19-22], which is slow but gives rise to persistent photocurrent until the device is reset by moving the ions back to their original distribution. During the present operation, both responses occur simultaneously, and which effects show up depend on how we measure the response.

What is most striking, however, is that we have found the slow (quasi-persistent) response can be further divided into two regimes, one showing the aforementioned relation (i.e. $R \propto P^{-\beta}$, $\beta \sim 0.9$) and another showing no power dependence (i.e. $R \propto P^{-\beta}$, $\beta \sim 0$)! Due to the extremely low power level that distinguishes the two

drastically different power dependent relations, in the following we use the number of photons absorbed by the device to discuss the two regimes.

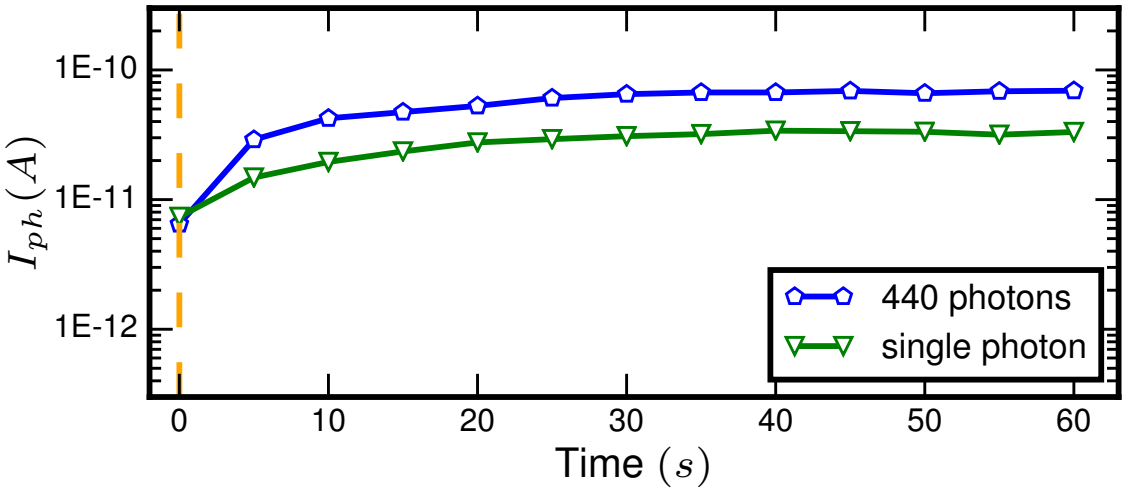

Figure 4.7. Slow (quasi-persistent) response of the device to a single optical pulse containing a different number of photons.

4.4.2 Single Photon Sensitive Slow-Response

In the slow (quasi-persistent) photoresponse regimes, tests were performed at both 518 nm and 635 nm with a similar range of power. The turning point for the power dependence of responsivity occurs at around 10 aW where the responsivity reaches its maximum value of $1.7x10^7 A/W$. At $\lambda = 518\,nm$, a single photon of an energy of 2.39 eV (0.38 aJoule) corresponds to a power level of 1.9 aW in a 200ms optical pulse. The flat regime in Figure 4.8 corresponds to the response to 1 to 10 photons of the device. The full range of power in Figure 4.8 corresponds to 1 to 400 photons absorbed by the perovskite layer. When more than 10 photons are absorbed by the perovskite layer, the responsivity displays the relation of $R \propto P^{-\beta}$, $\beta \sim 0.9$.

A constant responsivity means that the output photocurrent of the perovskite detector is linearly proportional to the number of photons absorbed by the perovskite layer. Figure 4.9 shows the results of 40 measurements with an average of 0.98 photons absorbed by the perovskite layer. It shows that by absorption of a single photon, the current is increased by around 30 pA on average. The quasi-persistent change in the material conductivity, revealed as persistent photocurrent, is most likely caused by redistributions of the ion and charged vacancy within the perovskite layer, which subsequently changes band bending and carrier injection efficiency at the ITO/perovskite junction.

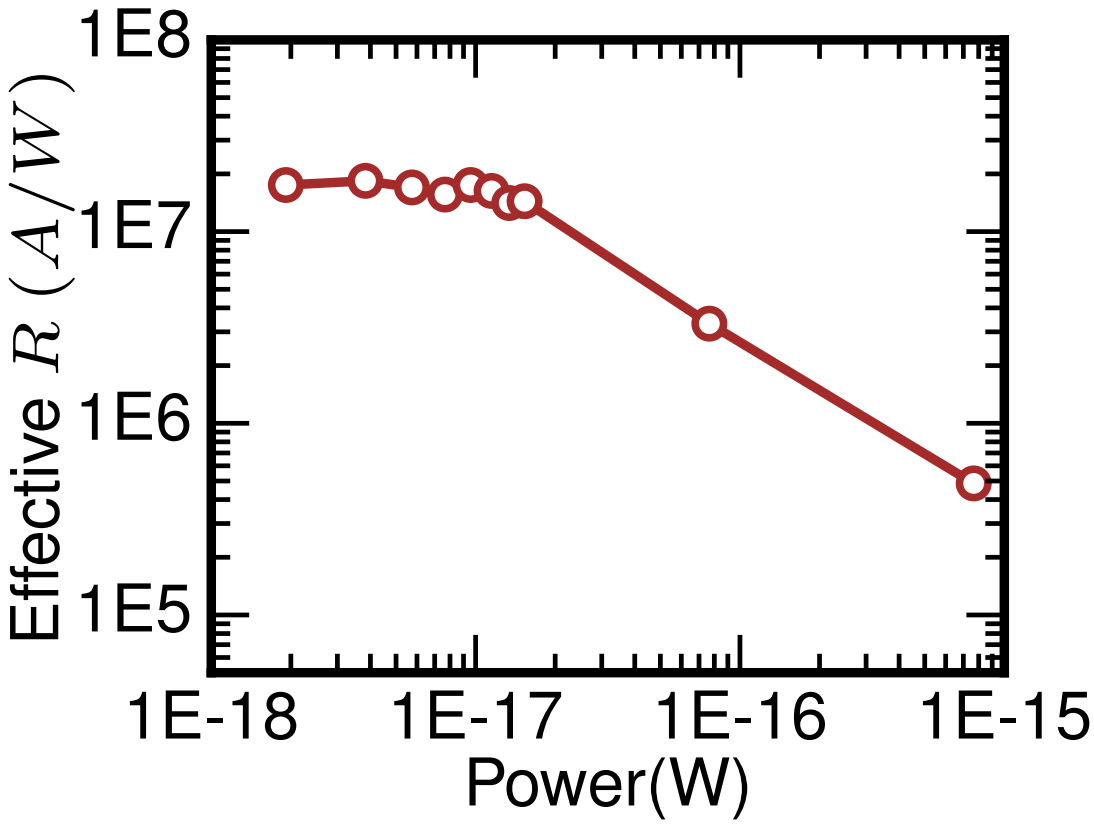

Figure 4.8 Average power-dependent quasi-persistent photoresponse (518 nm).

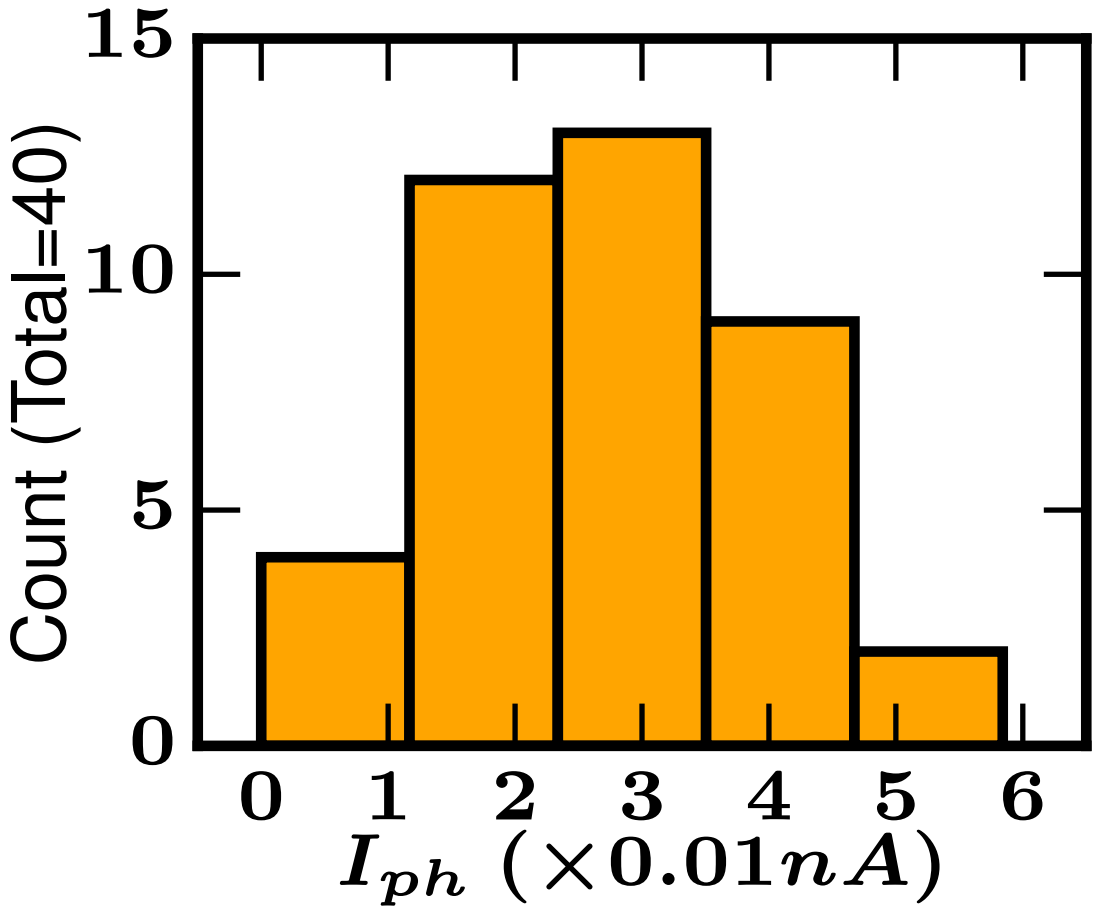

Figure 4.9. Statistical distribution of photocurrent with absorption of a single 518 nm wavelength photon. (Average Photon number: 0.98)

Figure 4.10 shows the bias-dependent photoresponse with eight 518 nm wavelength photons absorbed. Below the bias of 0.620 V (corresponding to an average electric field of 1.55×10^4 V/cm in the 400 nm perovskite layer), the photoresponse drops rapidly. Interestingly the threshold filed for this internal amplification process is an order of magnitude lower than the threshold field for electron impact ionization in most condensed matters

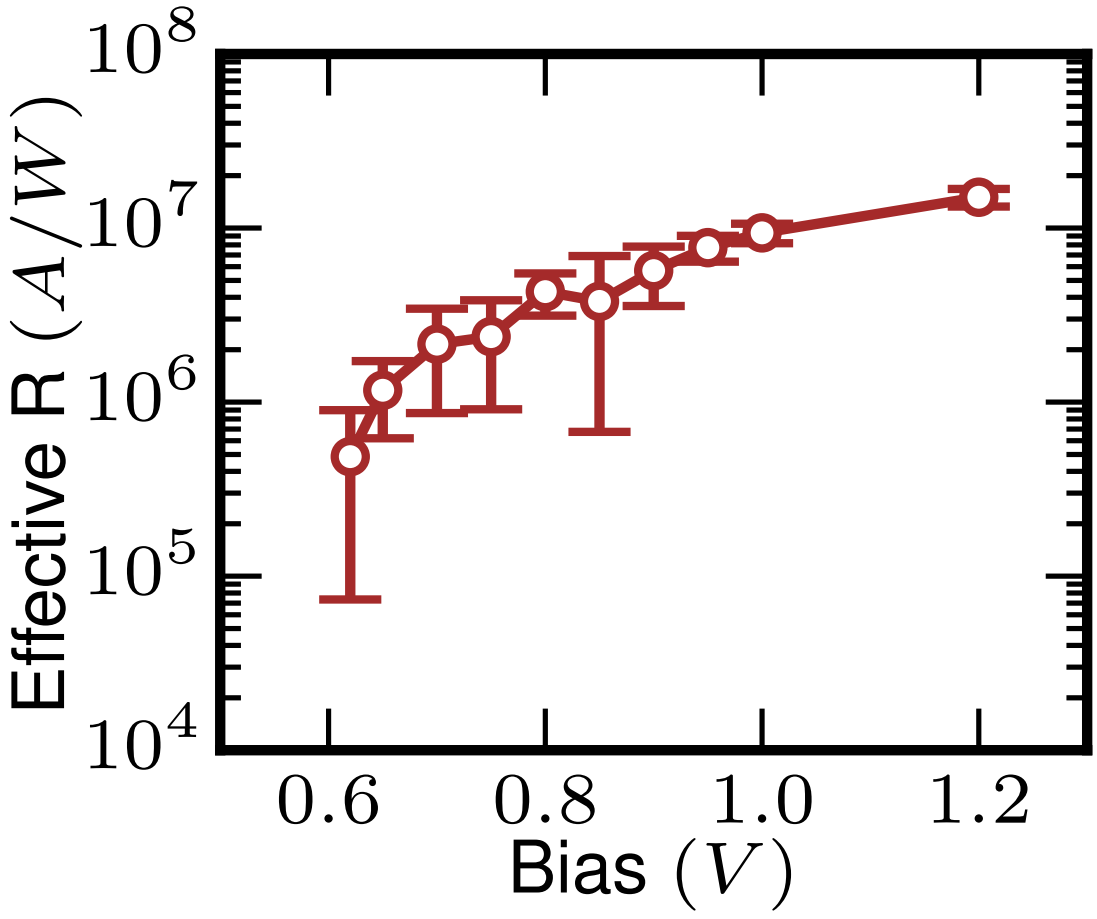

Figure 4.10. Bias-dependent quasi-persistent photoresponse to 8 photons of 518 nm wavelength.

4.5 Reversibility for Quasi-Persistent Photoresponse and Proposed Mechanism.

For another supporting evidence of macroscopic property change under optical excitation and external bias, we measured the reflectivity spectrum of the device before and after optical illumination under bias and after resetting the bias to 0 V. The observed reflective spectrum change indicates the change of composition distribution within the device due to this reversible process [23-24]. Under white light illumination, the reflectivity peak of the device under bias shifted from 645 nm to around 630 nm, as shown in Figure 4.11.a. After the light source and bias were turned off, the reflective peak shifted back after about 2 minutes, indicating that the perovskite layer returned to the original state by ion diffusion [25]. The observation with the quasi-persistent photoresponse behavior leads to the proposed potential band diagram change due to charged ion and vacancies accumulation near the electrodes, as illustrated in Figure 4.11.b.

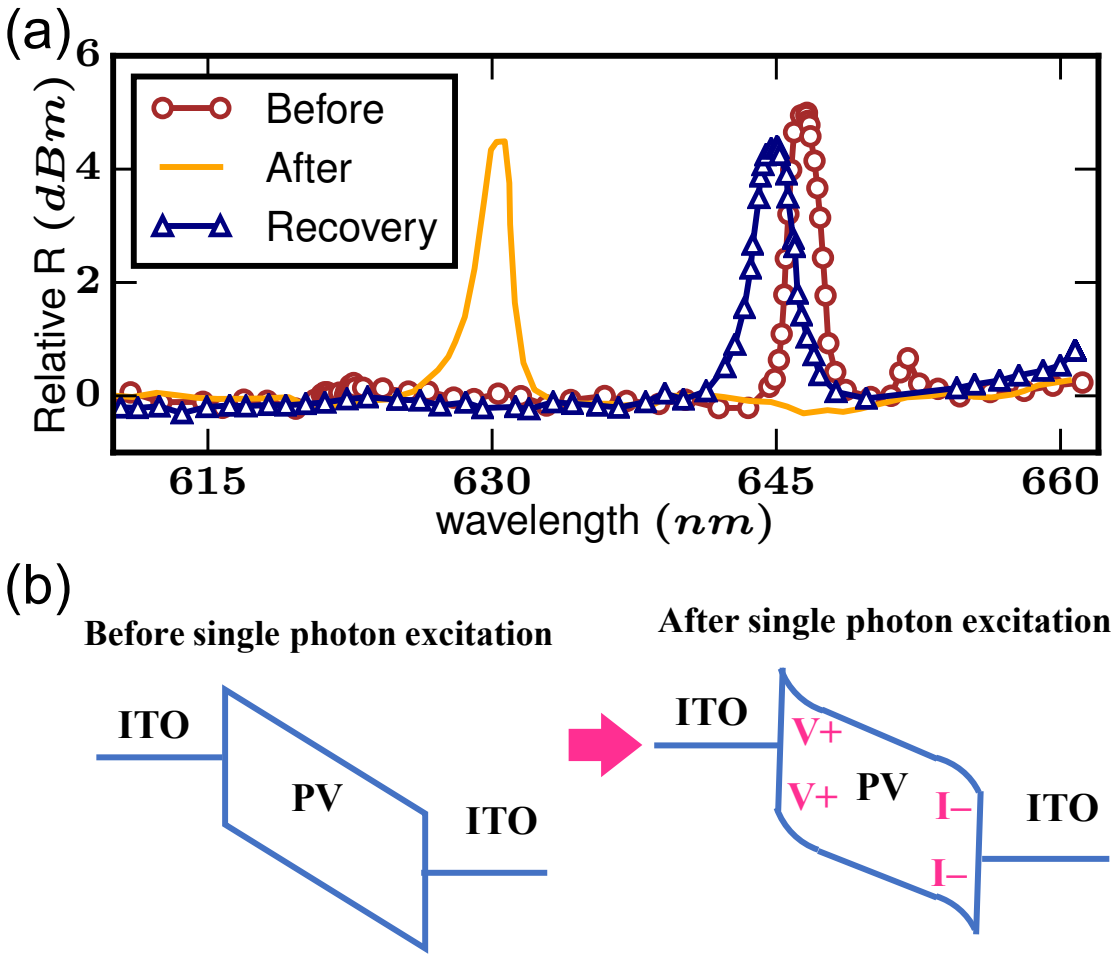

Figure 4.11. Reversibility of the internal amplification process (a) Relative Reflective Spectrum. Brown circle line is reflectivity upon the device area before illumination; Orange star line is reflectivity after illumination with applied bias; Navy triangle line is reflectivity two minutes after bias was turned off. (b) Band-bending under bias due to accumulation of changed ions after photons absorption.

4.6 Discussion and Applications

In a 7 μm diameter perovskite photodetector, we investigated the frequency and optical power dependent responsivity. We observed that the device showed two different power dependent responsivities, one being similar to conventional photodetectors and the other being quasi-persistent and sensitive to very low optical power up to a single photon. By careful measurements of photoresponse of perovskite device down to the single photon level, we discovered that $MAPbI_3$ perovskite can change its macroscopic electric properties by absorbing the energy of a single photon (about 0.2 aJoule). This phenomenon cannot be explained without an internal amplification mechanism that can cause collective motion of a massive number of iodides by absorption of only a few photons.

The main contribution of this chapter is to report the first observation that macroscopic electric and optoelectronic properties of perovskite thin films can be altered or programmed by a few or even a single photon carrying extremely low (aJoule) energy. The detailed physical mechanism that gives the device its extremely high sensitivity and persistent response requires further experimental and theoretical investigations. One particular promising application utilizing this internal amplification process is analog memory device for neuromorphic computing [26-27]. The low-energy operation triggered by even single-photon irradiation provides large benefits in the computing system. The cascadic behavior allows us to develop new types of multistate memory with forming-free property, and new logic circuit architecture. Since the slow response can come from collective ionic motions, some electronic device applications such as high-speed

transistor may be limited, but many new device applications including energy harvesting, high capacity memory, and optical switches are expected. For example, the development of photo/electrochromic device with low power operation and high response speed is expected. The simple device structure and solution process are ideal for low-cost, highly integrated practical applications and mass production. Although there are several technological challenges including stability issues of this material group, novel cascadic ion migration behavior as well as the other high-speed operation regime gives us ample opportunities to create new device applications based on hybrid perovskites. We anticipate this part of work will create new avenues for research and application of perovskite device and material.

Portions of Chapter 4 have been published in the following publication: **Zihan Xu**†, Yugang Yu†, Shaurya Arya, Iftikhar Ahmad Niaz, Yimu Chen, Yusheng Lei, Mohammad Abu Raihan Miah, Jiayun Zhou, Alex Ce Zhang, Lujiang Yan, Sheng Xu, Kenji Nomura and Yu-Hwa Lo, "Frequency and Power Dependent Photoresponse of Perovskite Photodetector Down to Single Photon Level", *Nano Letters*, (2020). († These authors contributed equally.) The dissertation author was the co-first author/primary investigator and author of these papers.

Reference:

[1] Zhao, Yixin, and Kai Zhu. "Organic–inorganic hybrid lead halide perovskites for optoelectronic and electronic applications." *Chemical Society Reviews* 45, no. 3 (2016): 655-689.

[2] Jeon, Nam Joong, Jun Hong Noh, Young Chan Kim, Woon Seok Yang, Seungchan Ryu, and Sang Il Seok. "Solvent engineering for high-performance inorganic–organic hybrid perovskite solar cells." *Nature materials* 13, no. 9 (2014): 897.

[3] Lei, Yusheng, Yimu Chen, Yue Gu, Chunfeng Wang, Zhenlong Huang, Haoliang Qian, Jiuyuan Nie, J., Hollett, G., Choi, W., Yu, Y. and Kim, N., "Controlled Homoepitaxial Growth of Hybrid Perovskites." *Advanced Materials* 30, no. 20 (2018): 1705992.

[4] Lin, Kebin, Jun Xing, Li Na Quan, F. Pelayo García de Arquer, Xiwen Gong, Jianxun Lu, Liqiang Xie, Zhao, W., Zhang, D., Yan, C. and Li, W. "Perovskite light-emitting diodes with external quantum efficiency exceeding 20 per cent." *Nature* 562, no. 7726 (2018): 245.

[5] Saidaminov, Makhsud I., Valerio Adinolfi, Riccardo Comin, Ahmed L. Abdelhady, Wei Peng, Ibrahim Dursun, Mingjian Yuan, Sjoerd Hoogland, Edward H. Sargent, and Osman M. Bakr. "Planar-integrated single-crystalline perovskite photodetectors." *Nature communications* 6 (2015): 8724.

[6] Saidaminov, Makhsud I., Md Azimul Haque, Maxime Savoie, Ahmed L. Abdelhady, Namchul Cho, Ibrahim Dursun, Ulrich Buttner, Erkki Alarousu, Tom Wu, and Osman M. Bakr. "Perovskite photodetectors operating in both narrowband and broadband regimes." *Advanced Materials* 28, no. 37 (2016): 8144-8149.

[7] Fang, Yanjun, and Jinsong Huang. "Resolving weak light of sub-picowatt per square centimeter by hybrid perovskite photodetectors enabled by noise reduction." *Advanced Materials* 27, no. 17 (2015): 2804-2810.

[8] Hu, Xin, Xiaodong Zhang, Lin Liang, Jian Bao, Shuang Li, Wenlong Yang, and Yi Xie. "High-performance flexible broadband photodetector based on organolead halide perovskite." *Advanced Functional Materials* 24, no. 46 (2014): 7373-7380.

[9] Ji, Li, Hsien-Yi Hsu, Jack C. Lee, Allen J. Bard, and Edward T. Yu. "High-performance photodetectors based on solution-processed epitaxial grown hybrid halide perovskites." *Nano letters* 18, no. 2 (2018): 994-1000.

[10] Wu, Jiang, Junyan Chen, Yifei Zhang, Zhaojian Xu, Lichen Zhao, Tanghao Liu, Deying Luo, D., Yang, W., Chen, K., Hu, Q. and Ye, F., "Pinhole-free hybrid perovskite film with arbitrarily-shaped micro-patterns for functional optoelectronic devices." *Nano letters* 17, no. 6 (2017): 3563-3569.

[11] Liu, Yang, Fushan Li, Chandrasekar Perumal Veeramalai, Wei Chen, Tailiang Guo, Chaoxing Wu, and Tae Whan Kim. "Inkjet-printed photodetector arrays based on hybrid

perovskite CH3NH3PbI3 microwires." *ACS applied materials & interfaces* 9, no. 13 (2017): 11662-11668.

[12] Dou, Letian, Yang Micheal Yang, Jingbi You, Ziruo Hong, Wei-Hsuan Chang, Gang Li, and Yang Yang. "Solution-processed hybrid perovskite photodetectors with high detectivity." *Nature communications* 5 (2014): 5404.

[13] Shen, Liang, Yanjun Fang, Dong Wang, Yang Bai, Yehao Deng, Mengmeng Wang, Yongfeng Lu, and Jinsong Huang. "A Self-Powered, Sub-nanosecond-Response Solution-Processed Hybrid Perovskite Photodetector for Time-Resolved Photoluminescence-Lifetime Detection." *Advanced Materials* 28, no. 48 (2016): 10794-10800.

[14] Bao, Chunxiong, Zhaolai Chen, Yanjun Fang, Haotong Wei, Yehao Deng, Xun Xiao, Lingliang Li, and Jinsong Huang. "Low-Noise and Large-Linear-Dynamic-Range Photodetectors Based on Hybrid-Perovskite Thin-Single-Crystals." *Advanced Materials* 29, no. 39 (2017): 1703209.

[15] Ji, Chengmin, Peng Wang, Zhenyue Wu, Zhihua Sun, Lina Li, Jing Zhang, Weida Hu, Maochun Hong, and Junhua Luo. "Inch-Size Single Crystal of a Lead-Free Organic–Inorganic Hybrid Perovskite for High-Performance Photodetector." *Advanced Functional Materials* 28, no. 14 (2018): 1705467.

[16] Guo, Yunlong, Chao Liu, Hideyuki Tanaka, and Eiichi Nakamura. "Air-stable and solution-processable perovskite photodetectors for solar-blind UV and visible light." *The journal of physical chemistry letters* 6, no. 3 (2015): 535-539.

[17] Lian, Zhipeng, Qingfeng Yan, Qianrui Lv, Ying Wang, Lili Liu, Lijing Zhang, Shilie Pan, Qiang Li, Liduo Wang, and Jia-Lin Sun. "High-performance planar-type photodetector on (100) facet of MAPbI 3 single crystal." *Scientific reports* 5 (2015): 16563.

[18] Chen, Shan, Changjiu Teng, Miao Zhang, Yingru Li, Dan Xie, and Gaoquan Shi. "A Flexible UV–Vis–NIR Photodetector based on a Perovskite/Conjugated-Polymer Composite." *Advanced Materials* 28, no. 28 (2016): 5969-5974.

[19] Minns, J. L., Paweł Zajdel, D. Chernyshov, W. Van Beek, and M. A. Green. "Structure and interstitial iodide migration in hybrid perovskite methylammonium lead iodide." *Nature communications* 8, no. 1 (2017): 1-5.

[20] Yin, Wan-Jian, Tingting Shi, and Yanfa Yan. "Unusual defect physics in CH3NH3PbI3 perovskite solar cell absorber." *Applied Physics Letters* 104, no. 6 (2014): 063903.

[21] Kim, Jongseob, Sung-Hoon Lee, Jung Hoon Lee, and Ki-Ha Hong. "The role of intrinsic defects in methylammonium lead iodide perovskite." *The journal of physical chemistry letters* 5, no. 8 (2014): 1312-1317.

[22] Peng, Wei, Clara Aranda, Osman M. Bakr, Germà Garcia-Belmonte, Juan Bisquert, and Antonio Guerrero. "Quantification of ionic diffusion in lead halide perovskite single crystals." *ACS Energy Letters* 3, no. 7 (2018): 1477-1481.

[23] Jeangros, Quentin, Martial Duchamp, Jérémie Werner, Maximilian Kruth, Rafal E. Dunin-Borkowski, Bjoern Niesen, Christophe Ballif, and Aïcha Hessler-Wyser. "In situ TEM analysis of organic–inorganic metal-halide perovskite solar cells under electrical bias." *Nano letters* 16, no. 11 (2016): 7013-7018.

[24] Price, Michael B., Justinas Butkus, Tom C. Jellicoe, Aditya Sadhanala, Anouk Briane, Jonathan E. Halpert, Katharina Broch, Justin M. Hodgkiss, Richard H. Friend, and Felix Deschler. "Hot-carrier cooling and photoinduced refractive index changes in organic–inorganic lead halide perovskites." *Nature communications* 6 (2015): 8420.

[25] Dong, Qingfeng, Yanjun Fang, Yuchuan Shao, Padhraic Mulligan, Jie Qiu, Lei Cao, and Jinsong Huang. "Electron-hole diffusion lengths> 175 μm in solution-grown CH3NH3PbI3 single crystals." *Science* 347, no. 6225 (2015): 967-970.

[26] Zou, Chen, Jiajiu Zheng, Cheng Chang, Arka Majumdar, and Lih Y. Lin. "Nonvolatile Rewritable Photomemory Arrays Based on Reversible Phase-Change Perovskite for Optical Information Storage." *Advanced Optical Materials* (2019): 1900558.

[27] Wang, Yan, Ziyu Lv, Jinrui Chen, Zhanpeng Wang, Ye Zhou, Li Zhou, Xiaoli Chen, and Su-Ting Han. "Photonic synapses based on inorganic perovskite quantum dots for neuromorphic computing." *Advanced Materials* 30, no. 38 (2018): 1802883.

Chapter 5 Ionic Impact Ionization and Density Functional Theory Toy Model

5.1 Proposed Ionic Impact Ionization in Perovskite

From the quasi-persistent photoresponse results discussed in chapter 4, we learnt that there has to be an internal amplification mechanism so that the perovskite photodetector can respond to single photon level input. We previously proposed the perovskite conductivity changes result from the accumulation of charged ions and vacancies which lead to band bending, due to single photon absorption under bias, as shown in Figure 4.11.b.

Here we propose a reversible amplification mechanism, ionic impact ionization (I3), to explain observations of macroscopic property changes by absorption of a single photon, as shown in Figure 5.1. This process triggered by an absorbed photon can be represented by equation (5.1), where the process in equation (5.1.c) (i.e. I3 process) is cascaded and the rate grows exponentially,

$$V_I^+/I_i^- \xrightarrow{h\nu} V_I^+/I_i^- + e^-/h^+ \rightarrow V_I^+/I_i^- + m\hbar\Omega \quad (5.1.a)$$

$$V_I^+/I_i^- + m\hbar\Omega \rightarrow V_I^+ + I_i^- \quad (5.1.b)$$

$$I_i^- + V_I^+/I_i^- \xrightarrow{E-field} V_I^+ + 2\,I_i^- \quad (5.1.c)$$

By absorbing an input photon of energy $h\nu$, an electron-hole pair is generated across the bandgap (or a midgap state for photon energy lower than the bandgap) . The electron-hole pair (e^-/h^+) recombines non-radiatively, producing multiple phonons, $m\hbar\Omega$, with sufficient vibrational energy to ionize the V^+/ I^- Frenkel pair, as shown in equation (5.1.b) [1-3], to become mobile V^+ and I^-. The applied electric field splits the V^+ and I^- apart. V^+ has much higher mobility (~$1x10^{-6}$ cm^2/Vs) [4] than I^- (~$5x10^{-8}$

cm^2/Vs) [5] and reaches the cathode while I^- still travels towards the anode. The proposed I3 process is described in equation (5.1.c). The Coulomb interaction between the travelling I^- and the V_I^+/I_i^- Frenkel pair can break the Frenkel pair into mobile V_I^+ and I_i^-. As a result, the number of mobile I_i^- increases exponentially in an avalanche-like process as the I_i^-s move towards the anode.

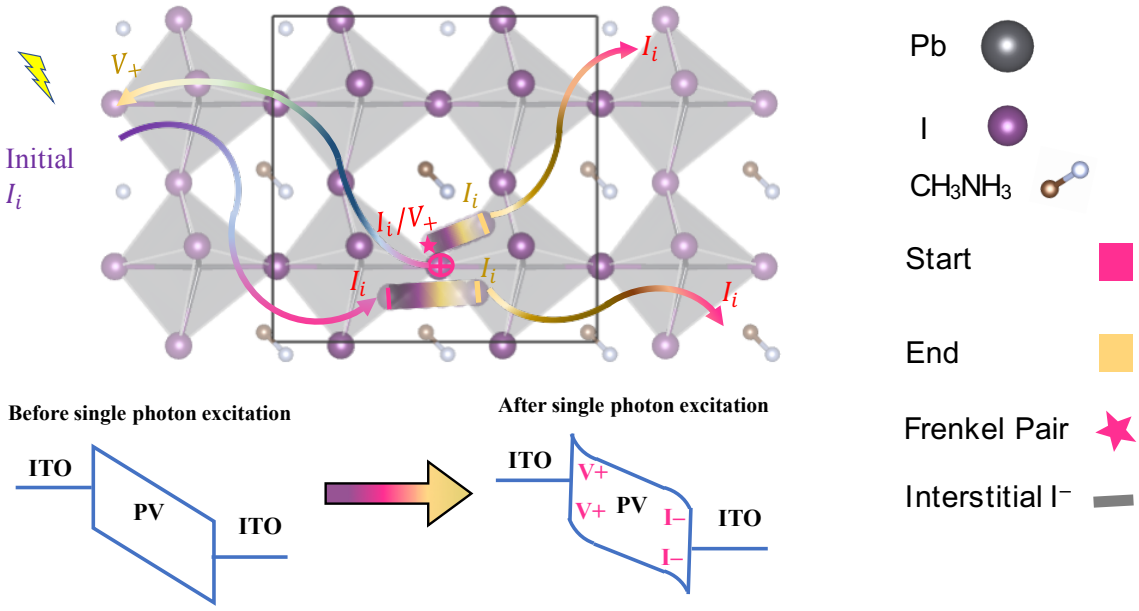

Figure 5.1. Ionic impact ionization (I3) process in equation (5.1.). Photo-induced initial I^- is generated from equation (5.1.a) and equation (5.1.b). When this initial I^- migrates and meets a Frenkel pair, equation (5.1.c) starts. Pink markers indicate the starting states and yellow markers indicate the finishing state of equation (5.1.c). The I^- generated from equation (5.1.c) will break another V_I^+/I^- Frenkel pair to produce another I^- and V^+, the I3 process, which will change the band diagram eventually due to the accumulation of V_I^+ and I^- at the cathode and anode.

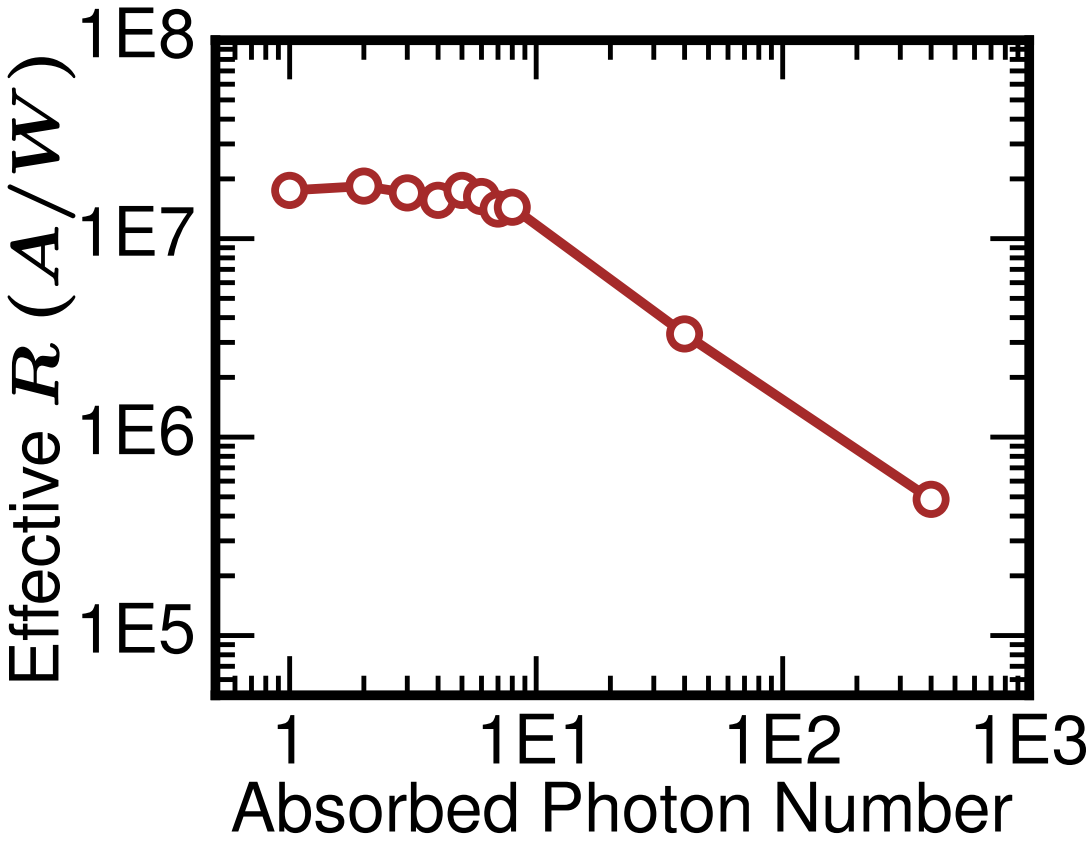

Figure 5.2. Effective quasi-persistent photoresponsivity vs. Absorbed Photon Number for 518 nm input. The photon number was counted within a 200 ms time window.

The data in Figure 5.2 show that the photoresponse of a 7 μm diameter device saturates by absorption of around 8 photons, suggesting that it takes only 8 I_i^- from photo-ionized Frenkel pairs to break apart all available V_I^+/I_i^- Frenkel pairs within the device.

Eventually all mobile iodides and V_I^+ are accumulated at perovskite/ITO interfaces near the anode and cathode, respectively, producing a macroscopic dipole inside the perovskite film and band bending. Such band bending lowers the effective Schottky barrier between ITO and perovskite [6-7], resulting in an increase in the

thermionic emission current under constant bias (tunneling current is negligible in this case due to low bias voltage). The increased current is represented as photoresponse or photocurrent of the device. Due to the highly efficient I3 process elucidated before, even the energy of a single photon can produce a measurable photoresponse. Or alternatively, the electric property of a perovskite device can be "switched" or "controlled" by a single photon.

The electrical conductivity change can be modeled by distribution of V^+'s and iodides within perovskite. By moving a given amount of iodides towards the anode and the same amount of V^+ to the cathode to keep the total charge within perovskite neutral, we obtain the band bending of perovskite, and the current under bias can be calculated from the thermionic emission model in equation (5.2)

$$J_T = AT^2 \exp\left(-\frac{q\varphi_B}{kT}\right)\left(\exp\left(\frac{qV}{kT}\right) - 1\right) \tag{5.2}$$

where A = Richardson coefficient, T = 300 K, φ_B = Schottky barrier height, V = applied bias, q = electron charge, and k = Boltzmann Constant. Taking the ratio between the total current (photocurrent plus dark current) and the dark current and using equation (5.2), we can obtain the change in Schottky barrier height $\Delta\varphi_B$, in equation (5.3),

$$\frac{I_{ph}+I_d}{I_d} = \exp\left[-\frac{q}{kT}\Delta\varphi_B\right] \tag{5.3}$$

Using the relation

$$\Delta\varphi_B = \varphi_B - \varphi_{Bo} = -\sqrt{qE/4\pi\varepsilon_0\varepsilon_r} \tag{5.4}$$

where E = electric field, ε_0 = permittivity of free space, ε_r= dielectric constant of perovskite), we can find the relation between the electric field at the perovskite/ITO interface and the measured currents, as shown in equation (5.5),

$$E = 4\pi\varepsilon_0\varepsilon_r[\ln(\frac{I_{ph}+I_d}{I_d})\frac{kT}{q^{3/2}}]^2 \quad (5.5)$$

According to the model for I3 process, the total number of impact ionization cycles is given by

$$C_{I3} = \log2(N_{I3}/N_{Ph}) \quad (5.6)$$

where N_{Ph} is the absorbed number of photons, which is assumed to be equal to the number of initial mobile iodides. The mean free path for the I3 process (IMFP) can be estimated to be IMFP= d/C_{I3}, where "d" is the thickness of perovskite film, being 400 nm in our case. Figure 5.3 shows the bias dependence of ionic impact ionization IMFP over a 400 nm perovskite film. Similar to electronic impact ionization, the externally applied bias needs to reach a threshold level to provide sufficient energy to the particle to create impact ionization. For ionic impact ionization, the threshold bias for I3 process is around 0.620 V, which corresponds to an IMFP of 20 nm and an energy barrier of 50 meV. In order to further verify our proposed mechanism, we used a Density Functional Theory (DFT) toy model to check the energy barrier for the I3 process in the perovskite device. We'll discuss the DFT toy model and calculation results in details in Chapter 5.2.

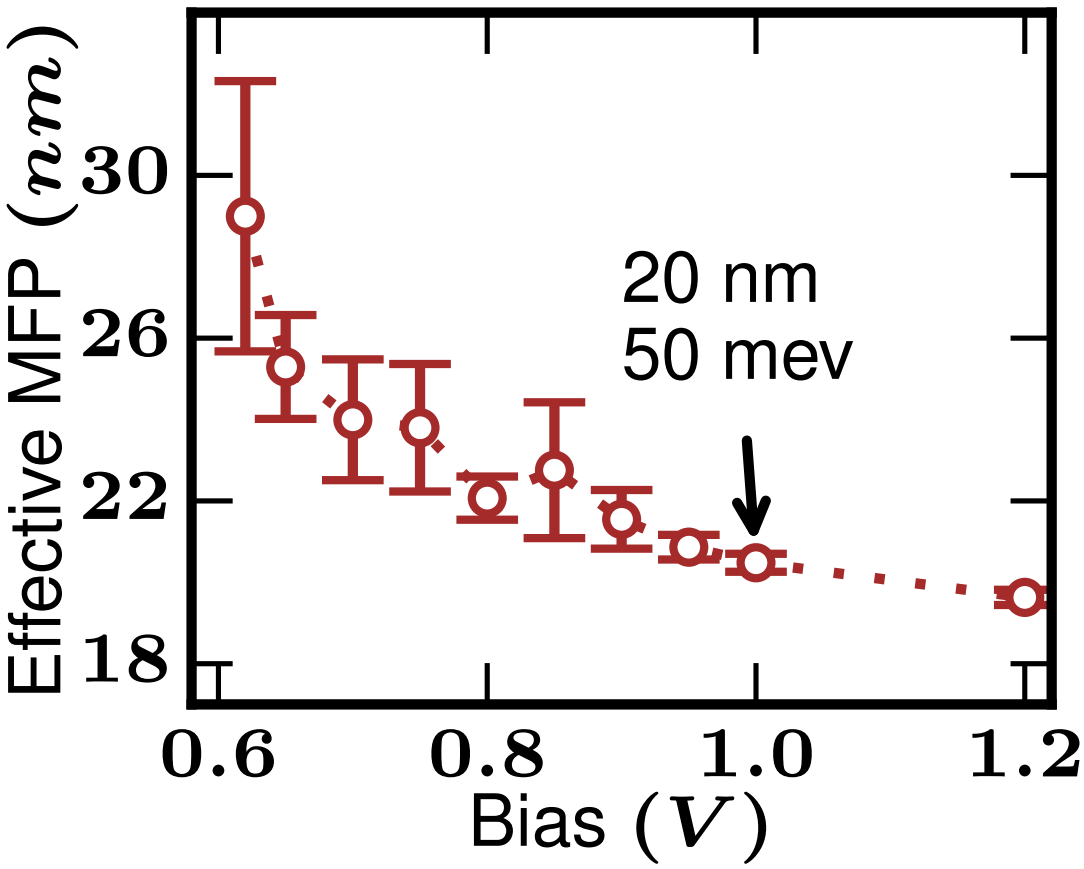

Figure 5.3. Bias dependent effective mean free path (MFP). For 1V bias, the effective MFP is 20 nm, corresponding to an energy barrier of 50 meV.

5.2 Density Functional Theory Toy Model for Ionic Impact Ionization

5.2.1 Computational Details

We used Quantum Espresso to perform the DFT calculations to verify the Ionic Impact Ionization (I3) process in perovskite. Density functional theory (DFT) simulations have been implemented in the PWSCF program of the Quantum Espresso Package [8]. Projector-augment wave (PAW) method with Perdew-Burke-Ernzerhof (PBE) exchange-correlation functional was used [9]. The energy cutoffs were set to 37 Ry (~500 eV) for the wave functions and 200 Ry for the kinetic energy. The energies were converged to 0.0001eV and the forces were converged to 0.05 eV/Å. All the energies were calculated from an initial gamma point relaxation, followed by a static calculation with 2 x 2 x 2 k-points. From the initial cubic unit cell [10], a lattice constant optimization was carried out and a lattice constant of 6.32 Å was obtained, which is close to X-ray diffraction result [11] of 6.31 Å and neutron diffraction result [12] of 6.32 Å. Consequently, a 2 x 2 x 2 supercell of 96 atoms bulk was generated and further optimized with fixed volume. In the simulation of one cycle of the I3 process, the starting state was adopted from the relaxation of the initial bulk structure with one interstitial iodine ion defect and the finishing state was adopted from the relaxation of the initial bulk structure with two interstitial iodine ions and one positive charged vacancy. The background charge for both states in a cycle of the I3 process was set to -1. The relaxed perfect cubic 2 x 2 x 2 supercell is shown in Figure 5.4.

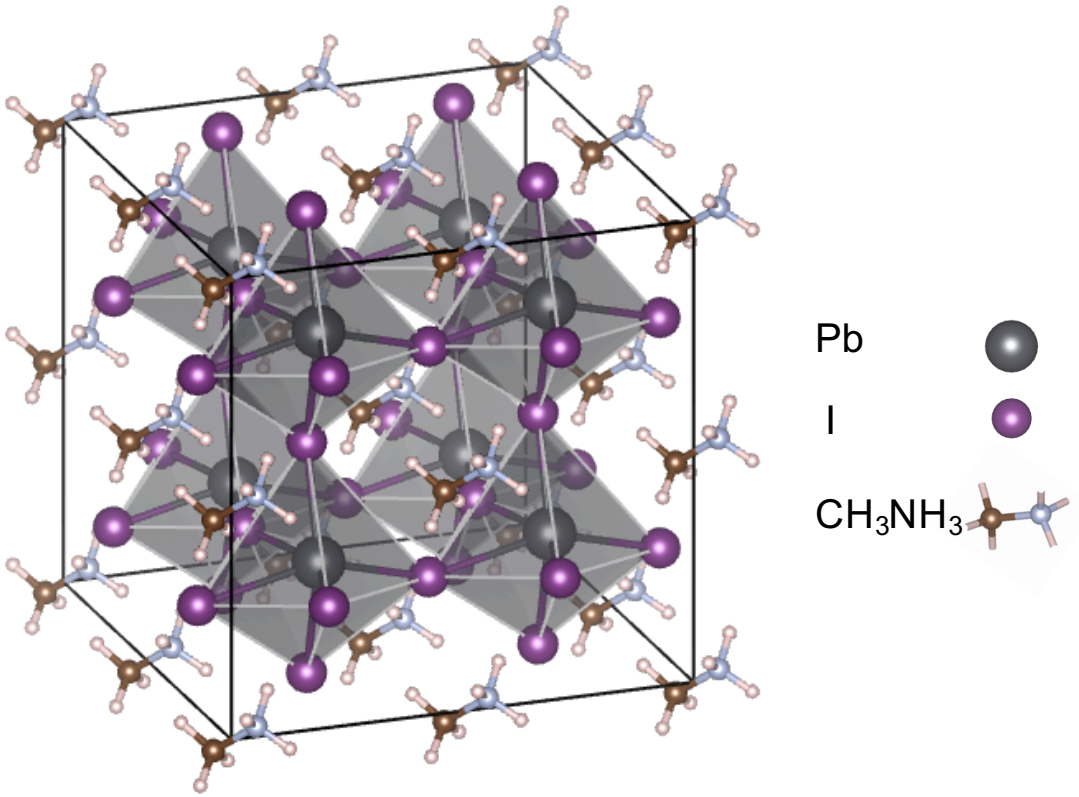

Figure 5.4. Relaxed perfect cubic supercell (2x2x2) for perovskite.

5.2.2 DFT Toy Model Results

In the 2 x 2 x 2 cubic cell (96 atoms), the initial state contains one negatively charged interstitial iodide (right crossing) and one V_I^+/I^- Frenkel pair (left crossing), shown in Figure 5.5. The final state after one cycle of I3 process is represented by two negatively charged interstitial iodide point defects with one positive charged vacancy, as shown in Figure 5.6.

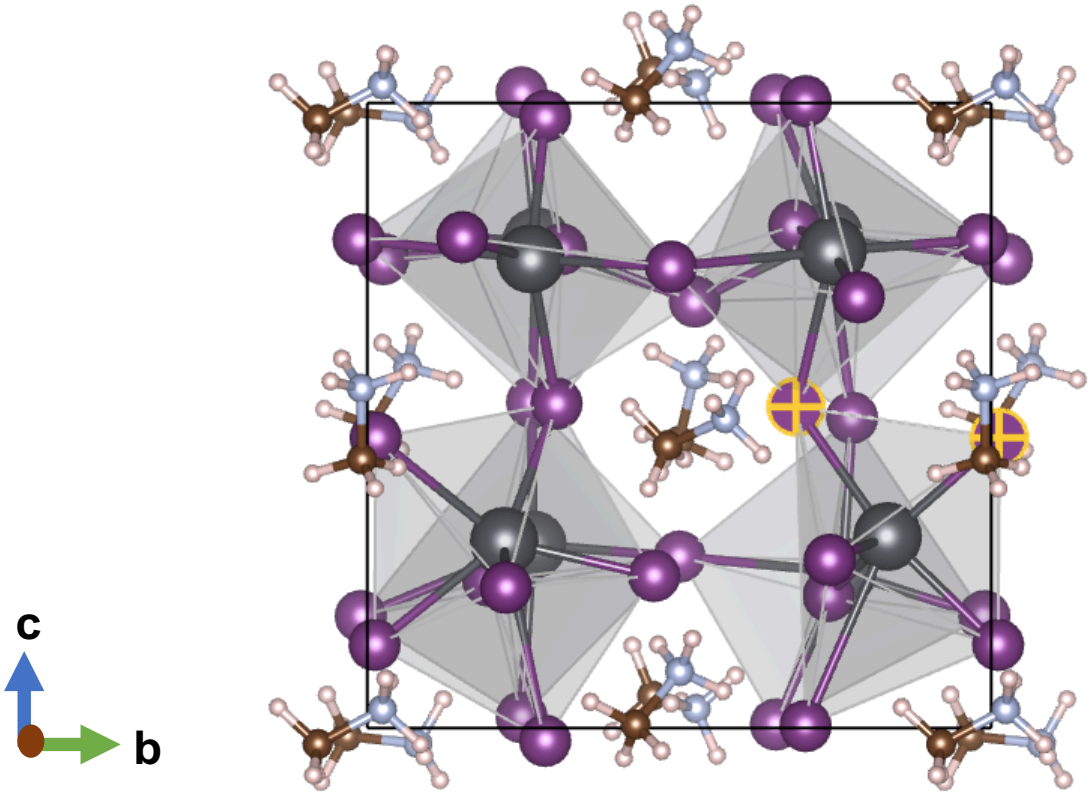

Figure 5.5. Starting State in one cycle of I3 process: 1 V_I^+/I^- Frenkel pair of defects (left crossing) and 1 interstitial I^- (right crossing). The front view of a cell with 97 atoms is shown.

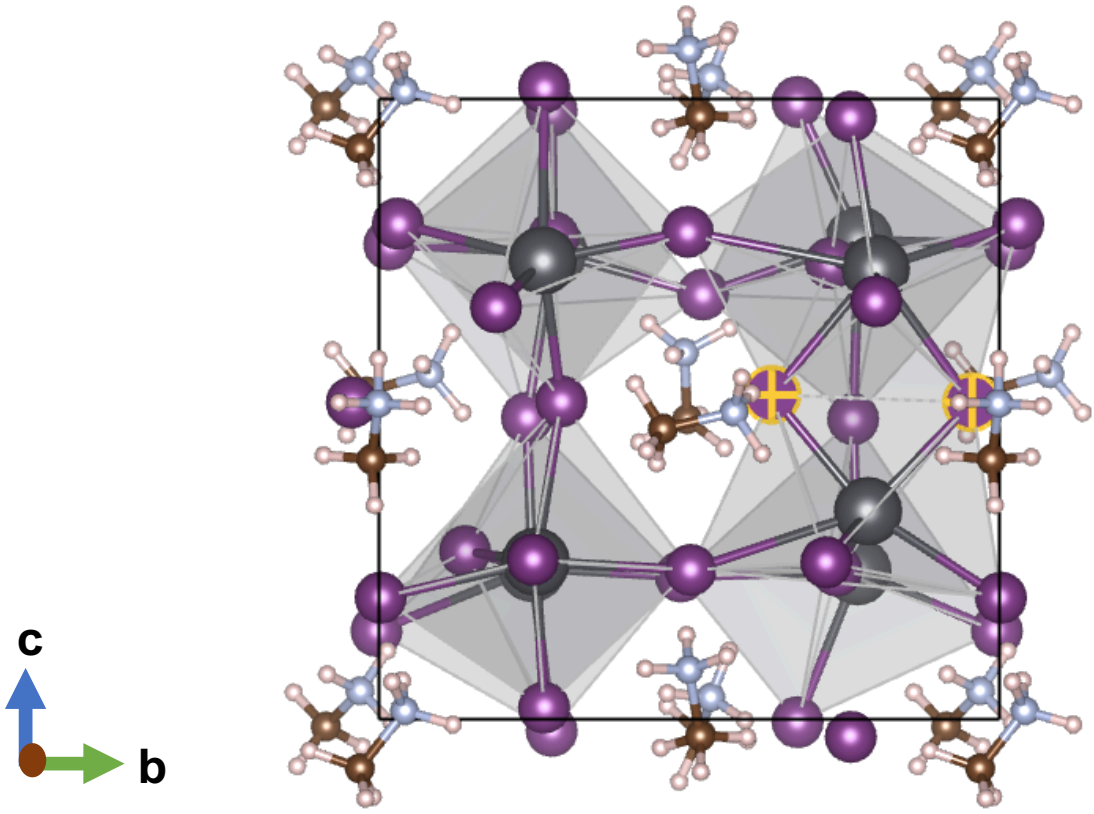

Figure 5.6. Finishing State in one cycle of I3 process: 2 interstitial I^- (2 crossing) and 1 V_I^+. The front view of a cell with 97 atoms is shown.

The calculation shows the energy of the final state to be 88 meV higher than the starting state, with the two iodides migrated by 0.80 Å and 1.1 Å as well as the rotation of MA groups, as shown in Figure 5.7. The intermediate state at the energy peak is only 3 meV greater than the final state. This threshold energy for ionic impact ionization is less than one tenth of the threshold energy for electron impact ionization process [13-16], which is consistent with the measurement of threshold E-field.

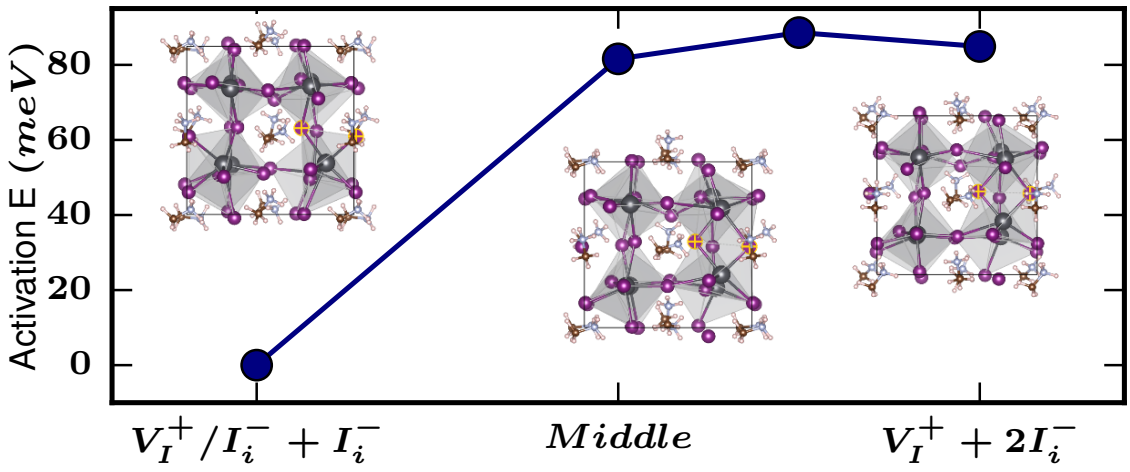

Figure 5.7. The activation energies from 1 V_I^+/I^- Frenkel pair and 1 interstitial I^- to 2 interstitial I^- and 1 V^+. The energy barrier is 91 meV from the 4 calculated structures.

5.3 Discussion and Conclusion

Although the threshold field for I3 process was surprisingly found to be orders of magnitude lower than the threshold field for electron impact ionization in most condensed matters, the results were supported by the calculations from our DFT toy model. The latter show that it takes only 88 to 91 meV to dissociate a V_I^+/I_i^- Frenkel pair into an interstitial iodide and positively charged iodine vacancy V_I^+ when an interstitial iodide is nearby. The threshold energy for I3 process is indeed more than an order of magnitude lower than the required energy for electron impact ionization. However, our DFT toy model can be improved by considering the grain boundaries in perovskite, given that the spin-coated perovskite film has some level of disorders. Though there are low angles and high angles grain boundaries, without losing generality, we can consider the tilt (-120) grain boundaries from cubic unit cell which have been observed in perovskite film through Transverse Electron Microscope (TEM) [17].

The perfect grain boundary was constructed with the relaxed cubic unit cell, keeping I atoms at the grain boundaries, by using the code similar to this paper [18]. There are 288 atoms in the (-120) supercell, as shown in Figure 5.8., which is a trade-off between our computational power and defect density level. All the GB DFT calculations are done with VASP [19], with 500 eV cutoff, GGA pseudopotential and gamma point fixed volume relaxation. The grain boundary situation is more complicated, in that the MA groups in the relaxed GB structure have already rotate compared with the perfect tilt GB case.

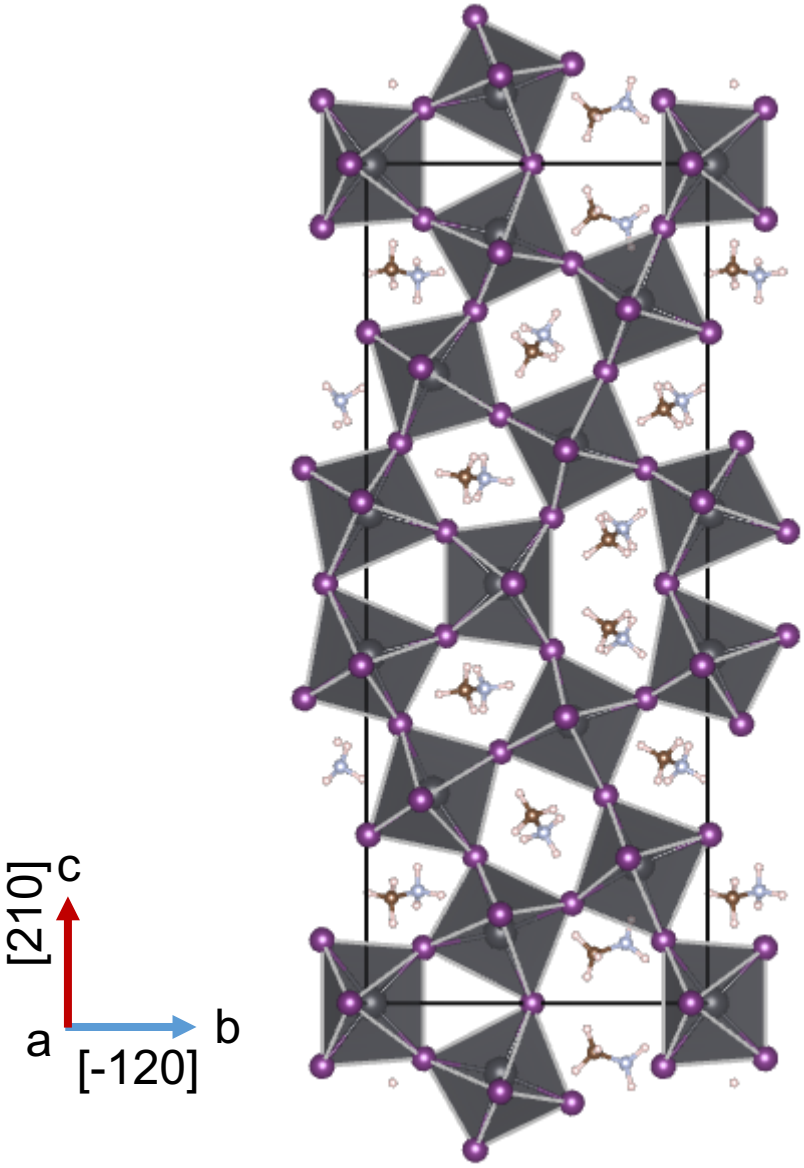

Figure 5.8. Relaxed structure for tilt (-120) grain boundary of perovskite. 288 atoms.

We only simulated the starting and finishing states of one cycle for I3 process in the tilt grain boundary of perovskite and the relaxed structures are illustrated in Figure 5.9. Similar to the bulk case, the starting state (the left one in Figure 5.9) has 1 interstitial

iodide and one Frenkel pair along the c = 0.5 grain boundary, while the finishing state include two interstitial iodides along the two sides of the grain boundary and a positively charged vacancy. The energy difference between the starting and ending states for one cycle of I3 process in GB is only 23 meV, which is much smaller than the 89 meV in bulk case and can suggest the enhancement of I3 process with grain boundaries in perovskite. The detail path for I3 process along the grain boundaries or how to migrate from and to the grain boundaries still require future investigation.

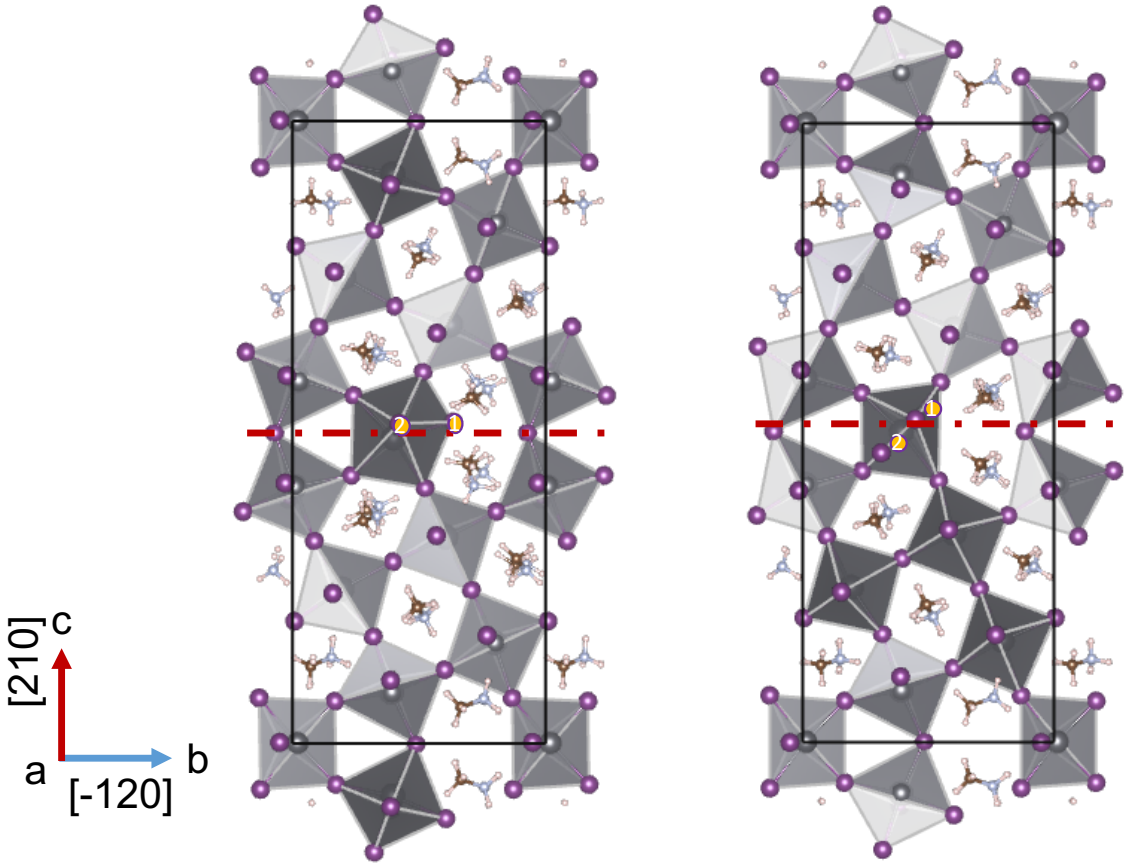

Figure 5.9. Relaxed structures for the starting (left) and finishing (right) states of one cycle in I3 process at the grain boundary. Starting states: 1 Frenkel pair and 1 interstitial iodide; Finishing state: 2 interstitial iodides and a positively charged vacancy.

The trap filling process [20-22] could impede the proposed ionic impact ionization process in perovskite. When the bias level is low, the initial mobile iodide needs to travel a longer distance to gain enough energy so as to trigger another cycle of ionic impact ionization. A longer travel distance reduces the number of ionic impact ionization cycles as well as increases the probability to encounter a trap level, which will decrease photoresponse under lower bias. For 8 photons of 518 nm, the trap filling process becomes dominant for bias below 0.62 V. Together with the Schottky barrier between ITO and perovskite that affects electron transport, the photoresponse drop dramatically below 0.62 V.

Our study also suggests the mechanism of generating initial photoexcited iodide by way of e-h excitation, followed by non-radiative recombination to produce multiple phonons with sufficient kinetic energy to produce mobile iodide. The I3 process is reversible in the sense that the accumulated iodides near the anode can return to the original distribution, and the recovery time can be shortened by an applied field opposite to the original filed. We have studied two reset conditions: setting the bias to 0 V and reversing the bias from 1V to -1V. The first condition relies on iodide diffusion in dark and the second condition uses an opposite field to accelerate the motion of iodide. As shown in Figure 5.10, under zero bias, the device needs 140 seconds to have its dark current return to its original value, while under the second condition, the device dark current is reset in 70 seconds.

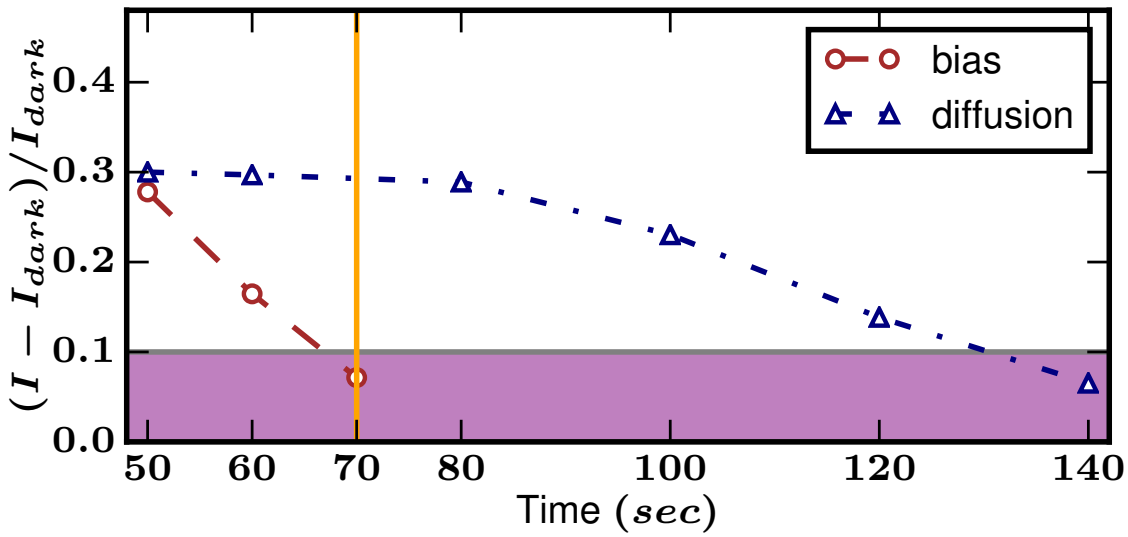

Figure 5.10. Reset of perovskite photodetector with the reverse bias or with diffusion only in the dark.

Portions of Chapter 5 have been published in the following publication: **Zihan Xu**†, Yugang Yu†, Shaurya Arya, Iftikhar Ahmad Niaz, Yimu Chen, Yusheng Lei, Mohammad Abu Raihan Miah, Jiayun Zhou, Alex Ce Zhang, Lujiang Yan, Sheng Xu, Kenji Nomura and Yu-Hwa Lo, "Frequency and Power Dependent Photoresponse of Perovskite Photodetector Down to Single Photon Level", *Nano Letters*, (2020). († These authors contributed equally.) The dissertation author was the co-first author/primary investigator and author of these papers.

References:

[1] Mosconi, Edoardo, Daniele Meggiolaro, Henry J. Snaith, Samuel D. Stranks, and Filippo De Angelis. "Light-induced annihilation of Frenkel defects in organo-lead halide perovskites." *Energy & Environmental Science* 9, no. 10 (2016): 3180-3187.

[2] Li, Cheng, Steffen Tscheuschner, Fabian Paulus, Paul E. Hopkinson, Johannes Kießling, Anna Köhler, Yana Vaynzof, and Sven Huettner. "Iodine migration and its effect on hysteresis in perovskite solar cells." *Advanced Materials* 28, no. 12 (2016): 2446-2454.

[3] Pérez-Osorio, Miguel A., Rebecca L. Milot, Marina R. Filip, Jay B. Patel, Laura M. Herz, Michael B. Johnston, and Feliciano Giustino. "Vibrational properties of the organic–inorganic halide perovskite CH3NH3PbI3 from theory and experiment: factor group analysis, first-principles calculations, and low-temperature infrared spectra." *The Journal of Physical Chemistry C* 119, no. 46 (2015): 25703-25718.

[4] Li, Cheng, Antonio Guerrero, Sven Huettner, and Juan Bisquert. "Unravelling the role of vacancies in lead halide perovskite through electrical switching of photoluminescence." *Nature communications* 9, no. 1 (2018): 1-8.

[5] Li, Cheng, Antonio Guerrero, Yu Zhong, Anna Gräser, Carlos Andres Melo Luna, Jürgen Köhler, Juan Bisquert, Richard Hildner, and Sven Huettner. "Real-time observation of iodide ion migration in methylammonium lead halide Perovskites." *Small* 13, no. 42 (2017): 1701711.

[6] Li, Pengfei, B. N. Shivananju, Yupeng Zhang, Shaojuan Li, and Qiaoliang Bao. "High performance photodetector based on 2D CH3NH3PbI3 perovskite nanosheets." *Journal of Physics D: Applied Physics* 50, no. 9 (2017): 094002.

[7] Mali, Sawanta S., and Chang Kook Hong. "pin/nip type planar hybrid structure of highly efficient perovskite solar cells towards improved air stability: synthetic strategies and the role of p-type hole transport layer (HTL) and n-type electron transport layer (ETL) metal oxides." *Nanoscale* 8, no. 20 (2016): 10528-10540.

[8] Perdew, John P., Kieron Burke, and Matthias Ernzerhof. "Generalized gradient approximation made simple." *Physical review letters* 77, no. 18 (1996): 3865.

[9] Giannozzi, Paolo, Stefano Baroni, Nicola Bonini, Matteo Calandra, Roberto Car, Carlo Cavazzoni, Davide Ceresoli, G. L. Chiarotti, M. Cococcioni, I. Dabo, A. D. Corso, S. de Gironcoli, S. Fabris, G. Frates, R. Gebauer, U. Gerstmann, C. Gougoussis, A. Kokalj, M. Lazzeri, L. "QUANTUM ESPRESSO: a modular and open-source software project for quantum simulations of materials." *Journal of physics: Condensed matter* 21, no. 39 (2009): 395502.

[10] Beltracchi, Philip. "First-principles study of hybrid organic-inorganic perovskites for photovoltaic applications, A." PhD diss., Colorado School of Mines. Arthur Lakes Library, 2015.

[11] Stoumpos, Constantinos C., Christos D. Malliakas, and Mercouri G. Kanatzidis. "Semiconducting tin and lead iodide perovskites with organic cations: phase transitions, high mobilities, and near-infrared photoluminescent properties." *Inorganic chemistry* 52, no. 15 (2013): 9019-9038.

[12] Weller, Mark T., Oliver J. Weber, Paul F. Henry, Antonietta M. Di Pumpo, and Thomas C. Hansen. "Complete structure and cation orientation in the perovskite photovoltaic methylammonium lead iodide between 100 and 352 K." *Chemical Communications* 51, no. 20 (2015): 4180-4183.

[13] Mattoni, A., Alessio Filippetti, M. I. Saba, and P. Delugas. "Methylammonium rotational dynamics in lead halide perovskite by classical molecular dynamics: the role of temperature." *The Journal of Physical Chemistry C* 119, no. 30 (2015): 17421-17428.

[14] Eames, Christopher, Jarvist M. Frost, Piers RF Barnes, Brian C. O'regan, Aron Walsh, and M. Saiful Islam. "Ionic transport in hybrid lead iodide perovskite solar cells." *Nature communications* 6, no. 1 (2015): 1-8.

[15] Azpiroz, Jon M., Edoardo Mosconi, Juan Bisquert, and Filippo De Angelis. "Defect migration in methylammonium lead iodide and its role in perovskite solar cell operation." *Energy & Environmental Science* 8, no. 7 (2015): 2118-2127.

[16] Liu, Yu-Hsin, Lujiang Yan, Alex Ce Zhang, David Hall, Iftikhar Ahmad Niaz, Yuchun Zhou, L. J. Sham, and Yu-Hwa Lo. "Cycling excitation process: An ultra efficient and quiet signal amplification mechanism in semiconductor." *Applied Physics Letters* 107, no. 5 (2015): 053505.

[17] Guo, Yaguang, Qian Wang, and Wissam A. Saidi. "Structural stabilities and electronic properties of high-angle grain boundaries in perovskite cesium lead halides." *The Journal of Physical Chemistry C* 121.3 (2017): 1715-1722

[18] Tran, Richard, Zihan Xu, Naixie Zhou, Balachandran Radhakrishnan, Jian Luo, and Shyue Ping Ong. "Computational study of metallic dopant segregation and embrittlement at molybdenum grain boundaries." *Acta Materialia* 117 (2016): 91-99.

[19] Hafner, Jürgen. "Materials simulations using VASP—a quantum perspective to materials science." *Computer physics communications* 177, no. 1-2 (2007): 6-13.

[20] Heo, Sung, Gabseok Seo, Yonghui Lee, Dongwook Lee, Minsu Seol, Jooho Lee, Jong-Bong Park, J.B., Kim, K., Yun, D.J., Kim, Y.S. and Shin, J.K., "Deep level trapped defect analysis in CH 3 NH 3 PbI 3 perovskite solar cells by deep level transient spectroscopy." Energy & Environmental Science 10, no. 5 (2017): 1128-1133.

[21] Wen, Xiaoming, Yu Feng, Shujuan Huang, Fuzhi Huang, Yi-Bing Cheng, Martin Green, and Anita Ho-Baillie. "Defect trapping states and charge carrier recombination in organic–inorganic halide perovskites." *Journal of Materials Chemistry C* 4, no. 4 (2016): 793-800.

[22] Duan, Hsin-Sheng, Huanping Zhou, Qi Chen, Pengyu Sun, Song Luo, Tze-Bin Song, Brion Bob, and Yang Yang. "The identification and characterization of defect states in hybrid organic–inorganic perovskite photovoltaics." *Physical chemistry chemical physics* 17, no. 1 (2015): 112-116.

Chapter 6 Conclusion and Outlook

Cycling Excitation Process (CEP) is an intrinsic mechanism of signal amplification for photodetection in disordered materials. The level and scale of disorder as well as the dark current or noise generation can influence the effectiveness of CEP. Amorphous Si on nSi photodetector can already achieve low noise and high gain bandwidth product.

In order to explore broader applications for CEP mechanism in amorphous Si, ITO on glass was used. By incorporating Au NP and utilizing LSPR effect, the absorption within the carbon doped amorphous Si layer was improved. With the help of Au NP, the dark current was suppressed, the photoresponse was enhanced and the device frequency response was faster. Through 3D electromagnetic simulation in COMSOL results, near Au NP, the enhancement of the electromagnetic field enhanced the absorption of light and the enhancement of the electric field can improve the CEP efficiency.

Photodetection in spin-coated organometallic perovskite device is more sophisticated. There were two types of photodetection. The first one is like conventional photoresponse in p-i-n diode, having high frequency response but no gain. The detailed study for the power and frequency dependence in perovskite photodetector also correct a historical misconception in the perovskite society. The misconception comes from measuring power dependent responsivity under (quasi)DC condition and impulse response under high frequency while assuming the DC responsivity applies to the high frequency response. However, the reality is that for perovskite, there is actually “no gain or increased responsivity” under even intermediate frequency. The other type of

photoresponse is quasi-persistent photoresponse, which has single photon sensitivity. The well-engineered small active area of perovskite photodetectors enabled the single photon detection, which led to the discovery of another novel internal amplification process, the proposed ionic impact ionization. DFT toy model was built to further support the physical mechanism. The reversible and highly sensitive quasi-persist photoresponse can have application such as analog memory device for neuromorphic computing.

There are more disordered materials to explore for various photodetection, with the inspiration of CEP mechanism in the studied amorphous silicon photodetectors. And the proposed novel internal amplification mechanism in perovskite, the ionic impact ionization, requires future studies from both experimental and computational approaches such as investigating ionic impact ionization in other type of organometallic perovskites as well as grain boundaries influences. Apart from the studied photon induced ionic impact ionization, the electron injection induced ionic impact ionization is also worthy for investigation in the future.